Enhancing Heat Pipe Efficacy: Thermosyphon Analysis, New Generation Refrigerant Transition, and Design Optimization

by

Vivek Kumar

A thesis submitted in partial fulfillment of the requirements for the degree of

Master of Science

Department of Mechanical Engineering
University of Alberta

Abstract

The efficacy of heat pipes is often constrained by their ability to effectively return condensed liquid from the condenser to the evaporator section through capillary pumping. However, when the heat pipe wick is absent or flooded due to overfilling, capillary pumping becomes irrelevant, resulting in a thermosyphon system. In a close-to-horizontal orientation, the driving force for liquid return in a thermosyphon is derived from the difference in liquid pool depth between the evaporator and condenser. Increasing the depth of condensed liquid augments the driving force for flow. However, an excessively deep liquid pool in the condenser can limit radial heat transfer and hinder heat rejection. Therefore, it is crucial to strike a balance that favors intermediate-depth liquid pools. Increasing the fill ratio beyond the optimized value leads to escalated manufacturing costs and adverse effects on performance. This study employs a theoretical approach based on the lubrication approximation to the Navier-Stokes equations to determine the fill ratio that maximizes thermosyphon performance. Additionally, we explore the variations of this ratio in relation to factors such as the axial temperature difference along the thermosyphon. Our analysis overcomes a common simplification observed in conventional thermosyphon descriptions by considering the incremental flow resistance resulting from axial variations in the liquid film thickness. Neglecting this aspect can lead to inaccuracies in estimating the axial heat flux. The modeling of heat pipe and thermosyphon results aids in the selection between a thermosyphon and a heat pipe, while also utilizing the hydrostatic-driven flow limit in the thermosyphon to replace the capillary limit in the heat pipe "fundamental diagram."

Furthermore, we compare the efficacy of R513a, an HFC/HFO refrigerant blend with lower global warming potential, to the commonly used R134a refrigerant in the context of heat pipe applications. Considering the adverse environmental impact of refrigerants on global warming, it is imperative to identify and implement eco-friendly alternatives with reduced global warming potential. Tests were conducted on both smooth and grooved heat pipes under uniform environmental conditions to evaluate the principal variations in performance and operation between the two refrigerants. Our study suggests that, in most cases, R513a can serve as a one-to-one substitute for R134a, demonstrating superior performance and enhanced heat transfer capacity. In certain situations, an integrated approach that involves adjusting only the fill mass is necessary to achieve comparable outcomes. This study illuminates a critical transition strategy towards alternative refrigerants, highlighting the potential for eco-friendly substitutes that rival or outperform conventional refrigerants.

Additionally, we present a Matlab-based, GUI-driven algorithm developed for heat pipe design and optimization. The algorithm predicts the thermodynamic performance of a heat pipe by considering various limiting conditions imposed by viscosity, capillary action, entrainment, boiling, and compressibility. This standalone tool assists in selecting the appropriate working fluid for a heat pipe and constructs a fundamental diagram over a wide temperature range. Furthermore, it facilitates the identification of optimal design parameters in a given setting. We utilized this tool to achieve an optimized design of axial heat transfer with enhanced performance, leveraging experimental data from the previous section specifically for a helical grooved heat pipe.

To sum up, our study contributes to the enhancement of heat pipe efficacy through an analysis of thermosyphon behavior, a comparison between eco-friendly refrigerants,

and the development of a Matlab-based algorithm for heat pipe design and optimization. These findings offer valuable insights into achieving optimal heat transfer and provide a foundation for selecting suitable heat pipe configurations and working fluids for various applications.

Acknowledgements

I am sincerely grateful to my mentors, Dr. Morris Flynn and Dr. Prashant Waghmare, for their exceptional guidance, valuable feedback, and unwavering support throughout my research journey. Their extensive knowledge and expertise in the field of thermo-fluidics have been truly inspiring, and I consider myself fortunate to have had the opportunity to learn from them. I have had the opportunity to work, learn, and collaborate with Muhammad Rizwanur (Rishad) as well. He is an absolute gem of a person and it's always exciting to work with him. Furthermore, I would like to express my deepest appreciation to Dr. Himanshu Trivedi for his consistent emotional support, which has meant a great deal to me.

I would like to express my gratitude to Dr. Sina Ghaemi for serving as the external examiner and to Dr. Ahmed Qureshi for being the Chair. Your valuable time and guidance are deeply appreciated, and I will always be obliged for your support.

Thank you to my course instructors for imparting their knowledge to me: Dr. Morris Flynn (Environmental Fluid Dynamics), Dr. Sina Ghaemi (Aerodynamics), Dr. Jamie Wong (Fluid Mechanics), Dr. Anthony Yeung (Advanced Transport Phenomena), Dr. Xuehua Zhang, and Dr. Andre Macdonald (Conduction Heat Transfer).

My heartfelt thanks go to my esteemed colleagues, Ganesh Prabhu Komaragiri, Raihanul Kabir, Zachary Shannon, Ryan Baily, and Aleksey Baldygin, whose invaluable assistance and guidance have played a pivotal role in the completion of this thesis.

Table of Contents

List of Tables

List of Figures

Chapter 1

Introduction

Heat generation and cooling systems are essential in various engineering applications, serving important purposes such as managing thermal loads, optimizing energy conversion, ensuring equipment efficiency, maintaining material integrity, and promoting safe operating conditions. These systems play a vital role in fields like power generation, aerospace, automotive, and electronics, where efficient heat management is crucial for reliable and high-performance operation. Engineers work towards designing and implementing effective cooling solutions that not only minimize environmental impact but also enhance energy efficiency. Hence, heat generation and cooling systems are integral to the success of engineering applications as they enable optimal performance, durability, and safety. In many engineering processes, excess heat is produced, necessitating its dissipation, especially in cases like microelectronic devices. On the other hand, in situations such as replacing stale interior air with fresh exterior air so as to meet air-exchange requirements, heat needs to be transferred. One effective method for dissipating or transferring heat is by utilizing a heat pipe.

A heat pipe is a heat transfer device that is used to move heat from one point to another [1]. It consists of a sealed container with a wick saturated by a working fluid. The fluid undergoes phase changes between liquid and vapor, enabling efficient axial heat transfer, even when the heat source and sink are separated by nontriv-

ial distances but relatively minor temperature differences. Consequently, heat pipes are highly adaptable and require minimal maintenance in industrial, residential, and commercial settings.

As suggested by the above commentary, a major appeal of heat pipes is that they are passive devices, meaning that they do not require any external energy input to function. In addition, the effective thermal conductivity of a heat pipe is much higher than that of solid materials like metals, which makes it a very efficient heat transfer device, particularly in scenarios where space and weight are at a premium. The thermal conductivity range of a heat pipe depends on several factors, including the materials used in the construction of the heat pipe, the working fluid, and the size and geometry of the heat pipe. Generally, the thermal conductivity range of a heat pipe can vary from $\sim 500\,\mathrm{W/(m\,K)}$ to $200{,}000\,\mathrm{W/(m\,K)}$ [2–6].

The basic operation of a heat pipe can be summarized in the following steps [7–9]: First, heat is applied to one end of the heat pipe, which causes the working fluid to vaporize. The heat causes the fluid to reach its boiling point and turn into vapor. Secondly, the vapor travels down the length of the heat pipe to the cooler end, where it condenses. The heat that was absorbed during the boiling process is then released as the vapor turns back into a liquid. Afterward, the condensed liquid flows back to the hot end of the heat pipe, either through capillary action or gravity or both, and the cycle repeats. During the operation of a heat pipe, the working fluid is constantly moving between the hot and cold ends of the pipe, allowing for efficient heat transfer. The key to the effectiveness of heat pipes lies in the fact that they can transfer large amounts of heat with very little temperature difference between the hot and cold ends. A heat pipe consists of several components, including [10–12]:

1. Evaporator: This is the section of the heat pipe where heat is absorbed from the heat source. The evaporator is typically located at the hot end of the heat pipe and is designed to have a large surface area to maximize heat absorption.

2. Condenser: This is the section of the heat pipe where heat is released to the surrounding environment. The condenser is typically located at the cold end of the heat pipe and is designed to have a large surface area to maximize heat dissipation.

3. Working fluid: This is the fluid that is used to transfer heat within the heat pipe. The working fluid is typically a low boiling point liquid that vaporizes in the evaporator and condenses in the condenser. Common working fluids include water, ammonia, and refrigerants such as R134a.

4. Wicking structure: This is a capillary structure that is used to transport the working fluid from the condenser to the evaporator. The wicking structure is typically made of a porous material such as sintered metal or woven mesh.

5. Envelope: This is the outer shell of the heat pipe that encloses the working fluid, wicking structure, and other components. The envelope is typically made of a material with good thermal conductivity, such as copper or aluminum, to facilitate heat transfer.

Due to the simple design with few components and simple operations, and their high efficacy, heat pipes are commonly used in applications where space and weight are at a premium, such as in the cooling of electronic components, as well as in more demanding applications. The applications include electronics, microelectronics, defense, aerospace, cryogenic systems, and solar thermal systems [13–16].

In electronics cooling, heat pipes are commonly used to cool electronic devices, such as CPUs, GPUs, and related components [6, 17–19]. They provide efficient

cooling with minimal noise and can handle high heat loads. Heat pipes are widely employed in electronics cooling due to their exceptional heat transfer capabilities. In various applications, such as CPU cooling, heat pipes play a crucial role. Whether in desktop computers, laptops, or servers, heat pipes efficiently transfer heat away from the CPU to a heat sink, where the heat in question can be dissipated by air-flow. Similarly, graphics cards, which often generate substantial heat, utilize heat pipes in their coolers to transfer heat from the GPU to a large heatsink or cooling fan, ensuring optimal performance and preventing overheating. Heat pipes are also instrumental in laptop cooling, enhancing efficiency and preventing thermal throt-tling by transferring heat away from the CPU and GPU to the laptop's heat sink or cooling fan. Moreover, in high-power LED lighting systems, heat pipes are applied to dissipate heat efficiently, promoting longer lifespan and preserving optimal perfor-mance. Power electronic components, such as inverters and power supplies, as well as telecommunications equipment like routers and switches, also benefit from heat pipe technology. Heat pipes effectively transfer heat away from these devices, ensur-ing stable operation and preventing thermal damage. Additionally, heat pipes find applications in automotive electronics, medical devices, and various other systems where effective cooling is essential for maintaining reliability, longevity, and optimal performance. With their compactness, high heat transfer capacity, reliability, and passive operation, heat pipes offer an excellent solution for managing heat in diverse electronic devices and systems [20].

Heat pipes also play a vital role in the aerospace and defense sector, where ef-fective thermal management is no less crucial [21–24]. They are extensively used in spacecraft thermal control systems to regulate temperatures and dissipate excess heat generated by onboard electronics and equipment. In avionics systems, heat pipes are employed to cool critical components, ensuring optimal performance and reliability in demanding environments. Military electronics, such as radar, navigation systems,

4

and communication devices, benefit from heat pipe cooling to enhance their performance and endurance in extreme conditions. Heat pipes are likewise integral to thermal protection systems for reentry vehicles and spacecraft, safeguarding components from extreme temperatures during atmospheric reentry. They are also utilized in missile guidance systems, electronic warfare systems, and unmanned aerial vehicles (UAVs) to manage heat and maintain the operational effectiveness of critical systems.

Heat pipes also find application in energy recovery systems to efficiently transfer and reclaim waste heat [7, 25–27]. In applications such as exhaust gas heat recovery, heat pipes play a crucial role in extracting waste heat from flue gases and transferring this heat to a working fluid for utilization. They are also employed in industrial processes to recover and transport waste heat for preheating fluids or generating electricity. Heat pipes find applications in data centers to cool servers while recovering and utilizing the generated heat. Additionally, they are integrated into industrial ovens, furnaces, and geothermal systems to capture and transfer waste heat for various energy recovery purposes. By enabling efficient heat transfer and maximizing the utilization of waste heat, heat pipes contribute to energy efficiency, reduced energy consumption, and sustainable practices in energy recovery systems.

In a similar spirit, heat pipes have become valuable components in HVAC (Heating, Ventilation, and Air Conditioning) systems, offering improved efficiency and performance and therefore potentially lucrative opportunities for cost savings [28–30]. In HVAC applications, heat pipes find several practical uses. Firstly, in Heat Recovery Ventilation (HRV) and Energy Recovery Ventilation (ERV) systems, heat pipes enhance heat transfer efficiency by recovering heat from the exhaust air and transferring it to the incoming air stream. This reduces the energy required for heating or cooling the fresh air and helps maintain comfortable indoor temperatures. Secondly, heat pipes play a crucial role in dehumidification processes by removing excess moisture

5

from the air. They cool the air below its dew point, causing moisture to condense. Additionally, heat pipes are utilized in cooling towers to enhance heat transfer efficiency, enabling efficient cooling of industrial processes or air conditioning systems. Moreover, heat pipes contribute to the performance of heat pump systems by improving heat transfer between the refrigerant and the conditioned space, resulting in enhanced energy efficiency. Overall, incorporating heat pipes into HVAC systems offers benefits such as energy savings, improved thermal comfort, and reduced operating costs.

Heat pipes likewise enjoy diverse applications in solar thermal systems [7, 25–27, 31]. They are commonly used in solar water heating devices, where they efficiently transfer heat from the collector to a heat exchanger for water or heat transfer fluid heating. In concentrated solar power (CSP) systems, heat pipes enable the collection and transport of concentrated solar energy, optimizing heat transfer to a working fluid or heat transfer medium. Solar air heating systems utilize heat pipes to enhance the transfer of solar heat to the air flowing through the system in question. Heat pipes also find applications in solar thermal power plants, aiding in heat transfer between various components and optimizing energy conversion. Additionally, heat pipes contribute to solar desalination systems by facilitating the transfer of heat for the distillation or evaporation of seawater. Overall, heat pipes play a vital role in solar thermal systems, improving energy efficiency and enhancing the utilization of solar energy.

Finally, heat pipes are widely used in various cryogenic applications [32–35]. In cryogenic systems, which involve extremely low temperatures, heat pipes play a crucial role in maintaining thermal stability and efficient heat transfer. Heat pipes are commonly employed in cryocoolers, which provide cooling at cryogenic temperatures for applications like superconducting magnets and infrared detectors. Heat pipes en-

able the transfer of heat from the cold end to the hot end, enhancing the performance and reliability of cryocoolers. Cryostats, used to maintain low temperatures in chambers or vessels, also benefit from heat pipes by removing heat generated by electronic components or sensors, thereby preventing localized heating. In cryogenic storage systems, heat pipes help in the efficient removal of heat to prevent the boiling off of cryogenic fluids or to maintain stable temperatures for stored materials. Cryogenic instrumentation, such as pumps, valves, and heat exchangers, utilize heat pipes to transfer heat away from sensitive components or to cool them to cryogenic temperatures. Furthermore, in space applications, heat pipes are employed for cryogenic thermal management, facilitating the transfer of heat in the vacuum of space. Overall, the high thermal conductivity, low thermal resistance, and lightweight design of heat pipes make them indispensable for efficient cryogenic temperature management in various applications.

In summary, heat pipes are a versatile and reliable technology for transferring heat in a wide range of applications, and their use continues to grow as new applications are developed. Notwithstanding these positive attributes, heat pipes have some limitations that should be considered in their design and selection. Some of the key limitations in the use of heat pipes include the following [36–40]:

Temperature limitations: Heat pipes have upper-temperature limits that depend on the working fluid and materials used in their construction. If the temperature exceeds these limits, the working fluid may degrade or the materials may fail, leading to a loss of efficiency or even a complete failure of the heat pipe.

Orientation limitations: Heat pipes have a preferred orientation due to their reliance on gravity and capillary forces for fluid circulation. If the heat pipe is not oriented correctly, it may not function efficiently or at all.
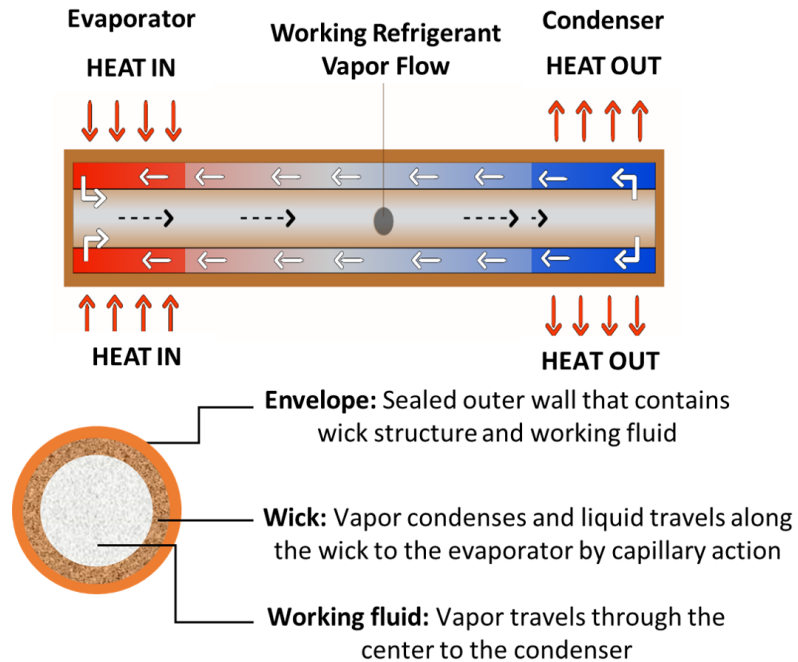
Figure 1.1: Schematic showing the different components of a heat pipe.

Pressure limitations: Heat pipes operate at low pressures, typically less than 1 atm. If the heat pipe is subjected to high pressures, it may fail or lose efficiency.

Chemical Compatibility limitations: Heat pipes may not be compatible with certain working fluids or materials, which can limit their use in certain applications.

Size limitations: Heat pipes are limited in size due to their reliance, at leat in part, on capillary forces for fluid circulation. Large heat pipes may require additional support or may not function efficiently.

In view of the above considerations, heat pipes have been traditionally limited to a narrow range of operating conditions. As a result, design engineers and researchers are continuously seeking to expand the range of applications and to enhance the performance of existing ones. To achieve this, careful selection of heat pipe components

and meticulous design play a critical role. Thus, much attention has been devoted to the return flow of the liquid from the condenser to the evaporator. This flow is driven by surface tension. However, if the surface tension of the liquid is low or if the wick is oversaturated or absent, the flow is then primarily driven by gravity. In particular, when there is no wick, the heat pipe is instead referred to as a thermosyphon. Thermosyphon design is relatively easy because thermosyphons are simple to operate, and economical. Therefore, these devices have been extensively studied.

Thermosyphons offer several advantages over heat pipes. Their simple design and construction make them cost-effective and easy to manufacture and maintain. Unlike heat pipes, thermosyphons are not limited by capillary action, allowing for longer heat transfer distances. By extension, thermosyphons excel in gravity-assisted systems, utilizing natural circulation driven by gravity for improved heat transfer. Operating at lower pressures reduces the risk of leaks and simplifies component design. Additionally, thermosyphons can handle higher heat loads due to their larger diameter and absence of capillary limitations, making them suitable for applications that require high-power dissipation. Ultimately, the choice between thermosyphons and heat pipes depends on specific application needs, taking into account factors such as heat load, orientation, space constraints, and cost considerations.

1.1 Design variables

Designing heat pipe and thermosyphon systems requires careful consideration of various key factors [41–43]. These factors play a crucial role in optimizing performance and include the following:

1. Operating temperature range: The choice of tube material will depend on the

operating temperature range of the heat pipe or thermosyphon. Materials must be able to withstand the temperature extremes of the heat pipe without degrading or failing.

2. Working fluid: The choice of tube material may also depend on the working fluid being used. Some fluids may be corrosive or reactive with certain materials, so it is important to choose a tube material that is compatible with the working fluid.

3. Tube dimensions: The dimensions of the tube will also impact its performance, including its ability to transfer heat efficiently. Factors such as the inner diameter, wall thickness, and tube length will need to be optimized for the specific application.

4. Wick design: The wick is an integral part of the heat pipe tube, and its design will impact the overall performance of the heat pipe. Factors such as the wick material, porosity, and permeability will need to be carefully considered to ensure effective operation.

5. Manufacturing considerations: The design of the heat pipe tube must also take into account variables related to the manufacturing process such as cost, ease of manufacture, and availability of materials.

6. Heat transfer requirements: The heat transfer requirements of the specific application will also impact the design of the heat pipe or thermosyphon tube. Factors such as the heat load, temperature difference, and required heat transfer rate will need to be considered when designing the tube.

Overall, designing a heat pipe tube involves a careful balance of the above factors to ensure that the heat pipe operates effectively and efficiently over its intended lifetime. The tube design must be optimized for the specific application, taking into

account all of the relevant factors to achieve the desired level of performance.

1.1.1 Selection of working fluid

The selection of the working fluid or refrigerant depends on the operating temperature range, heat transfer capacity, and compatibility with the materials used in the heat pipe. Some of the properties required for heat pipe refrigerants are [1, 44–46]:

1. High thermal conductivity: The refrigerant should have a high thermal conductivity to transfer heat efficiently from the heat source to the heat sink.

2. Low viscosity: Low viscosity is important to ensure that the refrigerant can flow easily through the narrow channels of the heat pipe, allowing for efficient heat transfer.

3. Low freezing point: The refrigerant should have a low freezing point to prevent it from solidifying at low temperatures, which could block the flow of the refrigerant and impede heat transfer.

4. Low boiling point: The refrigerant should have a low boiling point to ensure that it remains in the vapor phase at the operating temperature of the heat pipe.

5. Non-toxic and non-flammable: The refrigerant should be non-toxic and non-flammable to ensure safety in case of leaks or accidental exposure.

6. Chemical stability: The refrigerant should be relatively inert and should not react with the materials used in the heat pipe or with the heat source and heat sink.

7. Availability and cost: The refrigerant should be readily available and cost-effective to use in heat pipe applications.

Some common refrigerants used in heat pipe applications include [45, 47, 48]:

1. Water: Water is a commonly used refrigerant in heat pipes due to its high heat capacity and low cost. It is particularly effective for applications with low to moderate temperature ranges.

2. Ammonia: Ammonia is a popular refrigerant for industrial and commercial heat pipe applications due to its high heat transfer coefficient and low cost. However, it is also toxic and flammable, so appropriate safety measures must be taken.

3. Methanol: Methanol, known for its affordability and high latent heat of vaporization, is often used as a cost-effective refrigerant in low-temperature heat pipe applications. However, it is important to acknowledge that the flammable properties of methanol restrict its range of applications.

4. Ethanol: Ethanol is a widely used refrigerant in heat pipes for cooling electronic components and low-temperature applications due to its non-toxicity and affordability. However, it is important to note that the flammable nature of ethanol imposes limitations on its applications.

5. Fluorocarbons: Fluorocarbons, such as R134a, are commonly used refrigerants in air conditioning and refrigeration applications due to their low toxicity and high efficiency. However, they are also potent greenhouse gases and have a significant environmental impact.

High temperature heat pipes, typically use refractory metals or ceramics for their construction, as these materials have high melting points and can withstand the high temperatures involved. When it comes to selecting a refrigerant for high temperature heat pipes, there are a few options to consider [7, 49]:

Working fluid	$T_{\text{sink,min}}$ (°C)	$T_{\text{source,max}}$ (°C)
Acetone	-40	140
Methanol	-23	150
R134a	-40	316
R513a	-24	65
R514a	-24	65
Ammonia	-33	120
Water	20	200
Sodium	500	1300

Table 1.1: Temperature ranges for possible working fluids.

1. Sodium: Sodium is a common refrigerant for high temperature heat pipes, as it has a high boiling point and can operate at temperatures up to 1473 K (1200°C). It is also a good conductor of heat, which makes it an efficient choice for high temperature applications.

2. Potassium: Potassium is another option for high temperature heat pipe refrigerants, with a boiling point of 1033 K (760°C). It is also a good conductor of heat, but care must be taken to ensure that it does not react with the materials used in the heat pipe.

3. Lithium: Lithium is a lightweight, low-melting-point metal that can be used as a refrigerant in high temperature heat pipes, with a boiling point of 1615 K (1342°C). It is particularly useful for high temperature applications where size and weight are a concern.

4. Cesium: Cesium is another potential working fluid for high temperature heat pipes, with a boiling point of 1965 K (1692°C). However, it is a highly reactive metal that requires special handling and safety precautions.

The selection of a refrigerant for a heat pipe is an important consideration that

Figure 1.2: Wick types (a) Sintered wick (b) Wire mesh wick (c) Fibrous wick (d) Grooved wick. (From [50]; used with permission.)

can impact the performance, efficiency, and safety of the heat pipe system. It is important to carefully evaluate the specific requirements of the application and select a refrigerant that is compatible with the materials used in the heat pipe, provides the desired performance, and is safe and cost-effective.

1.1.2 Wick selection

Heat pipes use wicks to transport the working fluid from the condenser back to the evaporator. Ideally, the capillary pumping in question is aided by gravity, however, there are instances (evaporator situated above the condenser) where liquid transport by surface tension must overcome gravitational forcing. There are several types of wicks used in heat pipes, each with its own advantages and disadvantages [51–54]. These are described in greater detail below.

14

Sintered metal wicks are made by transforming a metal powder into a porous structure. They are highly durable and can withstand high temperatures and mechanical stresses, making them ideal for high-performance heat pipe applications. However, they can be expensive to manufacture and may be prone to clogging.

Grooved wicks are a type of heat pipe wick that feature a series of machined grooves or channels on the inner surface of the heat pipe. They offer several advantages, such as relatively simple manufacturing processes and good capillary action, but their effectiveness may vary depending on the specific application compared to other types of wicks. There are three common types of grooves used in heat pipes. Firstly, axial grooves are longitudinal grooves that run parallel to the length of the heat pipe. These grooves play a crucial role in facilitating the circulation of the working fluid in the axial direction, enhancing capillary action and improving heat transfer performance throughout the heat pipe. Secondly, circumferential grooves are concentric grooves that encircle the inner surface of the heat pipe. They promote the radial distribution of the working fluid within the heat pipe, enabling efficient heat transfer across the entire cross-section of the heat pipe and maximizing its thermal performance. Lastly, chevron grooves are V-shaped grooves that enhance the wicking action within the heat pipe, leading to improved fluid circulation and heat transfer. It is important to note that while grooved wicks can provide effective heat transfer, the selection of the appropriate wick type should be based on the specific requirements and constraints of the particular application.

Mesh wicks are made of fine wire mesh or of a screen, which is wound around a central support structure. They can be highly effective at transporting working fluid and are relatively easy to manufacture, but may be prone to clogging and can be sensitive to mechanical stresses. Fibrous wicks are made of highly porous materials such as ceramic fibers, carbon fibers, or glass fibers. They can provide good capillary

action and are highly resistant to mechanical stresses, but may also be prone to clogging and can be difficult to manufacture.

The design of the wick in a heat pipe is also an important consideration, as it can impact the efficiency and effectiveness of the heat pipe. Some key factors to consider when designing a wick for a heat pipe include its porosity, permeability, and thickness, as well as the type of working fluid being used.

1.1.3 Wick and envelope material selection

The selection of the tube material for a heat pipe depends on a variety of factors, including the operating temperature range, the working fluid used, and the mechanical and thermal properties required for the specific application. Some common materials used for heat pipe tubes include [55–57]:

1. Copper: Copper is a common choice for heat pipe tubes due to its high thermal conductivity, good mechanical properties, and relatively low cost. It is suitable for use with a wide range of working fluids and can operate at temperatures up to around 600°C.

2. Aluminum: Aluminum is another popular choice for heat pipe tubes, as it is lightweight and has good thermal conductivity. However, it may not be suitable for high temperature applications due to its relatively low melting point.

3. Stainless steel: Stainless steel is a durable and corrosion-resistant material that can be used in a wide range of heat pipe applications. It can operate at high temperatures and is suitable for use with many different working fluids.

4. Titanium: Titanium is a lightweight and strong material that can be used in high temperature and corrosive environments. It is particularly suitable for use with high temperature heat pipes and chemically-aggressive working fluids.
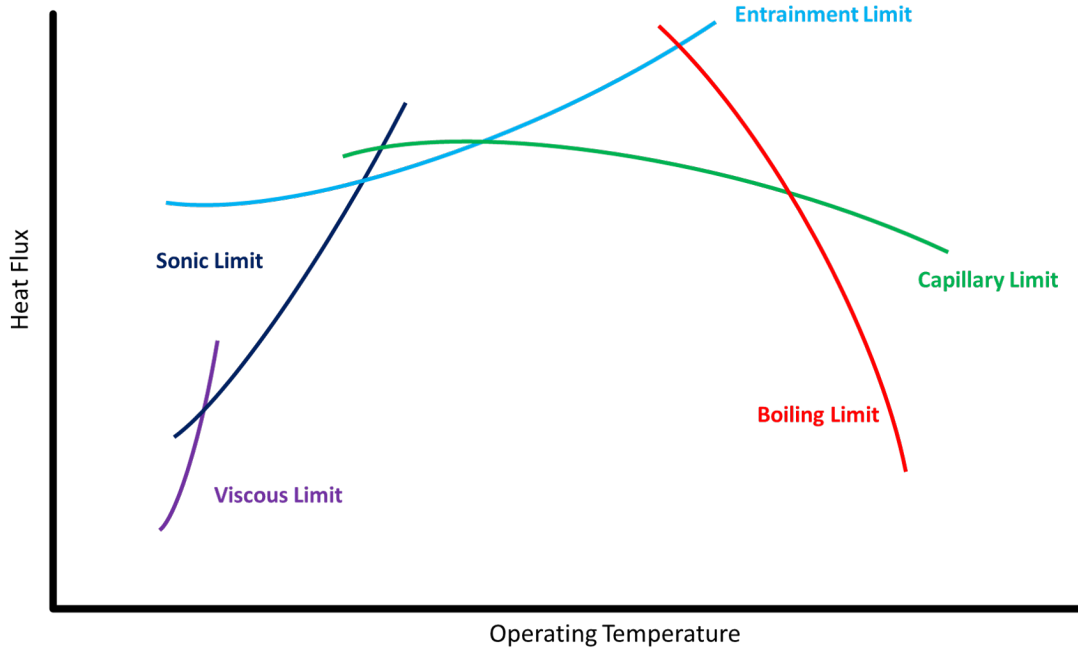
Figure 1.3: Heat pipe performance limitations[58].

5. Nickel alloys: Nickel alloys such as Inconel and Monel are often used in high temperature heat pipes due to their excellent corrosion resistance and high strength at elevated temperatures.

In addition to the tube material, other factors such as the thickness of the tube wall, the tube inner diameter, and the surface finish can also impact the performance of the heat pipe. It is important to carefully consider all of these factors when selecting a tube material for a heat pipe, in order to ensure that the heat pipe operates effectively and reliably over its intended lifetime.

1.2   Operational limitations

Current understanding of heat pipes [1, 59], [60] and [58] establishes several factors that can impose limits on the steady and transient operations of heat pipes. As shown in figure 1.3, the rate of heat transport through a heat pipe can be constrained by various physical phenomena, including the viscous limit, the capillary limit, the sonic limit, and the boiling limit. Also important to consider is frozen startup, as well

as condenser effects. The specific limitation on heat transfer can be determined by factors such as the size and shape of the tube, the working fluid, the wick structure, and the operating temperature. The maximum heat transport limitation of a heat pipe at a given temperature is defined by the lowest limit among these constraints. For a detailed explanation of the heat transfer limitations relevant to heat pipes, refer to [1]. Below, a brief summary is provided [1, 59].

Viscous limit: At lower temperatures, the heat pipe's evaporator region may have relatively low vapor pressures, which can be similar to the pressure required for propelling the vapor from the evaporator to the condenser. Consequently, the existing equilibrium between the total vapor pressure and the counteracting vapor viscous forces acting along the axial direction hampers the adequate flow of vapor mass. This condition, called the viscous limit, usually occurs in longer heat pipes with low saturation pressure of the working fluid near its melting temperature or during frozen startup conditions. A heat pipe operating near its triple point, where the vapor pressure is extremely low, experiences a "viscous limit" and necessitates the utilization of an alternative working fluid.

As vapor temperature does not appreciably vary over the length of the heat pipe, the vapor flow can be approximated as isothermal and the vapor itself can be considered as an ideal gas. Further, the vapor pressure at the condenser end is assumed to be zero, which provides the absolute limit for the condenser pressure. These simplifications lead to a one-dimensional laminar model of the vapor flow [61],

$$\dot{Q}_{\text{viscous}} = \frac{P_v \rho_v h_{fg} r_v}{16 \mu_v L_{\text{eff}}} \quad , \quad L_{\text{eff}} = L_a + \frac{L_e + L_c}{2} \tag{1.1}$$

Here, r_v represents the vapor core radius, L_a represents the adiabatic length, L_e represents the evaporator length, L_c represents the condenser length, P_v denotes vapor pressure, h_{fg} represents the enthalpy of vaporization, ρ_v stands for vapor density, μ_v

represents vapor viscosity, and L_{eff} indicates the effective length of the heat pipe.

Sonic limit: Typically, at low operating temperature and high radial heat flux, the vapor flow reaches sonic velocity near the end of the evaporator, causing a choking of the flow. This means that even if the heat flux is increased, the vapor flow cannot be further increased. The phenomenon in question often requires a very high power supply when operating at low temperatures. Typically, this phenomenon is observed during start-up and is expected to resolve itself over time as the operating temperature increases. The sonic limit of a heat pipe is determined by the maximum vapor velocity that can be sustained within the heat pipe before the vapor flow becomes supersonic. Once supersonic flow conditions are realized, the pressure drop and heat transfer coefficient within the heat pipe both decrease, leading to a reduced capacity for heat transfer. The sonic limit of a heat pipe is dependent on various factors, including the working fluid, heat pipe dimensions, and operating conditions such as temperature and pressure. It is typically experimentally determined by measuring the heat transfer capacity of the heat pipe at increasing heat inputs and plotting the resulting heat transfer rate against the heat input. The point at which the heat transfer rate begins to saturate or decrease indicates the sonic limit. The expression for the sonic limit is given by [61]

$$\dot{Q}_{\text{Sonic}} = A_v \rho_v h_{fg} \sqrt{\frac{\gamma_v R_v T_{\text{op}}}{2(\gamma_v + 1)}}, \tag{1.2}$$

where,

$$\gamma_v = \frac{C_p}{C_v} = \left(1 + \frac{2}{f}\right)$$

Here, f represents the degrees of freedom of the vapor molecules, R_v denotes the vapor gas constant, A_v represents the area for vapor core flow, and T_{op} indicates the operating temperature.

Entrainment limit: The entrainment limit of a heat pipe refers to the maximum

heat transfer capacity of the heat pipe, beyond which the vapor velocity in the evaporator section becomes large enough to entrain liquid droplets from the wick structure. Once the entrainment limit is reached, the heat transfer performance of the heat pipe is reduced due to a lack of sufficient liquid in the evaporator section. The entrainment limit depends on various factors, including the working fluid, wick structure, and operating conditions such as temperature and pressure. Consistent with the discussion of the sonic limit, the entrainment is also experimentally determined by measuring the heat transfer capacity of the heat pipe at increasing heat inputs and plotting the resulting heat transfer rate against the heat input. The point at which the heat transfer rate begins to saturate or decrease indicates the entrainment limit of the heat pipe. The primary distinction between the sonic limit and the entrainment limit lies in their respective temperature thresholds. The entrainment limit occurs at a higher temperature compared to the sonic limit. Furthermore, when the sonic limit is reached and the temperature difference (ΔT) is increased, the heat transfer rate ($\dot{Q}$) remains constant. Conversely, in the case of the entrainment limit, an increase in ΔT results in a decrease in $\dot{Q}$. The entrainment limit is approximated as follows [61]:

$$\dot{Q}_{\text{entr}} = A_v h_{fg} \sqrt{\frac{\rho_v \sigma}{2r_{h,s}}} \tag{1.3}$$

where $r_{h,s}$ is the wick pore radius and σ is the surface tension.

Boiling limit: At high heat fluxes, nucleate boiling may happen in the wick structure, leading to the entrapment of vapor in the wick. This can impede liquid return and result in evaporator dry-out. The limit in question is known as the boiling limit. Unlike other limitations, the boiling limit depends on the radial or circumferential heat flux in the evaporator, not the axial heat flux or total thermal power transported by the heat pipe. The boiling limit is determined using nucleate boiling theory, which consists of two phenomena: bubble formation and the subsequent growth or collapse of the bubbles. The boiling limit using nucleate boiling theory can be described as

20

[61]

$$\dot{Q}_{\text{Boil}} = \frac{2\pi L_{\text{e}} K_{\text{e}} T_{\text{v}}}{h_{fg}\rho_v \ln(r_{\text{i}}/r_{\text{v}})} \left(\frac{2\sigma}{r_{\text{b}}} - P_{\text{c}} \right) \tag{1.4}$$

where r_{b} represents the nucleation site radius, r_{i} represents the internal radius of the tube, r_{v} represents the vapor core radius (or inner wick radius), K_{e} represents the effective thermal conductivity of the liquid-saturated wick, σ denotes the surface tension of the liquid refrigerant, P_c represents the capillary pressure of the wick structure, and T_{v} represents the vapor temperature.

Capillary limit: The capillary limit, also known as the hydrodynamic limit, is a common constraint encountered in the operation of low-temperature heat pipes [1, 62]. This limitation occurs when the capillary pumping rate is insufficient to provide enough liquid to the evaporator section. Stated differently, the capillary limit arises when the sum of the liquid and vapor pressure drops exceeds the maximum capillary pressure that the wick can sustain. The maximum capillary pressure depends on the physical properties of the wick and on the working fluid. Any attempt to exceed the heat transfer limit imposed by the capillary limitation will cause dry-out in the evaporator section, which results in a sudden increase in wall temperature along the evaporator section. The capillary limit can be approximated by [61]

$$\dot{Q}_{\text{c,max}} = \frac{(QL)_{\text{c,max}}}{L_{\text{eff}}} \tag{1.5}$$

Here,

$$(QL)_{\text{c,max}} = \frac{P_c - \Delta P - \rho_l g L_t \sin(\theta)}{F_l + F_v}$$

where, $P_c = 2\sigma/r_c$, $\Delta P = \rho_l g d_v \cos\theta$ and F_l and F_v are given by

$$F_l = \frac{\mu_l}{\kappa A_w \rho_l h_{fg}}, \qquad F_v = \frac{(f_v Re_v)\mu_v}{2r_{\text{h,v}}^2 A_v \rho_v h_{fg}}$$

In the above equations, θ is the tube inclination angle, d_v is the vapor core diameter, L_t is the total length of the tube, κ is the wick permeability, $(f_v Re_v)$ is the drag coefficient, and $r_{\text{h,v}}$ is the vapor hydraulic radius.

1.3   Research gap and focus areas

In light of the above discussion and, more especially, some of the limitations associated with past research, we outline below the two principal problems to be tackled in this work. The first of these is theoretical and considers the analogue of the heat pipe capillary limiting curve for the case of thermosyphons. The second problem is experimental and considers the performance impact of changing from one to another kind of refrigerant. Details are described in the following two paragraphs.

As shown in figure 1.3, various parameters impose limitations on the steady state operations of heat pipes [1, 59]. Previous research has provided a detailed description of the criteria governing heat transfer limitations in heat pipes [1]. One common limitation in low-temperature heat pipes is the capillary limit [1, 62]. Attempts to exceed this limit lead to dry-out in the evaporator section, characterized by a sudden increase in wall temperature. However, there are scenarios where the capillary limit is irrelevant, such as when the wick is flooded or removed, making gravity dominant over capillarity. In horizontally oriented thermosyphons, the liquid flow is driven by the depth difference between the condenser and evaporator. As the inclination angle increases (with the evaporator below the condenser), the depth difference may decrease or disappear, and the liquid flow is then driven by the elevation difference between the two sides of the thermosyphon [62]. However, a deep liquid pool in the condenser can hinder radial heat transfer, especially with working fluids of low thermal conductivity. Therefore, for horizontally oriented thermosyphons, it is important to strike a balance that ensures optimal liquid pool depth. Deviating from this optimum depth can result in poor performance and increased material costs, particularly if the working fluid is expensive. Research conducted to date fails to provide the optimal fill ratio for a thermosyphon, and does not quantify the consequences of either overfilling or underfilling the thermosyphon. Additionally, the literature does not adequately

emphasize the use of the hydrostatic limiting curve as an alternative to the capillary limiting curve.

In response to global warming, industries are consistently striving to minimize greenhouse gas emissions [63, 64]. Considering the significant environmental impact of fluorocarbon refrigerants, industries are now transitioning to next-generation refrigerants [65–67]. R513a refrigerant boasts a remarkably smaller Global Warming Potential (GWP) compared to its predecessor, R134a [68]. This makes R513a a potential candidate to replace R134a as a suitable alternative. Therefore, it is crucial to thoroughly consider the impact of these modifications before transitioning to this new refrigerant. Essentially, R513a requires changing fill mass or system design modifications to ensure consistent performance. Research has explored the transition from R134a to R513a in various HVAC applications, including heat pumps, refrigerators, and other systems. However, there is limited research on transitioning from R134a to R513a in heat pipe applications. The heat pipe sector is growing fast but the research on the use of these novel refrigerants in heat pipes remains relatively unexplored and represents a novel area of study [69]. Unfortunately, the lack of research on the transition of heat pipes to R513a has led most companies to rely on traditional refrigerants.

The technical discussion of the thesis is divided into three chapters as described below.

1.3.1 Finding the optimum fill mass and hydrostatic limit in thermosyphon

In **Chapter 2**, we conduct a modeling analysis of a thermosyphon (in particular its adiabatic section) in order to examine the variation of heat flux ($\dot{Q}$) with different fill fractions. We thereby define the maximum achievable heat flux of the thermosyphon. These results are instrumental in establishing the thermosyphon operational limits.

In particular, our analysis allows us to define a "hydrostatic limit," which serves as the analogue of the capillary limit for heat pipes (where surface tension, not gravity, is responsible for liquid flow). By comparing the results of the thermosyphon model with those of a heat pipe, we are able to establish selection criteria for choosing between a thermosyphon and a heat pipe.

1.3.2 Transition to new generation refrigerants with low global warming potential in both heat pipe and thermosyphon applications

Chapter 3 asks how one can make a seamless transition to next-generation refrigerants with low global warming potential (GWP). We report upon multiple experiments that vary the fill fraction and inclination angle to assess implications for the following working fluids: R134a (old refrigerant) and R513a (new refrigerant). Ultimately, we compare the behavior of these refrigerants under different operating conditions and formulate a strategy for transitioning from one to the other refrigerant.

1.3.3 Industrial software for heat pipe design and optimisation

In **Chapter 4**, we describe a software called LowTHeR (standing for "Low Temperature Heat Recovery") specifically tailored for the design and optimization of heat pipes, utilizing the most up-to-date research in the field. This software is primarily geared toward industrial applications and encompasses various essential components. It commences with refrigerant selection, followed by the option for new design or design optimization to facilitate retrofit applications, taking into account factors such as envelope dimensions and wick specifications. Additionally, the software incorporates a heat pipe bank module to further augment its functionality. Moreover, leveraging the experimental data obtained from Chapter 3, we successfully optimized heat pipe design in a particular setting that is relevant to the interests of our industrial sponsor.

Chapter 2

On the hydrostatic limit for thin film flow with applications to thermosyphons

2.1 Introduction

Heat pipes are remarkable devices for efficient heat transfer, garnering significant attention across engineering fields due to their exceptional ability to transport large amounts of thermal energy over considerable distances while maintaining minimal temperature differentials [58]. This characteristic has made them a preferred choice in applications like electronics cooling and solar energy systems [59]. One of their key advantages is their significantly higher thermal conductivity compared to materials like copper, which are known for their low resistance to heat diffusion. Consequently, heat pipes offer a reliable and attractive solution for various heat transfer needs [70]. Given these attributes, it's crucial to fully comprehend the operational principles, design considerations, and performance traits of heat pipes to effectively tackle contemporary heat transfer challenges.

Heat pipes find immense utility in modern technology, particularly in the cooling of electronic devices, computer processors, LED lighting, solar panels, and high-performance computing systems [71–74]. They function as passive devices that facilitate heat transfer from one location to another without requiring external energy

25

input [75]. These devices contain a low-boiling-point liquid such as water or ammonia, which undergoes evaporation and condensation to achieve heat transfer. The heat exchange process involves applying heat to one end, leading to the liquid evaporating and moving along the pipe to the cooler end. At this point, the liquid condenses and releases its latent heat of vaporization. The condensed liquid then returns to the hot end to repeat the cycle. The return of the liquid can be facilitated either through capillary forces in a wick or through gravity forces, with the latter case often termed a thermosyphon.

The efficient operation of heat pipes is governed by various parameters that impose constraints on both steady-state and transient processes [1, 59]. These limitations encompass phenomena such as the frozen startup (vicious limit), capillary limit, sonic limit, entrainment limit, and boiling limit. These factors can lead to heat transfer limitations depending on the heat pipe's size, shape, working fluid, wick structure, and operating temperature. The most restrictive limit among these considerations determines the maximum heat transport capacity of the heat pipe at a given temperature [1].

A common limitation encountered in low-temperature heat pipes is the capillary limit [1, 62]. This arises from the incapability of a specific capillary structure to provide sufficient return flow of condensed liquid to the evaporator section of the heat pipe. In such cases, the sum of pressure drops experienced by the liquid and vapor surpasses the maximum capillary pressure the wick can sustain. Pushing beyond this capillary limit results in dry-out within the evaporator section, leading to a sudden increase in wall temperature.

However, there are instances where the capillary limit becomes less relevant. For example, when the wick is flooded with liquid, removed altogether, or in the case of a long and inclined heat pipe where capillarity takes a back seat to gravity. To explore these scenarios, the focus shifts towards studying horizontal and inclined thermosyphons (heat pipes without wicks). Here, the capillary limit is replaced by

an analogous hydrostatic limit [76–78].

In thermosyphons oriented horizontally, liquid flow results from the varying depths of liquid in the condenser and evaporator sections. As the inclination angle increases, the liquid depth difference may decrease or vanish, causing flow to be driven by elevation disparities on either side of the thermosyphon [62]. However, deep liquid pools in the condenser might hinder radial heat transfer, especially if the working fluid has low thermal conductivity. Thus, a balance must be struck in the liquid pool depth for thermosyphons oriented horizontally. Deviating from this optimal depth could lead to poor performance and increased material costs, particularly if the working fluid is expensive.

In our approach, we primarily examine steady-state liquid flow, omitting phase changes in the evaporator and condenser sections. Our aim is to determine the fill ratio that optimizes thermosyphon performance for a specific working fluid, inclination angle, and heat load. Traditional thermosyphon models typically overlook the incremental flow resistance caused by variations in liquid film thickness. By considering these factors, we aim to identify scenarios where thermosyphon performance matches or surpasses that of conventional heat pipes. Additionally, our work sheds light on performance restrictions posed by hydrostatic limitations, complementing existing heat pipe operating curves that primarily apply to capillary-driven flow.

The work is divided into the following sections: Section 2 outlines a theoretical model that, for different operating conditions, links the variation of heat flow with liquid depth. We build upon this analysis in Section 3 by defining the variation of the maximum rate of heat transfer, which in turn defines the hydrostatic limit. The connection between this hydrostatic limit and the corresponding capillary limit for heat pipes is examined in Sections 4 and 5, in the complementary theoretical model of a heat pipe is presented and discussed. Section 6 wraps up with conclusions and ideas for further study.

For future reference, we list in table 2.2 key variables with associated SI units and typical values. In the case of nondimensional variables, only units and descriptions are provided.

Table 2.1: List of refrigerant properties with units and typical values.

Refrigerant Properties	Typical value	Unit
Liquid density (ρ_l)	1000	kg/m^3
Liquid dynamic viscosity (μ_l)	10^{-3}	kg/(m·s)
Liquid kinematic viscosity (ν_l)	10^{-6}	m^2/s
Capillary length (l_{cap})	2	mm
Latent heat of vaporization (h_{fg})	2.26×10^6	J/kg
Ratio of specific heats ($\gamma_{\text{vapor}} = c_p/c_v$)	1.327	–
Ideal gas constant (R)	8.314	J/(mol·K)
Molecular mass (m_v)	18.02	g/mol
Vapour density (ρ_v)	1.3	kg/m^3
Vapour dynamic viscosity (μ_v)	18×10^{-6}	kg/(m·s)
Liquid thermal conductivity at 25°C (K_f)	0.607	W/(m·K)
Sidewall thermal conductivity (K_s)	398	W/(m·K)
Room temperature (T_R)	300	K

2.2 Thermosyphon operation

The rate of heat transfer in a thermosyphon is often computed using a thermal network analysis. Accordingly, and using a generalization of Ohm's law, thermal resistances are defined for each instance of conductive or convective heat transfer [1, 61]. Such an approach naturally emphasizes heat transfer in a direction perpendicular to the long axis of the thermosyphon for which conductive effects (whether through the thermosyphon sidewall or through the layer of liquid that accumulates in the condenser) are especially relevant. On the other hand, and considering a flow of heat

Table 2.2: List of geometrical parameters, values, and other variables.

Geometrical Dimensions

Heat pipe height (H)	50	mm
Heat pipe width (ζ)	100	mm
Heat pipe evaporator length (L_e)	0.25	m
Heat pipe condenser length (L_c)	0.25	m
Heat pipe adiabatic length ($L_a = L$)	1	m

Other Variables

Gravity (g)	9.81	m/s^2
Condenser temperature (T_c)		°C or K
Evaporator temperature (T_e)		°C or K
Temperature range ($\Delta T = T_e - T_c$)		°C or K
Condenser liquid depth (h_c)		mm
Evaporator liquid depth (h_e)		mm
Liquid mass flow rate ($\dot{m}_l$)		kg/s
Vapor mass flow rate ($\dot{m}_v$)		kg/s
Liquid profile ($h = h(x)$)		mm
Inclination angle (θ)		°

and mass in the axial direction, a thermosyphon can only transfer as much heat as can be carried by the vapor generated in the evaporator. In turn, evaporation is only possible if there is an adequate return flow of liquid from the condenser. Thus there is an essential trade-off for thermosyphons that are oriented close to horizontal: if the mass of liquid is too large, conductive resistances in the condenser will likewise be large such that the overall rate of heat transfer, $\dot{Q}$, is low. Conversely, if the mass of liquid is too small, there will be an insufficient hydrostatic driving force for liquid flow leading to dry-out and a similar (or perhaps more dramatic) decrease in $\dot{Q}$. The trade-off in question can be understood in graphical terms with reference to a figure such as figure 2.1 (a), which shows the variation of $\dot{Q}_{\text{op}}$ and $\dot{Q}_{\text{hydro}}$ with $\bar{h}$, the average

Table 2.3: List of superscripts, consolidated variables, and abbreviations.

Superscript	meaning
$(\ )^r$	Radial direction
$(\ )^a$	Axial direction

Consolidated variables	Values	Unit
$\beta = \rho_l \mathrm{g}/\mu_l$	9.81×10^6	s^{-1}
$\Pi_l = \frac{1}{\mu_l}\left(\frac{\partial P_l}{\partial x} - \rho_l g_x\right)$		
$\Pi_v = \frac{1}{\mu_v}\left(\frac{\partial P_v}{\partial x} - \rho_v g_x\right)$		

Abbreviation	Meaning	Unit
$\dot{Q}$	Heat flux	W
$\dot{Q}_{\mathrm{max}}$	Maximum heat flux	W

liquid depth along the length of the thermosyphon. Here, $\dot{Q}_{\mathrm{op}}$ represents the operational heat flux obtained through the thermal network, while $\dot{Q}_{\mathrm{hydro}}$ represents the hydrostatic driven heat flux obtained by solving the liquid mass flow rate. The steady state thermosyphon operating point (indicated, for different evaporator section liquid depths, by the black circles) corresponds to the point of intersection of the $\dot{Q}_{\mathrm{op}}$ and $\dot{Q}_{\mathrm{hydro}}$ curves.

For a fixed ΔT, it is clear from figure 2.1 (a) that when $\bar{h}$ increases $\dot{Q}_{\mathrm{op}}$ decreases, due to an increase in radial thermal resistance. On the other hand, as $\bar{h}$ increases, the corresponding $\dot{Q}_{\mathrm{hydro}}$ increases due to an increase in the driving force associated with a larger hydrostatic pressure. Additionally, figure 2.1 (a) illustrates that as h_e decreases, $\dot{Q}_{\mathrm{hydro}}$ increases. This effect occurs because, for a fixed $\bar{h}$, a decrease in h_e results in more liquid being available in the condenser, leading to a larger hydrostatic pressure difference between one and the other end of the thermosyphon.

Of course, the trade-off illustrated in figure 2.1 (a) can be modified by the addition

of a wick, which changes the driving force for liquid flow from hydrostatic to capillary and changes the thermosyphon into a heat pipe, wicks that are flooded achieve little or no capillary pumping [59]. Also, and beyond a small angle of inclination, capillary pumping is, in any event, subordinate to hydrostatic pressure differences. Therefore one does not necessarily need to consider the wick in optimizing heat transfer, that is unless $\theta = 0°$ and/or heat pipe is short in length, as might apply in compact electronics equipment.

Motivated by this discussion, we undertake a theoretical study of the liquid fill fraction that maximizes $\dot{Q}$ given the aforementioned constraints. In so doing, we separately consider the overall heat flux (as estimated using a thermal network analysis) and the axial heat flux (as determined from the lubrication equations of fluid flow). We then equate these two expressions as is appropriate for steady conditions. The fundamental investigation in question is interesting in its own right and also provides a helpful point of comparison between thermosyphon and heat pipe design.

2.2.1   Modelling approach

Thermal network analysis

We apply a thermal network analysis to evaluate the overall thermal resistance, R, associated with heat flow along a thermosyphon. This overall resistance is composed of a number of constituent components as shown in figure 2.1 (b). The resistance terms are defined as follows: R^r_{shell} represents the shell resistance in the radial direction, R^r_{int} denotes the resistance at the liquid-vapor interface, R^a_{vapor} refers to the axial vapor resistance, $R^a_{\text{shell}} + R^a_{\text{wick}}$ represents the combined axial resistance of the shell and wick, $R^{r,\text{evap}}_{\text{wick}}$ indicates the radial wick resistance in the evaporator, and $R^{r,\text{cond}}_{\text{wick}}$ signifies the radial wick resistance in the condenser. In the context of a thermosyphon, the resistance values $R^{r,\text{evap}}_{\text{wick}}$ and $R^{r,\text{cond}}_{\text{wick}}$ represent the resistance caused by the liquid pool in the evaporator and condenser, respectively. These resistance
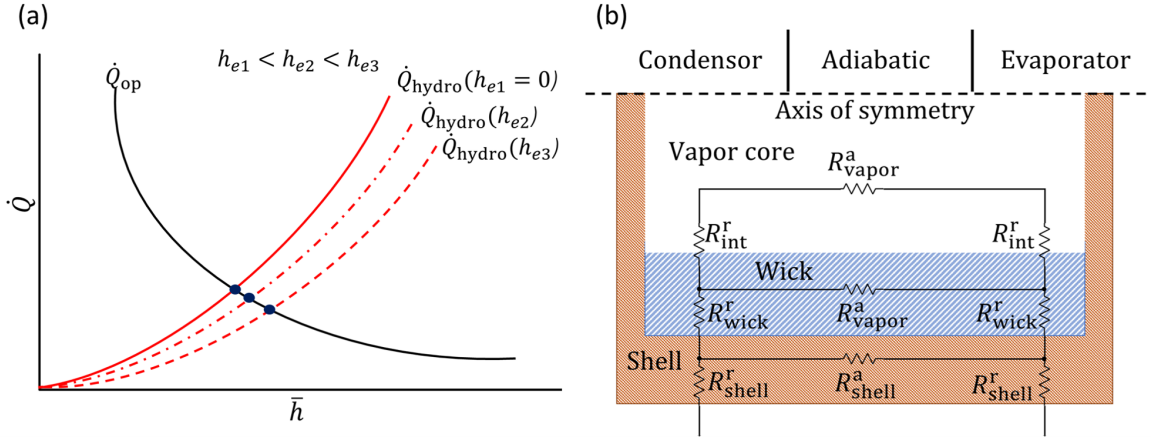
Figure 2.1: (a) variation of $\dot{Q}_{\mathrm{op}}$ and $\dot{Q}_{\mathrm{hydro}}$ (b) Thermosyphon schematic illustrating the thermal resistance model. (Image not to scale)

values can be determined by substituting the thermal conductivity of the wick with the thermal conductivity of the liquid in (2.2). From the order-of-magnitude scaling analysis given in table 2.4, the value of R is set primarily by the thermal resistances associated with the saturated wick (R^r_{wick}) and with the wall or shell material (R^r_{shell}). Whereas R^r_{shell} is approximately the same in the evaporator and condenser, R^r_{wick} is not because of the different depths of liquid measured at these opposite ends of the heat pipe or thermosyphon. It is therefore necessary to distinguish between $R^{r,\mathrm{cond}}_{\mathrm{wick}}$ and $R^{r,\mathrm{evap}}_{\mathrm{wick}}$, which respectively represent the thermal resistances associated with the liquid layer in the condenser vs. in the evaporator. Note finally that the corresponding magnitude of the resistance term, $R^a_{\mathrm{shell}} + R^a_{\mathrm{wick}}$, in the axial direction is so large that heat transfer by liquid advection is, for all intents and purposes, the only means of transporting heat along the long axis.

To simplify the analysis, we consider that heat is added or removed only through the bottom (possibly inclined) surface of the (rectilinear) evaporator. We therefore consider the two side surfaces and top surface to be insulated. Due to the vertical variation of temperature (and therefore of density) within the liquid, the liquid in the condenser is stably-stratified such that heat transfer occurs via conduction.

In contrast, heat transfer in the evaporator occurs via pool boiling and is therefore significantly enhanced by rising bubbles. Accordingly, the thermal resistance of the condenser is an order of magnitude larger than that of the evaporator, i.e. $R_{\text{wick}}^{r,\text{cond}} \gg R_{\text{wick}}^{r,\text{evap}}$ [79–81]. This disparity persists even when the depth of the liquid in the evaporator, h_e, is large.

Leveraging the above assumptions, the overall thermal resistance for the heat pipe or thermosyphon depicted in figure 2.1 can be estimated as follows:

$$R = \frac{\delta}{K_s \zeta L_c} + \frac{\delta}{K_s \zeta L_e} + \frac{h_c}{K_f \zeta L_c}. \tag{2.1}$$

Here, δ and K_s refer to the thickness and thermal conductivity of the shell material, respectively, h_c is the depth of the liquid layer in the condenser, and K_f is the thermal conductivity of the (liquid) refrigerant. Finally, ζ represents the width of the rectangular channel and L_c and L_e represent the respective lengths of the condenser and the evaporator. With R to hand, the overall heat flux can be determined from

$$\dot{Q} = \dot{Q}_{\text{radial}} = \frac{\Delta T}{R}. \tag{2.2}$$

Here the temperature range $\Delta T = T_{\text{e}} - T_{\text{c}}$ in which T_e and T_c respectively indicate the evaporator and condenser temperatures. From $\dot{Q}$, the mass flow rates of liquid ($\dot{m}_l$) and of vapor ($\dot{m}_v$) can be evaluated from $\dot{m}_l = -\dot{m}_v = \dot{Q}/h_{fg}$, where h_{fg} is the latent heat of condensation. Note that $\dot{m}_l$ and $\dot{m}_v$ have opposite signs because the flows they represent are anti-parallel. Note also that $\dot{m}_l$ and $\dot{m}_v$ are, at steady state, equal to the rates of evaporation and condensation.

Lubrication flow analysis

To derive an independent expression for $\dot{m}_l$, we consider the flow illustrated schematically in figure 2.2. Thus do we examine the thermosyphon adiabatic section, which exhibits a continuous (and non-linear) variation of depth, h, of the liquid layer from

Table 2.4: Thermal resistance of the various heat pipe or thermosyphon components as illustrated in figure 2.1 (b).

Resistance Term	Magnitude ($^\circ$C/W)
R^r_{shell}	10^0
$R^{r,\mathrm{cond}}_{\mathrm{wick}}$	10
$R^{r,\mathrm{evap}}_{\mathrm{wick}}$	10^{-1}
R^r_{int}	10^{-5}
R^a_{vapor}	10^{-8}
$R^a_{\mathrm{shell}} + R^a_{\mathrm{wick}}$	10^3

the condenser to the evaporator. Because attention is focused on the adiabatic section, it is appropriate to assume that the liquid maintains a constant depth of h_c throughout the condenser section, which ends at $x = 0$, and a constant depth of h_e throughout the evaporator section, which starts at $x = L$ [61].

Liquid flows from the condenser to the evaporator due to the difference of hydrostatic pressures between $x = 0$ and $x = L$. The pressure difference in question depends on θ, h_c, h_e and $\rho_l - \rho_v (\simeq \rho_l)$. Consistent with figure 2.2 and with our previous discussion, we consider, for reasons of algebraic simplicity, a 2D rectilinear flow where the fluid thermophysical properties (e.g. liquid density ρ_l, liquid viscosity μ_l and latent heat of vaporization h_{fg}) are constant along the length and only depend on the operating temperature, T_{op}. Additionally, we assume steady conditions, for which h_c/L and the Reynolds number (Re $= \rho_l U h_c/\mu_l$) are small enough to justify the use of a lubrication approximation. In the definition of the Reynolds number, the characteristic velocity can be determined by balancing viscous forces with those associated with hydrostatic pressure, yielding $U = \rho g h_c^3/\mu L$. By applying the lubrica-

34
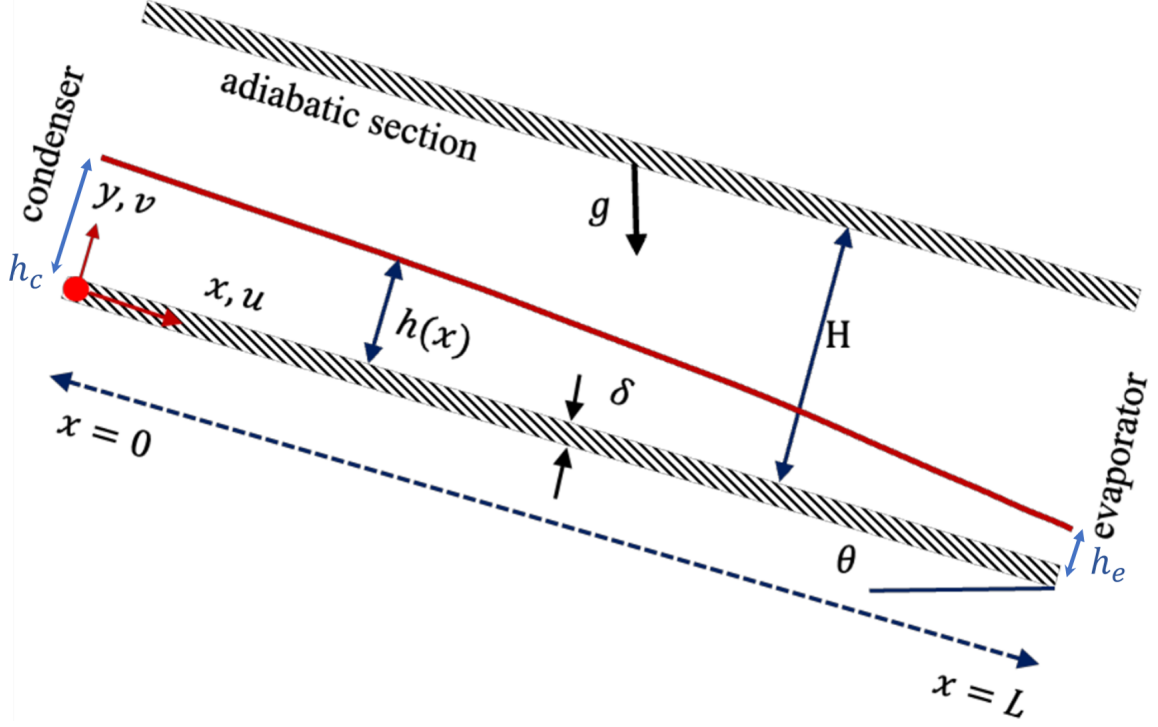
Figure 2.2: Variation of liquid depth in a rectangular thermosyphon at an inclination angle θ. The mean liquid depth along the length is represented by $\bar{h}$ in equation 2.10.

tion approximation, i.e., $\text{Re} \frac{h_c}{L} \ll 1$, and using as boundary conditions a no-slip basal condition, i.e. $u_l(x,0) = 0$, and a stress-free interfacial condition, i.e. $\frac{\partial u_l}{\partial y}(x,h) = 0$, we can deduce the following expression for the liquid velocity profile:

$$u_l(x,y) = \left(\frac{1}{\mu_l} \frac{\partial P_l}{\partial x} - \frac{\rho_l g_x}{\mu_l} \right) \left(\frac{y^2}{2} - hy \right) \tag{2.3}$$

Here the subscript l represents the liquid phase such that P_l is the pressure measured in the liquid. Also, $g_x = g \sin \theta$ and $g_y = g \cos \theta$. This latter term is important when expressing force balance in the cross-stream, rather than streamwise, direction, i.e.

$$\frac{\partial P_l}{\partial y} = -\rho_l g_y \tag{2.4}$$

Integrating (2.4) yields

$$P_l(x,y) = \rho_l g_y (h - y) + P_v \quad \Rightarrow \quad \frac{\partial P_l}{\partial x} \simeq \rho_l g_y \frac{\partial h}{\partial x} \tag{2.5}$$

In evaluating gradients in the streamwise direction, we have deliberately assumed $\partial P_v / \partial x$ to be small compared to $\rho_l g_y \partial h / \partial x$. We discuss the validity of this assumption

in subsection 2.2.4. Substitution of (2.5) into (2.3) shows that

$$u_l(x, y) = \frac{g}{\nu_l} \left(-\cos\theta \frac{\partial h}{\partial x} + \sin\theta \right) \left(hy - \frac{y^2}{2} \right)$$

(2.6)

Here $\nu_l \equiv \mu_l/\rho_l$ is the liquid kinematic viscosity. Using (2.6), $\dot{m}_l$ can be determined via integration, i.e.

$$\dot{m}_l = \rho_l \zeta \int_0^h u_l \, \mathrm{d}y$$

(2.7)

Solving for $\dot{m}_l$ therefore requires knowledge of h, a formula for which can be derived by integrating the mass continuity equation. Indeed, and by following the steps outlined in [82], it can ultimately be shown that

$$h^3 \cos\theta \frac{\mathrm{d}h}{\mathrm{d}x} - h^3 \sin\theta = C_1$$

(2.8)

The constant C_1 is determined using $\dot{Q}_{\text{radial}}$ with details provided in subsection 2.2.3.

2.2.2   The horizontal thermosyphon

Although our prior analysis is applicable to all inclination angles, we are especially interested in quantifying thermosyphon performance when $\theta = 0°$, whereby

$$h(x) = \left[h_c^4 \left(1 - \frac{x}{L} \right) + \frac{x}{L} h_e^4 \right]^{\frac{1}{4}}.$$

(2.9)

Using (2.9), we can determine the average liquid depth, $\bar{h}$, in the interval $0 \leq x \leq L$ as follows:

$$\bar{h} = \frac{1}{L} \int_0^L h(x) \, \mathrm{d}x = \frac{4}{5} \left(\frac{h_c^5 - h_e^5}{h_c^4 - h_e^4} \right)$$

(2.10)

Equation (2.9) also allows evaluation of $\dot{m}_l$ and $\dot{Q}$ from

$$\dot{m}_l = \frac{\rho_l g \zeta}{12 \nu_l L} \left(h_c^4 - h_e^4 \right) = \frac{\dot{Q}}{h_{fg}}$$

(2.11)

By combining (2.2) and (2.11), it can be shown that

$$h_e = \left(h_c^4 - \frac{\Delta T}{R} \frac{12 \nu_l L}{h_{fg} \rho_l g \zeta} \right)^{\frac{1}{4}}$$

(2.12)
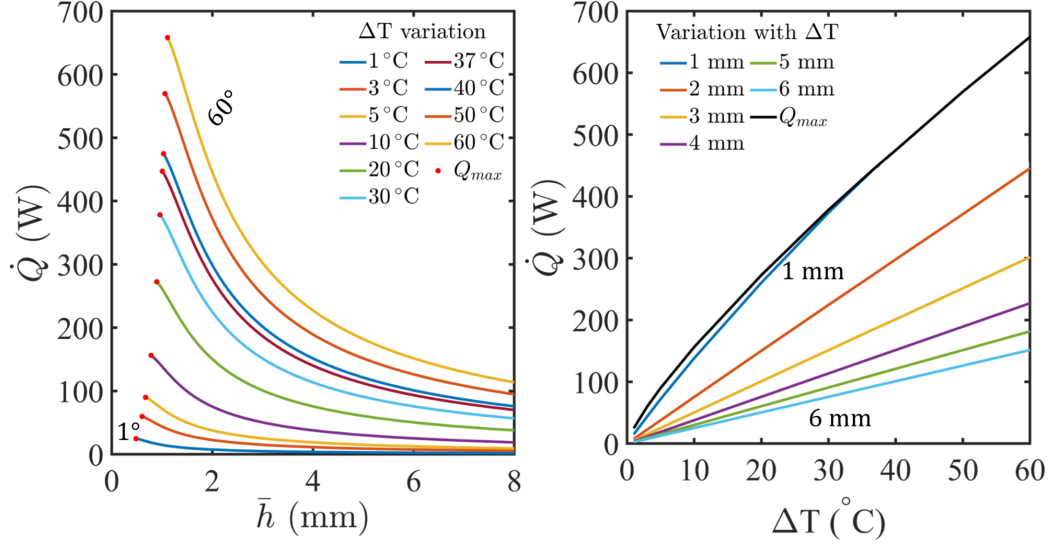
Figure 2.3: (a). Variation of $\dot{Q}$ with $\bar{h}$ for different ΔT at $\theta = 0°$ (b). Variation of $\dot{Q}$ and $\dot{Q}_{\max}$ with ΔT for different $\bar{h}$ at $\theta = 0°$.

From (2.12), the solution methodology is straightforward. The input parameter h_c is used to calculate $\dot{Q}$ from (2.1) and (2.2). With h_c and $\dot{Q}$ to hand, (2.12) is applied to solve for h_e. Utilizing h_e and h_c, we can then calculate $\bar{h}$ from (2.10), from which the variation of $\dot{Q}$ with $\bar{h}$ can be ascertained. We limit our analysis to situations where $h_e \geq 0.5\,\mathrm{mm}$, $0.5\,\mathrm{mm}$ being a threshold value intermediate to a characteristic material roughness scale and the capillary length ($\simeq 2.7\,\mathrm{mm}$ for water at ambient temperature and pressure).

Figure 2.3 (a) shows $\dot{Q}$ vs. $\bar{h}$ for various evaporator-to-condenser temperature differences, ΔT. As $\bar{h}$ increases, $\dot{Q}$ decreases due to an increase in the thermal resistance caused by the corresponding increase in h_c. Whereas this last statement suggests minimizing the mass of working fluid added to the thermosyphon, it is important to avoid decreasing the fill mass below the critical point, shown by the series of red dots, associated with thermosyphon dry out. To the left of the red dots, $\bar{h}$ is too small to sustain the requisite liquid flow rate; in mathematical terms, the combination of (2.2) and (2.11) does not admit a physically-acceptable solution, i.e. one satisfying

$h_e \geq 0.5\,\text{mm}$. Figure 2.3 (a) also shows that as ΔT increases, there is an up - and rightward shift in the $\dot{Q}$ vs. $\bar{h}$ curves. Increasing ΔT increases $\dot{Q}$ from (2.2), which requires a larger $h_c - h_e$ to drive the liquid from the condenser to the evaporator. Because h_e is bounded from below, larger $h_c - h_e$ necessitates an increase in h_c. As a consequence, and consistent with the above commentary, (i) R increases from (2.1) thereby negating some of the increase that would otherwise be observed in $\dot{Q}$, and, (ii) the minimum possible value of $\bar{h}$ also increases.

Figure 2.3 (b) reconsiders the results of figure 2.3 (a) but now shows $\dot{Q}$ vs. ΔT for different $\bar{h}$. The positive slopes of the curves indicate that $\dot{Q}$ increases with increasing ΔT regardless of the average liquid depth. At small $\bar{h}$ (1 mm), the thermosyphon transports a lot of heat but is only operational until 38°C; any further increase in ΔT causes the thermosyphon to reach the dry-out limit. By contrast if the thermosyphon were filled to a greater extent, it would not achieve as large a $\dot{Q}$ for moderate temperature differences. However, the thermosyphon in question would exhibit a broader (possibly much broader) range of operation vis-à-vis ΔT.

2.2.3   The inclined thermosyphon

The results of subsection 2.2.2 are limited to the case $\theta = 0°$. Oftentimes, thermosyphons are inclined (condenser above the evaporator); this subsection extends the discussion to such a scenario. Equation (2.8) is solved using the boundary condition $h(0) = h_c$. By combining (2.6), (2.7) and (2.8), we find that

$$\dot{m}_l = \rho_l \zeta \frac{\rho_l g}{\mu_l} \left(-\cos\theta \frac{\mathrm{d}h}{\mathrm{d}x} + \sin\theta \right) \frac{h^3}{3} = \frac{\dot{Q}}{h_{fg}} \qquad (2.13)$$

To simplify the expression for $\dot{m}_l$ (2.13), we utilize an equation for $\mathrm{d}h/\mathrm{d}x$ from (2.8). Then expressing $\dot{m}_l$ in terms of the overall heat flux using (2.2) yields as the
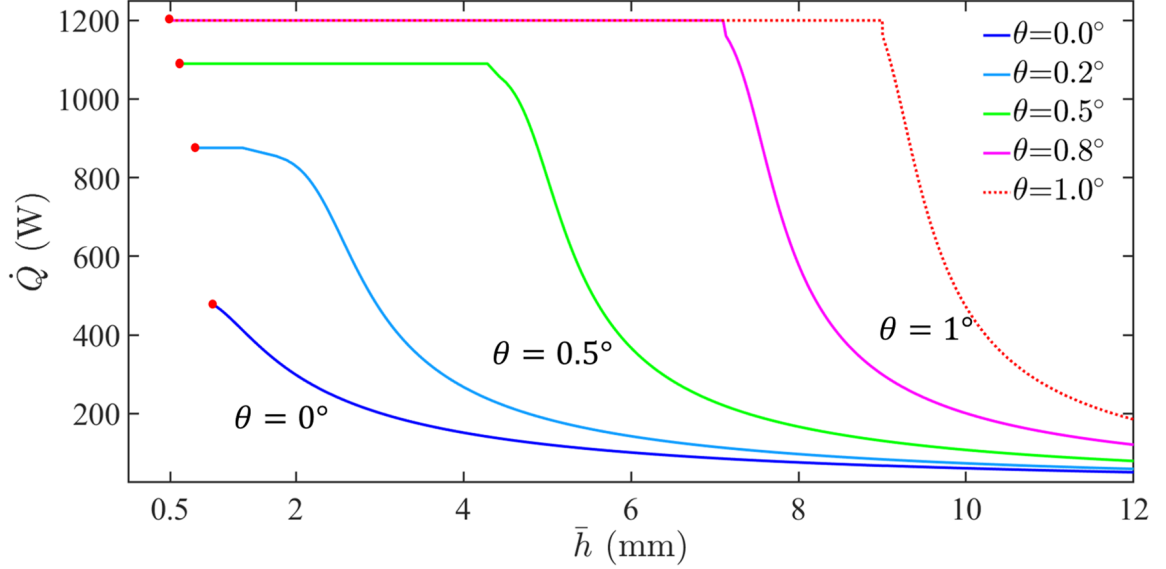
Figure 2.4: Variation of $\dot{Q}$ with $\bar{h}$ for different inclinations (θ) with $\Delta T = 40°$C.

solution for C_1

$$C_1 = -\frac{3\nu_l \dot{m}_l}{\rho_l g \zeta} = -\frac{3\nu_l}{\rho_l g \zeta} \frac{\Delta T}{R \, h_{fg}} \tag{2.14}$$

Given the input values of h_c and ΔT, the value of C_1 is determined using (2.14). Subsequently, we solve (2.8) and (2.10) to obtain the profiles of $h(x)$ and $\bar{h}$, respectively. The derived expression for $h(x)$ allows us to determine h_e and verify the acceptability of the solution i.e. by ensuring $h_e \geq 0.5$ mm.

Figure 2.4 shows the variation of $\dot{Q}$ with $\bar{h}$ for different θ and $\Delta T = 40°$C. As expected, the rate of heat transfer increases with the tilt angle θ: as the tilt angle increases, additional liquid tends to accumulate in the evaporator rather than spreading across the condenser. Correspondingly, the conductive resistance $R_{\text{wick}}^{r,\text{cond}}$ decreases. Moreover, and for sufficiently long thermosyphons, increasing θ even by a small amount significantly increases the driving force for liquid flow because $L \sin\theta$ may be comparable to, or larger than, $h_c - h_e$. Thus the resistance to heat transfer decreases whether measured with reference to the cross-flow or streamwise directions. In contrast to the horizontal thermosyphon case, the $\theta > 0°$ curves of figure 2.4 exhibit

a low-level plateau. In physical terms, the plateau signifies a dry condenser, i.e. a condenser for which liquid immediately depletes as it flows downslope towards the evaporator. Correspondingly, the plateau elongates (and the curves shift leftward) as θ increases. Thus an advantage of an inclined thermosyphon is that its operation is less sensitive to small variations in the working fluid fill mass. In other words, thermosyphon performance as measured by $\dot{Q}$ is relatively insensitive to minor or even significant changes of $\bar{h}$ as might arise due to a slow leakage of working fluid.

2.2.4 Thermosyphon modeling with vapor counter-flow

Our analysis up till now has ignored the dynamic influence of a vapor counter-flow. This influence is potentially significant: the vapor, whose mass flow rate must be equal and opposite to that of the liquid, exerts a shear stress on the liquid and results, therefore, in a deformation of this film relative to the no vapor counter-flow case. In this subsection, we ask whether such deformations have a significant impact on the hydrostatic force that drives the liquid flow.

As discussed in subsection 2.2.1, after applying the lubrication ($\text{Re}\frac{h_c}{L} \ll 1$) and steady flow assumptions, the expression for u_l becomes

$$u_l = \frac{\Pi_l}{2}y^2 + b_1 y + b_2 \qquad 0 < y < h\,, \tag{2.15}$$

where

$$\Pi_l \equiv \frac{1}{\mu_l}\left(\frac{\partial P_l}{\partial x} - \rho_l g_x\right) \tag{2.16}$$

and b_1 and b_2 are to be specified by application of the boundary conditions discussed below. Meanwhile (2.5) can be solved by substituting $P_v(x,y) \approx P_v(x)$. Here P_v represents the vapor pressure and is only a function x and independent of y due to

the small vapor density. Accordingly, (2.5) must be modified as follows:

$$\frac{\partial P_l}{\partial x} = \rho_l g_y \frac{\partial h}{\partial x} + \frac{\partial P_v(x)}{\partial x} \qquad (2.17)$$

Extending the above methodology to the vapor counter-flow, we consider as the governing equation

$$u_v = \frac{\Pi_v}{2} y^2 + c_1 y + c_2, \qquad h < y < H \qquad (2.18)$$

where

$$\Pi_v \equiv \frac{1}{\mu_v} \left(\frac{\mathrm{d}P_v}{\mathrm{d}x} - \rho_v g_x \right) \qquad (2.19)$$

Here, ρ_v represents the vapor density, μ_v represents the vapor viscosity, and u_v and v_v respectively denote the vapor velocity in the x and y directions. Note that Π_v is only a function of x and it is independent of y. Note also that c_1 and c_2 are, as with b_1 and b_2, determined by application of boundary conditions. To wit, we consider the following:

$$(i) \; u_l(x, 0) = 0 \qquad (ii) \; \mu_l \frac{\partial u_l(x, h)}{\partial y} = \mu_v \frac{\partial u_v(x, h)}{\partial y}$$

$$(iii) \; u_l(x, h) = u_v(x, h) \qquad (iv) \; u_v(x, H) = 0$$

Application of the above boundary conditions ultimately yields

$$b_2 = 0$$

$$b_1 = \frac{-\frac{1}{2}\Pi_v(h - H)^2 - \frac{1}{2}\Pi_l h^2 + C_\mu \Pi_l h(h - H)}{h - C_\mu(h - H)}$$

$$c_1 = \frac{\frac{1}{2}\Pi_l h^2 + \frac{1}{2}\Pi_v(h^2 - H^2 - \frac{2}{C_\mu}h^2)}{\frac{1}{C_\mu}h + H - h}$$

$$c_2 = -c_1 H - \frac{1}{2}\Pi_v H^2$$

Here $C_\mu = \mu_l/\mu_v$. Note that C_μ and H are constants and do not depend on x or y. Even so, note that because $h = h(x)$, b_1, c_1 and c_2 are all likewise functions of x.

To find the variation of h with x, the liquid mass continuity equation can be used. More specifically, we integrate the continuity equation in differential form over height from $y = 0$ to $y = h$ and apply Leibnitz's rule to show that

$$0 = \frac{\partial}{\partial x} \int_0^h u_l \mathrm{d}y + \frac{\partial h}{\partial t}$$

At steady state, the above result can be rewritten as

$$0 = \frac{\mathrm{d}}{\mathrm{d}x} \int_0^h u_l \, \mathrm{d}y = \frac{\mathrm{d}}{\mathrm{d}x} \int_0^h \left(\frac{\Pi_l}{2} y^2 + b_1 y \right) \mathrm{d}y = \frac{\mathrm{d}}{\mathrm{d}x} \left(\frac{\Pi_l}{6} h^3 + \frac{b_1}{2} h^2 \right) = \frac{1}{6} \frac{\mathrm{d}(\Pi_l h^3 + 3 b_1 h^2)}{\mathrm{d}x}$$

Rearranging this last result gives

$$\frac{\mathrm{d}\Pi_l}{\mathrm{d}x} h^2 + 3\Pi_l h \frac{\mathrm{d}h}{\mathrm{d}x} + 3h \frac{\mathrm{d}b_1}{\mathrm{d}x} + 6b_1 \frac{\mathrm{d}h}{\mathrm{d}x} = 0 \tag{2.20}$$

To solve (2.20), we apply (2.2.4) and thereby calculate $\frac{\mathrm{d}b_1}{\mathrm{d}x}$ as follows:

$$\begin{aligned}
\frac{\mathrm{d}b_1}{\mathrm{d}x} &= \frac{\frac{1}{2}(h^2 - H^2)\frac{\mathrm{d}\Pi_v}{\mathrm{d}x} + \Pi_v h \frac{\mathrm{d}h}{\mathrm{d}x} - \Pi_l h \frac{\mathrm{d}h}{\mathrm{d}x} - \frac{1}{2}(h^2)\frac{\mathrm{d}\Pi_l}{\mathrm{d}x} + C_\mu h(h + H)\frac{\mathrm{d}\Pi_l}{\mathrm{d}x} + C_\mu \Pi_l h \frac{\mathrm{d}h}{\mathrm{d}x}}{h - C_\mu(h + H)} \\
&+ \frac{C_\mu \Pi_l(h + H)\frac{\mathrm{d}h}{\mathrm{d}x} + h(h + H)\frac{\mathrm{d}\Pi_v}{\mathrm{d}x} + \Pi_v(h + H)\frac{\mathrm{d}h}{\mathrm{d}x} + \Pi_v h \frac{\mathrm{d}h}{\mathrm{d}x}}{h - C_\mu(h + H)} \\
&+ \frac{(1 - C_\mu)\frac{\mathrm{d}h}{\mathrm{d}x}(\frac{1}{2}\Pi_v(h^2 - H^2)) - \frac{1}{2}\Pi_l h^2 + C_\mu \Pi_l h(h + H) + \Pi_v h(h + H)}{(h - C_\mu(h + H))^2} \tag{2.21}
\end{aligned}$$

With the above result to hand, h can be computed from (2.20). In principle, therefore, we can calculate $\dot{m}_l$ and $\dot{m}_v$ from

$$\dot{m}_l = \rho_l \zeta \int_0^h u_l \mathrm{d}y = \rho_l \zeta \left(\frac{\Pi_l}{6} h^3 + \frac{b_1}{2} h^2 \right) = \frac{\dot{Q}}{h_{fg}} \tag{2.22}$$

$$\dot{m}_v = \rho_v \zeta \int_h^H u_v \mathrm{d}y = \rho_v \zeta \left[\frac{\Pi_v}{6}(H^3 - h^3) + \frac{c_1}{2}(H^2 - h^2) + c_2(H - h) \right] = \frac{\dot{Q}}{h_{fg}} \tag{2.23}$$

When $\theta = 0°$, the gravity components of (2.16) and (2.19) can be simplified as $g_x = 0$ and $g_y = g$. Moreover, it is observed by many researchers that the vapor pressure variation through the adiabatic section of a thermosyphon or heat pipe is linear [1, 61]. The reason behind such a linear variation is that the adiabatic section experiences a negligible change of temperature and therefore of density. As the cross-sectional area also remains approximately constant ($h \ll H$), it is appropriate to
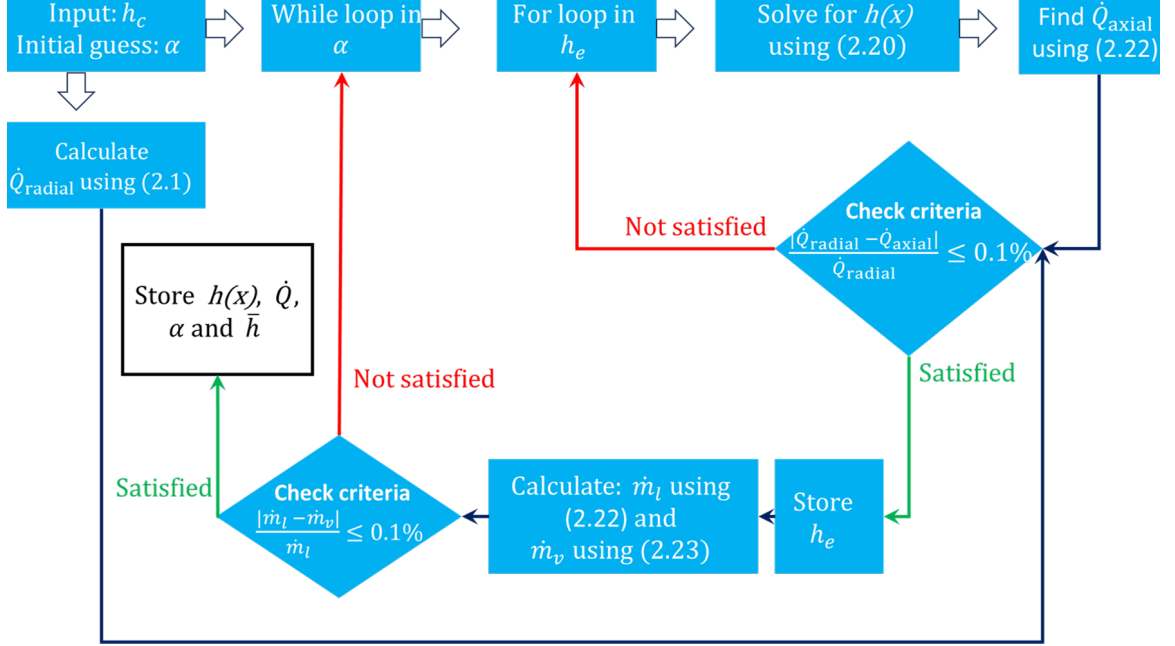
Figure 2.5: Solution steps for finding $h(x)$, α and $\bar{h}$.

assume that P_v is a linear function of x, or $P_v = \alpha x$. Here α is a constant that is independent of x and y. Accordingly, Π_v from (2.19) can be simplified as

$$\Pi_v = \frac{1}{\mu_v}\left(\frac{\partial P_v}{\partial x} - \rho_v g_x\right) = \Pi_v = \frac{\alpha - \rho_v g \sin\theta}{\mu_v} = \frac{\alpha'}{\mu_v} \tag{2.24}$$

Accordingly, Π_l from (2.16) can be written as

$$\Pi_l = \frac{1}{\mu_l}\left(\frac{\mathrm{d}P_l}{\mathrm{d}x} - \rho_l g_x\right) = \frac{\rho_l g \cos\theta\frac{\mathrm{d}h}{\mathrm{d}x} - \rho_l g \sin\theta + \alpha'}{\mu_l} = \frac{\rho_l g}{\mu_l}\left(\cos\theta\frac{\mathrm{d}h}{\mathrm{d}x} - \sin\theta\right) + \frac{\alpha'}{\mu_l} \tag{2.25}$$

Here $\alpha' = \alpha - \rho_v g \sin\theta$.

To solve for $h(x)$ from the second order differential equation (2.20), we apply the expressions for Π_v and Π_l from (2.24) and (2.25), respectively. Thereafter, we followed the four steps given in figure 2.5.

Building on figure 2.3 (a), figure 2.6 display the relationship between $\dot{Q}$ and $\bar{h}$ with

vapor counter-flow. The green curves in figure 2.6 closely resemble those of figure 2.3, indicating that the presence of vapor counter-flow does not significantly affect the liquid flow or profile. This observation can be attributed to two main factors: (i) the relatively low vapor velocities due to the small ratio of $\bar{h}$ to H, and (ii) the corresponding modest values of $\dot{m}_v$ and $\dot{Q}$. In the given range of $\dot{Q}$, the maximum value of α is less than $0.1\,\text{Pa·s/m}$. A careful comparison of figure 2.3 (a) and the green curves of figure 2.6 therefore reveals inconsequential differences of $\dot{Q}$, at least when the thermosyphon height measures $5\,\text{cm}$.

By contrast to this last paragraph, more significant differences may arise when the thermosyphon height is reduced. This fact is illustrated most clearly in figure 2.6, it is evident that reducing the value of H amplifies the influence of vapor counter-flow, particularly at higher values of $\dot{Q}$ or ΔT. When $\Delta T = 5°C$, $\dot{Q} < 100\,\text{W}$ and there is minimal shear stress at the interface due to the low velocity of the vapor. However, as the temperature range increases, differences become more pronounced due to the higher velocity of the vapor and the resulting increase in viscous resistance. The differences in question are especially prominent when $\bar{h}$ is comparatively small. Figure 2.6 further reveals that intensified interfacial shear stress shifts the curves down and to the right. This shift occurs because the thermosyphon requires a larger volume of liquid to generate a stronger driving force and compensate for the additional viscous resistance caused by vapor counter-flow. The downward shift is a consequence of the restriction on liquid return caused by viscous shear stress.

Although the results of figure 2.6 specifically consider a horizontal orientation for which $\theta = 0°$, similar results apply to the case of an inclined thermosyphon. Given this similarity, in particular the fact that the vapor counter-flow is most important for large ΔT and small $\bar{h}$ (i.e. large $\dot{Q}$), we do not include quantitative results here.
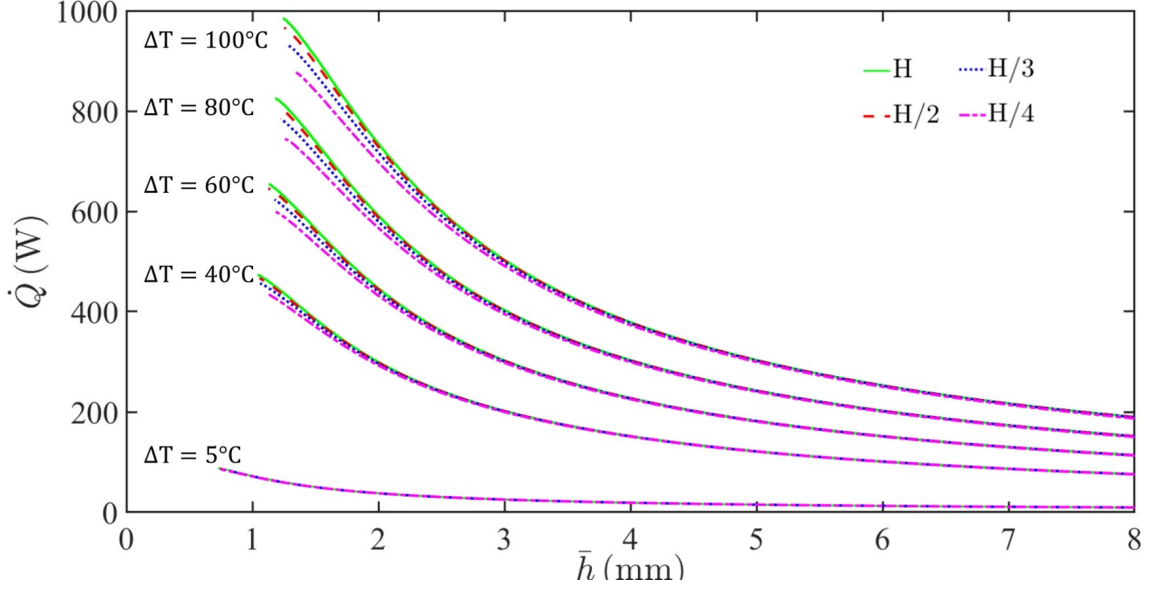
Figure 2.6: Variation of $\dot{Q}$ vs $\bar{h}$ with counter vapor flow at various ΔT (at $\theta = 0°$).

2.2.5 $\dot{Q}_{\max}$ variation for a thermosyphon

This section aims to determine the maximum heat transfer ($\dot{Q}_{\max}$) of a thermosyphon and explore how this quantity varies with different design parameters such as $\bar{h}$, L, and θ. Furthermore, we will analyze the influence of vapor counter-flow on $\dot{Q}_{\max}$ and identify situations where consideration of this counter-flow becomes necessary.

Variation of $\dot{Q}_{\max}$ with $\bar{h}$, θ and L

Figure 2.7(a) illustrates the impact of θ and $\bar{h}$ on $\dot{Q}_{\max}$. At $\theta = 0°$ and at the starting point where $\bar{h} = h_c = h_e = 0.5\,\mathrm{mm}$, $\dot{Q}_{\max} = 0$ because there is no hydrostatic driving force to cause a flow of liquid from the condenser to the evaporator. Additionally, as θ increases, when $\bar{h} = h_c = h_e = 0.5\,\mathrm{mm}$, the profile of $h(x)$ remains uniform in x. However, the resulting elevation difference between the two ends of the thermosyphon yields a pressure difference that leads to an increase of $\dot{Q}_{\max}$ with θ even though the thermosyphon is filled to its least possible extent.

Furthermore, figure 2.7 illustrates two trends regarding the variation of $\dot{Q}_{\max}$ with
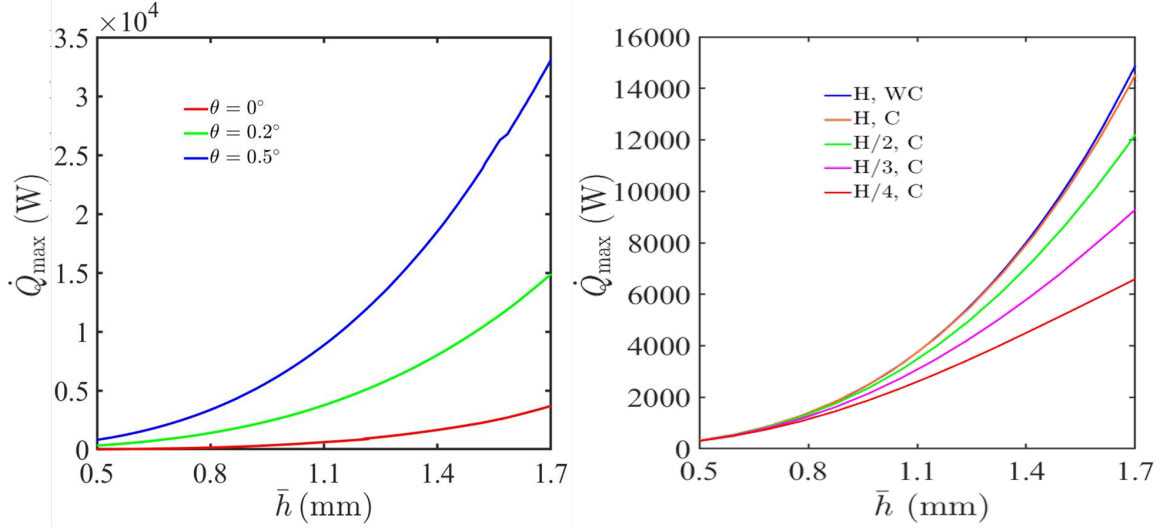
Figure 2.7: Variation of $\dot{Q}_{\max}$ in a thermosyphon (a) for different inclination angles, θ. Panel (b) highlights the influence of the vapor counter-flow w.r.t. H (for $\theta = 0.2°$). Here, "WC" refers to the configuration without vapor counter-flow, while "C" represents the configuration with counter vapor flow.

$\bar{h}$. Firstly, an increase in $\bar{h}$ leads to an increase in $\dot{Q}_{\max}$: the liquid-flow experiences reduced resistance while moving from the condenser to the evaporator when the liquid depth is greater. This is because the driving force for liquid flow is the height difference $h_c - h_e$. Increasing this height difference requires that both h_c and $\bar{h}$ increase, h_e being bounded from below e.g. by 0.5 mm. Furthermore, a larger $\bar{h}$ reduces flow resistance, resulting in reduced shear throughout the liquid layer. In other words, increasing $\bar{h}$ both enhances the driving force for fluid flow and reduces flow resistance.

Secondly, the thermosyphon tilt angle significantly impacts $\dot{Q}_{\max}$, as shown in figure 2.7(a). This figure differs from the previously presented figure 2.4 as figure 2.4 is plotted for a specific ΔT value of 40°C. $\dot{Q}_{\max}$ rapidly increases with θ and a barely perceptible 0.5° increase of inclination angle from $\theta = 0°$ to $\theta = 0.5°$ can, for the relatively long heat pipe of interest here, double the maximum possible heat flux. By extension, the maximum possible heat flux can increase by an order of magnitude if θ is increased from 0° to 4°. The enhancements just documented are due to the height

difference between the condenser and evaporator, with the additional factor of $L \sin \theta$ being added to $h_c - h_e$. Of course, when the thermosyphon orientation is horizontal, different considerations apply in that $L \sin \theta = 0$ and increasing L serves to decrease (rather than to increase) $\dot{m}_l$ and therefore $\dot{Q}$ – see e.g. (2.11).

Consistent with the discussion of the last paragraph, the length L also has a significant impact on both $\dot{Q}_{\max}$ and $\dot{Q}$, and these influences depend on θ. When $\theta = 0°$, $\dot{Q}_{\max}$ and $\dot{Q}$ are inversely proportional to L. As L increases, the magnitude of $\mathrm{d}h/\mathrm{d}x$ decreases, resulting in a decrease in $\dot{m}_l$. In other words, increasing L leads to higher viscous resistance encountered by the liquid returning from the condenser to the evaporator. If the length of the thermosyphon is doubled, $\dot{Q}_{\max}$ is therefore halved. However, the impact of L changes as θ increases. For $\theta > 0°$, the term $(- \cos \theta \cdot \frac{\mathrm{d}h}{\mathrm{d}x} + \sin \theta)$ in (2.13) becomes relevant to the calculation of the heat transfer rate. Further, in case of large θ, the influence of the first term $(- \cos \theta \cdot \frac{\mathrm{d}h}{\mathrm{d}x})$ becomes less significant, while the second term $(\sin \theta)$ becomes more dominant, resulting in a lesser influence of $\mathrm{d}h/\mathrm{d}x$ and therefore of L.

Effect of vapor counter-flow on $\dot{Q}_{\max}$

Figure 2.7(b) illustrates, for fixed inclination angle, the variation of $\dot{Q}_{\max}$ with H and therefore with the severity of the vapor counter-flow. The results indicate that at larger thermosyphon heights (H), the curves overlap perfectly, suggesting that counter vapor flow has a negligible impact on $\dot{Q}_{\max}$. This is attributed to the very small interfacial shear stress due to the magnitude of H. Not surprisingly, the influence of the vapor counter-flow becomes more prevalent as H decreases and the vapor velocity increases. Differences from the no vapor counter-flow case are especially apparent for relatively large $\bar{h}$ in which case $\dot{Q}_{\max}$ is comparatively large.

2.3   Heat pipe modelling

The section compares the capillary limit (relevant to heat pipes) to the hydrostatic limit (relevant to thermosyphons), shedding light on their differences and possible ramifications in terms of the design or the selection of one vs. the other heat transfer device. To this end, particular attention will be focused on details such as system requirements and operating conditions.

2.3.1   Neglecting vapor counter-flow

The radial and overall heat transfer through the heat pipe, based on a thermal network analysis is identical to (2.2). Here, R represents the overall thermal resistance across the heat pipe, which can be defined as

$$R = \frac{\delta}{K_s L_e} + \frac{\delta}{K_s L_e} + \frac{h}{K_e L_c} + \frac{h}{K_e L_e} \tag{2.26}$$

Here, h represents the wick thickness and K_e represents the effective thermal conductivity of the wick saturated with liquid refrigerant. This latter quantity can be defined as

$$K_e = \frac{K_f[(K_f + K_w) - (1 - \epsilon')(K_f - K_w)]}{[(K_f + K_w) + (1 - \epsilon')(K_f - K_w)]}$$

where we have assumed that the wick is exactly saturated with liquid. In this last equation, ϵ' denotes the wick porosity and can be expressed as follows

$$\epsilon' = 1 - \frac{\pi D^2}{4N^2}$$

Here, D represents the diameter of the mesh wires comprising the wick and N is the mesh number.

The pressure drop, ΔP_l, experienced by a fluid as it flows through a porous medium such as a wick can be obtained from Darcy's law. To wit,

$$\Delta P_l = \frac{\mu_l L \dot{m}_l}{\rho_l \kappa A_w} \tag{2.27}$$

Here, κ denotes the wick permeability, and A_w refers to the wick cross-sectional area, which represents the area of the wick (solid plus void space) that is perpendicular to the direction of the liquid flow. The variables κ and A_w can be defined as follows:

$$\kappa = \frac{D^2 \epsilon'^3}{122(1 - \epsilon')^2}, \qquad A_w = h\zeta$$

During the operation of the heat pipe, vapor flows from the evaporator to the condenser. The continuous deposition of water droplets in the condenser results in a liquid-vapor interface that is nearly flat [1]. As a result, the capillary radius becomes very large, and the pressure difference across the interface in the condenser section approaches zero. Therefore, only the capillary pressure difference of the liquid-vapor interface in the evaporator is responsible for liquid transport along the length of the wick. The pressure difference across the liquid-vapor interface can be calculated using Laplace's equation. Doing so, and applying (2.27) and $\dot{m}_l = \dot{Q}/h_{fg}$ yields

$$\Delta P_l = \Delta P_c = \frac{\sigma}{R_c} = \frac{\mu_l L \dot{Q}}{\rho_l \kappa A_w h_{fg}} \tag{2.28}$$

Here it is assumed that $\Delta P_v \ll \Delta P_l$. In this context, σ denotes the surface tension and R_e is the capillary radius as measured in the evaporator. The determination of R_c is critical in assessing the bounds of the solution space. Specifically, R_c must be greater than $R_{c,\min} = (W - D)/2$. Any solutions falling outside this range are unphysical. Thus the decision of whether to accept or reject a particular solution can be made by solving (2.28) for R_c with $\dot{Q}$ replaced by $\Delta T/R$ c.f. (2.2).

Complementing figure 2.3 (a), figure 2.8 illustrates, for the heat pipe case, the variation of $\dot{Q}$ with $\bar{h}$. Here $\bar{h}$ represents the average liquid depth, which is defined as the liquid layer depth after removing the wick (i.e., $\bar{h} = h\epsilon'$). Increasing the wick thickness decreases $\dot{Q}$; again, this is due to the presence of excess liquid, which increases the wick thermal resistance in the condenser section. Also consistent with our previous analysis, $\dot{Q}$ increases with ΔT as indicated by the upward shift of the
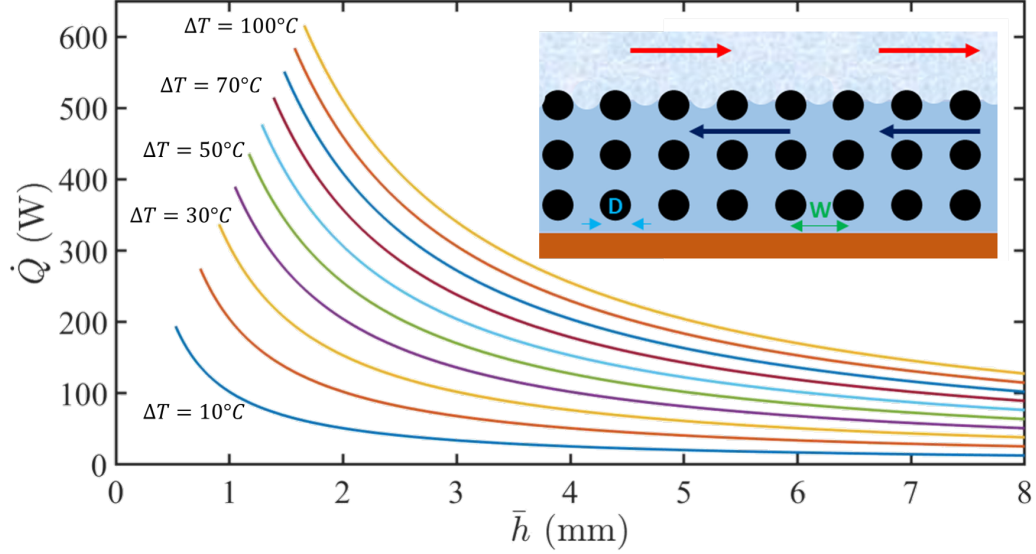
Figure 2.8: Variation of $\dot{Q}$ with $\bar{h}$ for different ΔT at $W/D =1.5$ and $\theta=0.2°$.

curves in figure 2.8. Furthermore, as ΔT increases, the curves also shift to the right. As before, the increase in radial heat flux needs to be balanced by the axial return of liquid from the condenser to the evaporator. The axial flow in question requires a minimum liquid volume. Therefore, and as ΔT increases, it is necessary to increase the minimum value of $\bar{h}$.

Figure 2.9 illustrates the variation of $\dot{Q}$ with $\bar{h}$ for fixed ΔT but different W/D. Larger W/D values correspond to larger wick porosities, ϵ'. There are three key observations that can be drawn from this figure 2.9. Firstly, similar to the previous case, for a given wick porosity, an increase in wick thickness leads to a decrease in $\dot{Q}$. The figure 2.9 (a) also shows that a higher heat transfer rate is realized by decreasing W/D. There are two reasons for this: (i) less porous wicks contain more solid material compared to void space and therefore enjoy larger K_e, and, (ii) screen-type wicks with closely-spaced wires can achieve smaller radii of curvature and therefore a greater driving force for capillary-induced flow. Thirdly, the starting points of the curves shift to the right as W/D is decreased. This shift follows from the fact that, by decreasing W/D, we simultaneously increase the axial flow resistance. Such a
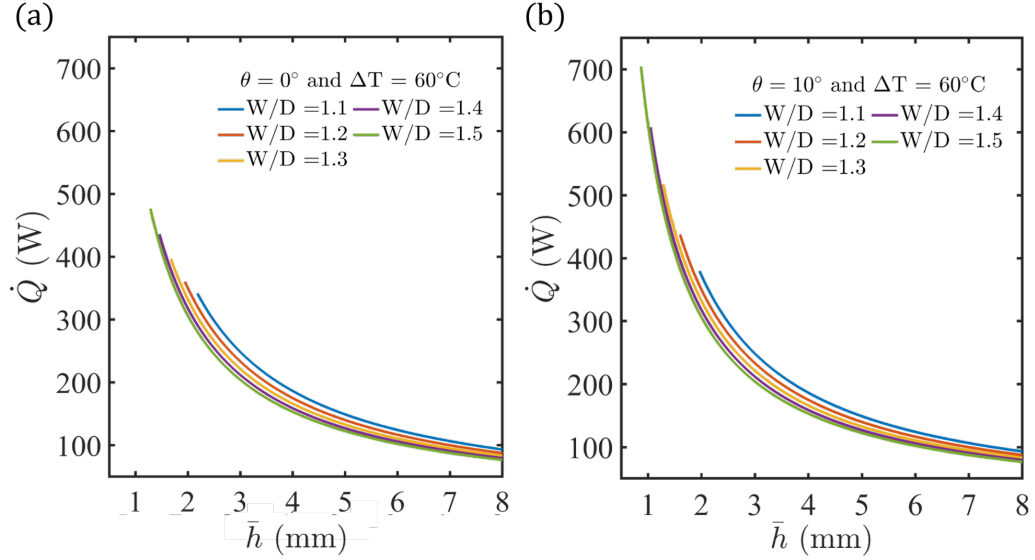
Figure 2.9: Variation of $\dot{Q}$ with $\bar{h}$ for different W/D and $\Delta T = 60°C$ (a) at $\theta = 0°$ and (b) $\theta = 10°$.

resistance requires a certain minimum fluid depth to overcome hence the increase in the minimum value of $\bar{h}$.

For small $\bar{h}$, the heat pipe functions effectively only when W/D is relatively large. This situation occurs when the liquid layer is thin, and the wick has high porosity and therefore a large permeability to facilitate the return flow of liquid (by capillary pumping). Note that although $\dot{Q}$ can become quite large in the thin wick limit, operating a heat pipe within this parameter range comes with inherent risks. Even a slight reduction in the liquid mass (due to slow leakage, for example) or a minor decrease in the W/D ratio (resulting from a manufacturing defect) can easily lead to heat pipe dry-out.

When the heat pipe is titled through an angle θ, the factor ΔP_l must be replaced by $\Delta P_l = \Delta P_c + \rho g L \sin \theta$. Thus do we find that the overall heat transfer is enhanced when $\theta > 0°$ such that the evaporator lies below the condenser. Substituting $\Delta P_c =$

σ/R_c into this new expression for P_l, R_c can be written as

$$R_c = \frac{\sigma}{\Delta P_l - \rho g L \sin \theta} \tag{2.29}$$

The results depicted in figure 2.9 (b) demonstrate the correlation between Q and $\bar{h}$ when the heat pipe is inclined at an angle of $\theta = 10°$. In addition to the capillary pressure difference ($\sigma/R_c \approx 3000\,\text{Pa·s}$), the hydrostatic pressure ($\rho g L \sin 10° \approx 1730\,\text{Pa·s}$) plays a crucial role by exerting an additional driving force for liquid flow. Consequently, even with a comparatively thin wick, there is enough liquid to sustain a heat flux that could, in the horizontal inclination, only obtain with larger $\bar{h}$. Furthermore, the presence of a thin wick leads to smaller values of R, resulting in larger possible $\dot{Q}$ for a given temperature difference ΔT.

2.3.2 Consideration of vapor counter-flow

In the preceding subsection, we ignored the influence of vapor counter-flow. Now we include this effect and find that Darcy's law must be modified so as to include the effect of the shear stress applied along the liquid-vapor interface. To this end, we consider the Brinkman equation, which is derived from Darcy's law but includes a viscous shear dissipative term [83]. The simplified version of Brinkman's equation for the liquid phase reads as follows:

$$\frac{\mu_l}{\epsilon'}\frac{\partial^2 u_l}{\partial y^2} - \frac{\mu_l u_l}{\kappa} = \frac{\partial P_l}{\partial x} - \rho g_x \qquad \Rightarrow \qquad \frac{1}{\epsilon'}\frac{\partial^2 u_l}{\partial y^2} - \frac{u_l}{\kappa} = \Pi_l = \frac{1}{\mu_l}\left(\frac{\partial P_l}{\partial x} - \rho_l g_x\right) \tag{2.30}$$

The equation for vapor counter-flow remains unchanged from the thermosyphon case of (2.18) and (2.19) from subsection 2.2.4. Since Π_l and Π_v are solely functions of x. Solving (2.30) and (2.18) results in the following general expressions for u_l and u_v:

$$u_v = \Pi_v \frac{y^2}{2} + D_1 y + D_2$$

$$u_l = B_1 \exp\left(\sqrt{\frac{\epsilon'}{\kappa}}y\right) + B_2 \exp\left(-\sqrt{\frac{\epsilon'}{\kappa}}y\right) - \Pi_l \kappa$$

Here, B_1, B_2, D_1, and D_2 are constants because, modulo an inconsequential change of liquid depth in x, the liquid and vapor flow profile remain unchanged along the length of the heat pipe. The constants in question will be functions of Π_v and Π_l and can be determined by applying the following four boundary conditions: (i) $u_v(y = H) = 0$, (ii) $u_l(y = 0) = 0$, (iii) $u_l(y = h) = u_v(y = h)$, and (iv)

$$\frac{\partial u_l}{\partial y} - \epsilon' \frac{\partial u_v}{\partial y} - \frac{a\epsilon'}{\sqrt{\kappa}} u_l = 0$$

This latter equation between the porous medium liquid flow and the free medium vapor flow specifies an Ochoa-Tapia and Whitaker (1995)-type boundary condition that describes the shear stress exerted by the flowing vapor [84]. Here, a is a non-dimensional, $\mathcal{O}(1)$ coefficient that characterizes the excess stress along $y = h$. For convenience, we set $a = 1$ in the discussion to follow.

By applying the expressions for u_v and u_l, the mass flow rates $\dot{m}_l$ and $\dot{m}_v$ can be calculated as follows:

$$\dot{m}_l = \zeta\rho_l \int_0^h u_l dy$$

$$\dot{m}_l = \zeta\rho_l \left[B_1 \sqrt{\frac{\kappa}{\epsilon'}} \left(\exp\left(\sqrt{\frac{\epsilon'}{\kappa}} h \right) - 1 \right) - B_2 \sqrt{\frac{\kappa}{\epsilon'}} \left(\exp\left(-\sqrt{\frac{\epsilon'}{\kappa}} h \right) - 1 \right) - \Pi_l \kappa h \right]$$

$$(2.31)$$

$$\dot{m}_v = \zeta\rho_v \int_h^H u_v dy = \zeta\rho_v \left[\frac{\Pi_v}{6} \left(H^3 - h^3 \right) + \frac{D_1}{2} (H^2 - h^2) + D_2(H - h) \right] \quad (2.32)$$

The expressions obtained for B_1, B_2, D_1, and D_2 using the four boundary conditions can be inserted into equations (2.31) and (2.32). Making these substitutions, the values of Π_l and Π_v can be determined by recognizing that $\dot{m}_l = -\dot{m}_v = (\dot{Q}/h_{fg})$ where, as usual, the rate of heat transfer is determined from $\dot{Q} = \Delta T/R$.
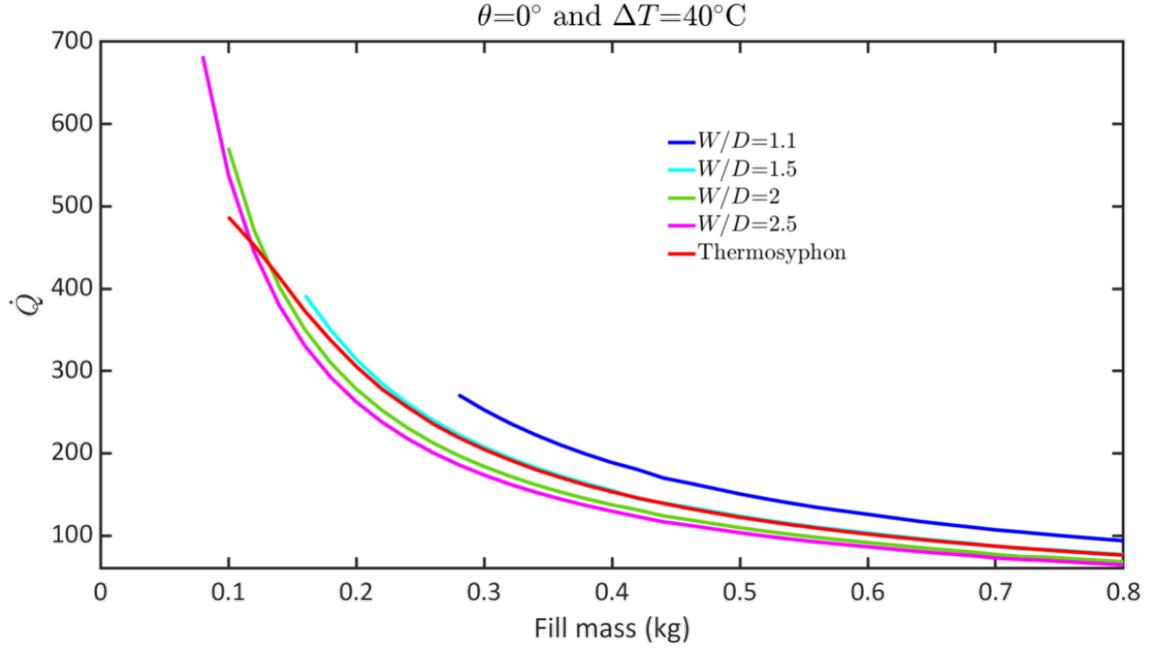
Figure 2.10: Performance comparison between thermosyphon and heat pipe at $\theta = 0°$.

The values of Π_l and Π_v are obtained using (2.31) and (2.32), respectively. Subsequently, α and R_c are evaluated by rearranging $\Pi_v = \frac{\alpha}{\mu_v}$ and $\Pi_l = \frac{1}{\mu_l}\left(\frac{\sigma}{R_c L} - \rho_l g \sin\theta\right)$, respectively. In the latter case, the expression for R_c is found to read

$$R_c = \frac{\sigma}{L(\Pi_l \mu_l + \rho_l g \sin\theta)} \tag{2.33}$$

As in subsection 2.3.1, the determination of R_c is important in evaluating the physical acceptability of our solution.

The inclusion of counter vapor flow in our study yielded results that closely match with the findings in subsection 2.3.1. This outcome can be attributed to the presence of a wick within the heat pipe, which decreases the area of the liquid-vapor interface. Consequently, this reduction in interfacial area results in a decrease in shear stress at the interface.
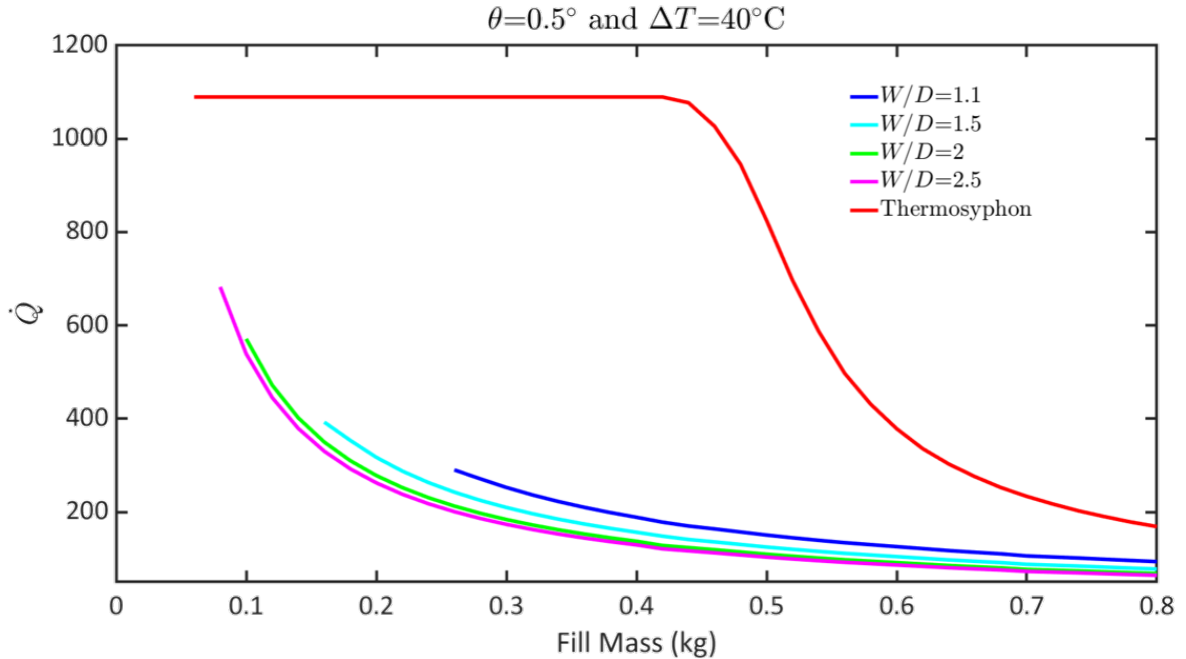
Figure 2.11: Performance comparison between thermosyphon and heat pipe at $\theta = 0.5°$.

2.4 Performance comparison: heat pipe vs. thermosyphon

In the previous sections, we examined how different geometric parameters influence the rate of heat transfer in a thermosyphon and in a heat pipe. Another crucial aspect, although not given as much emphasis, is to directly compare the performance of these two heat transfer devices. The performance comparison in question is illustrated by figure 2.10, specifically for the case where $\theta = 0°$. For sufficiently small liquid charges (i.e. fill mass ¡ 0.09 kg), the capillary pressure difference in case of the heat pipe and the hydrostatic pressure difference in case of the heat pipe is not strong enough to replenish the liquid that is evaporated in the evaporator. Thus a state of dryout exists. Of greater interest is the region where the fill mass exceeds $0.09\,\mathrm{kg}$ for which a direct comparison can be made between the rate of heat transfer associated with the thermosyphon (red curve) as compared to a heat pipe (other curves, demarcated by W/D).

As the fill mass increases within the range of 0.1 kg to 0.15 kg, a crossover point occurs between the thermosyphon and a heat pipe having $W/D = 2$ or $W/D = 2.5$. At this crossover point, both devices exhibit equal $\dot{Q}$. By contrast, figure 2.10 shows that the red and blue curves (corresponding, respectively, to the thermosyphon and to a heat pipe with $W/D = 1.1$) never intersect: owing to the low wick porosity associated with such a small value of W/D, the blue curve applies only for a fill mass of more than approximately 0.28. Over this range, capillary pumping proves the more effective mechanism of liquid return and radial heat conduction is aided by the comparatively large solid fraction within the wick. For these reasons, the blue curve remains above the red curve. More interesting, therefore, is the comparison between the thermosyphon and a heat pipe having $W/D = 1.5$ (teal curve). Here, we find that the rate of heat transfer is nearly identical (though, granted, the heat pipe experiences dryout at a larger fill mass than does the thermosyphon).

Figure 2.11 performs a similar comparison to figure 2.10 but now for the case $\theta = 0.5°$. In the inclined scenario, both the heat pipe and thermosyphon benefit from gravity, which helps to drive the return flow of liquid to the condenser. However, in the case of the heat pipe, the gravity-driven flow faces additional viscous resistance as it flows through the porous medium comprising the wick. Of course, no such restriction applies for the thermosyphon for which the wick is absent and the liquid presents as a freely flowing thin film. In turn, the depth of this film is not limited by the wick height as it is in the case of the heat pipe. For this reason, and given the long lengths of heat pipes and thermosyphons considered here, we note from figure 2.11 that the red curve lies significantly above the counterpart curves corresponding to heat pipes having different W/D. If the length of the heat pipe and thermosyphon were to be reduced, the benefit derived from inclining the thermosyhon would be less and the gap between the red curve and the other curves of figure 2.11 would close.

2.5 Hydrostatic limit as a replacement of the capillary limit

This section aims to explain the limits associated with hydrostatic-driven flow and with capillary-driven flow. More specifically, we ask about the implications of replacing the capillary limit (applicable to heat pipes) with the hydrostatic limit (applicable to thermosyphons).

Similar to the colored curves of figure 2.3 (b), the hydrostatic limit is defined from the maximum heat flux that a thermosyphon can realize for a given geometry and fill fraction. The variation of the hydrostatic limit with the operating temperature can be derived by replacing the factor of ΔT that appears in (2.2) with a corresponding expression involving T_{op}. More precisely, we note that

$$T_{\mathrm{op}} = \frac{T_e + T_c}{2} = \frac{\Delta T}{2} + T_c = \frac{\dot{Q}R}{2} + T_c \qquad (2.34)$$

Equation (2.34) must be interpreted with care because it seems to suggest a linear correlation between $\dot{Q}$ and T_{op}. In reality, however, R also changes with T_{op} suggesting a nonlinear relationship between the variables in question. This nonlinearity applies both when considering the hydrostatic as well as the capillary limit. With (2.34) to hand, we turn to figure 2.12 for which $\theta = 0°$ and the thermosyphon design remains the same always. while T_{op} varies with ΔT as prescribed by the following formula: In figure 2.12 (a), an increase in $\dot{Q}$ is associated with an increase in T_{op}. It can be observed that increasing $\bar{h}$ results in a decrease in $\dot{Q}$ due to the higher radial thermal resistance. Another crucial aspect to consider is that, for small $\bar{h}$ values, the thermosyphon operates up to a limited T_{op}. This limitation arises because decreasing $\bar{h}$ simultaneously decreases h_e, whose minimum possible value (e.g., 0.5 mm) is approached as T_{op} is increased. Consequently, for a fixed $\bar{h}$, there exists a critical threshold beyond which $\dot{Q}$ cannot be further increased, leading to thermosyphon failure.
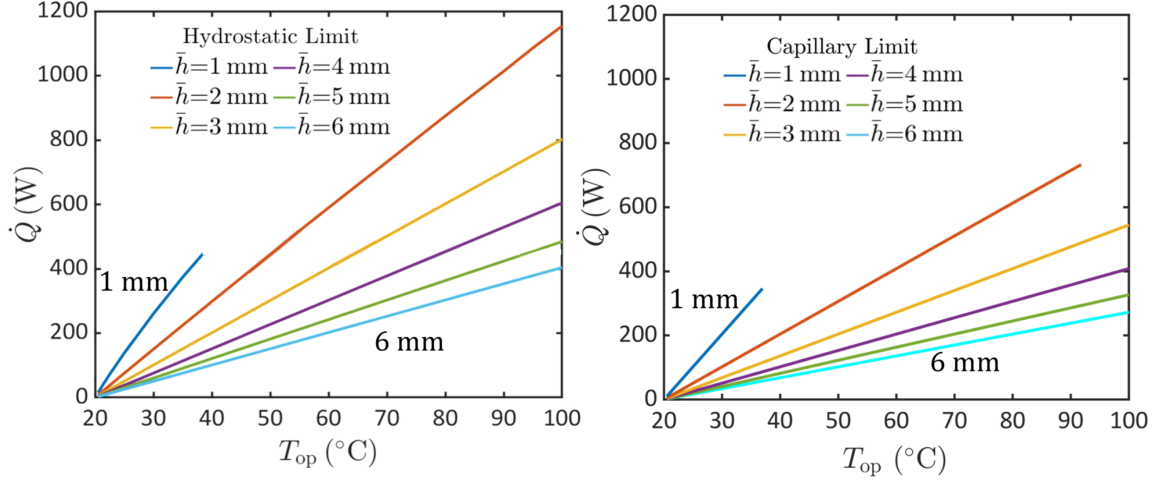
Figure 2.12: Hydrostatic limit vs. capillary limit at θ of 0° for different $\bar{h}$. (a) Hydrostatic limit (b) Capillary limit.

The capillary limit for a heat pipe is determined using a similar analysis as the hydrostatic limit. Here, however, the maximum flow rate is associated, in the evaporator, with a minimum radius of curvature rather than with a minimum elevation or liquid pool depth. In figure 2.12 (b), the variation of $\dot{Q}$ with T_{op} is presented for different fill ratios ($\bar{h}$) of a heat pipe with a fixed W/D ratio of 1.5. The curves in the plot represent the capillary limit, demonstrating that as T_{op} increases, $\dot{Q}$ also increases for different $\bar{h}$. However, it is noteworthy that increasing $\bar{h}$ results in a reduction of $\dot{Q}$ due to the increased radial thermal resistance of the wick structure.

Considering both panels of figure 2.12 simultaneously, several qualitative similarities can be observed. First, there is an increase in $\dot{Q}$ as T_{op} increases, and a decrease in $\dot{Q}$ as $\bar{h}$ increases. However, despite these similarities, an important distinction exists between figure 2.12 (a) and figure 2.12 (b). Notably, the hydrostatic limit operates at larger values of $\dot{Q}$ and extends to higher T_{op} compared to the capillary limit for all $\bar{h}$ values considered. Unfortunately, this last observation is not universal and instead depends on the properties of the wick, here quantified by W/D. Thus if W/D is

increased to 1.5 (not shown), there exists a region of the parameter space (consisting of large $\bar{h}$) for which the limit associated with the hydrostatic limit is more grave than that associated with the capillary limit. In summary, therefore, the question of whether a heat pipe or thermosyphon will offer superior performance is nuanced and cannot be answered definitively without consideration of W/D, T_{op} range, and $\bar{h}$.

2.6 Conclusion

In the context of thermosyphon design, there exists a balance between the operational heat transfer rate ($\dot{Q}_{\mathrm{op}}$) and the hydrodynamic heat transfer rate ($\dot{Q}_{\mathrm{hydro}}$), which is represented by the maximum heat transfer rate, $\dot{Q}_{\mathrm{max}}$. This equilibrium point is crucial in optimizing the performance of thermosyphons. Deviation from the optimal filling level in the thermosyphon, whether due to overfilling or underfilling, can result in dry-out or performance deterioration, respectively. However, relying solely on operating at $\dot{Q}_{\mathrm{max}}$ can be a risky strategy, as any leakage of the working fluid can lead to dry-out. Inclining the thermosyphons enhances performance by increasing the heat transfer rate ($\dot{Q}$) for a given $\bar{h}$. For a fixed thermosyphon design, inclining the thermosyphon provides a range of $\bar{h}$, where $\dot{Q}_{\mathrm{max}}$ is achieved. The variation $\dot{Q}_{\mathrm{max}}$ or $\dot{Q}$ is also influenced by vapor counter-flow. At extremely high rates of heat transfer, the impact of vapor counter-flow becomes significant and needs to be taken into consideration. Hence, modeling the effect of vapor counter-flow becomes crucial in determining the optimal performance of thermosyphons.

When the W/D ratio is fixed in a heat pipe, the heat transfer rate ($\dot{Q}$) decreases as the wick thickness or the average liquid depth ($\bar{h}$) increases due to an increase in radial thermal resistance. In general, a smaller W/D ratio leads to a higher $\dot{Q}$ because of a lower radial thermal resistance. However, a larger W/D ratio results in a higher $\dot{Q}_{\mathrm{max}}$. This phenomenon occurs because a thin wick with a higher W/D ratio can accommodate more liquid, leading to enhanced capillary-driven flow. Consequently,

this enables a higher maximum heat transfer rate ($\dot{Q}_{\text{max}}$) to be achieved.

In comparison, thermosyphons tend to perform better compare to heat pipe for large $\bar{h}$ and large W/D. Conversely, heat pipes perform better for small $\bar{h}$ values and large W/D. The work of section 2.4 is mainly beneficial when choosing a heat pipe or thermosyphon for heat transfer. In addition to aiding in qualitative selection decisions, it also offers a quantitative guidance that assists in best performing solution.

In thermosyphons, a performance limit is defined as the hydrostatic limit. This limit can be utilized in thermosyphons to replace the capillary limit on the "fundamental diagram" of heat pipes. Similar to the capillary limit in the heat pipe limiting curve, a defined hydrostatic limit can also be incorporated into the fundamental diagram of thermosyphons. This comprehensive approach allows for a better understanding of the heat transfer characteristics and limitations of thermosyphons.

Chapter 3

Experimental study on R1234yf/R134a mixture (R513a) as R134a replacement in heat pipes

3.1 Introduction

Numerous industries are culpable for greenhouse gas emissions, including the refrigeration and air conditioning sector, which poses a considerable threat due to its generation of copious amounts of harmful refrigerant gas [85]. The Heating, ventilation, and air conditioning (HVAC) industry, which heavily depends on refrigerants, is expanding at a rapid pace and is a major perpetrator of global warming. Once these refrigerants, in particular hydrofluorocarbons (HFCs), escape into the atmosphere, they become significant contributors to climate change [65–67, 86]. In 2015, HFCs only accounted for around 2% of greenhouse gas emissions, but their contribution is expected to rise to $9 - 20\%$ by 2050 [Canada gazette (2015)][68]. Owing to their substantial impact on climate change relative to carbon dioxide, HFCs have been categorized as greenhouse gases under the Kyoto Protocol (UN, 1997) [87, 88]. Over the past decade, several countries have established plans and protocols to decrease the use of HFCs in heating, ventilation, and air conditioning (HVAC) systems, such as the Montreal Protocol [89]. These initiatives to mitigate the detrimental impacts of climate change have resulted in elevated costs for HFC refrigerants. In response,

researchers are examining the thermodynamic properties of low global warming potential (GWP) refrigerants, which offer a more environmentally and economically sustainable alternative [90–92]. Therefore, the HVAC industry is persistently striving to reduce carbon and HFC emissions. In the immediate future, the sector's focus will shift towards replacing HFCs with low-GWP refrigerants to minimize their impact on the environment. It will be imperative to evaluate the suitability of alternative fluids in existing systems and to determine whether performance analysis of refrigerant systems could enhance performance.

R513a's refrigerant touts a Global Warming Potential (GWP) of 573, a remarkable decrease of 60% compared to its predecessor R134a (refer table 3.1). Such an achievement elevates R513a to a potential candidate to supplant R134a as a suitable alternative. Although the refrigerant's boiling point and thermal heat capacity are on par with that of R134a, R513a's other properties, namely vapor pressure, surface tension, density, and thermal conductivity, may exhibit substantial variation. Given such modifications, it is of utmost importance to meticulously consider their impact prior to transitioning to this new refrigerant.

Essentially, the implementation of R513a requires modifications to the system design in order to ensure consistent performance. R513a is versatile, applicable to a plethora of heat transfer applications, water coolers, air conditioners, heat pumps, and ice arenas. This eco-friendly and energy-efficient refrigerant is increasingly embraced by industries, especially heat pump manufacturers. Research has explored the transition from R134a to R513a in various HVAC applications, including heat pumps, refrigerators, and other systems. Although R513a's altered properties may impact performance, such drawbacks can be alleviated by modifying the internal design. Despite the numerous studies on transitioning from R134a to R513a, there is a paucity of research on transitioning from R513a to R134a in heat pipe applications.

The heat pipe sector represents a lucrative market valued at \$1 billion and is projected to sustain a Compound Annual Growth Rate (CAGR) of 6.17%, according to a recent report by Technavio (September 2021)[69]. Nevertheless, a dearth of research on the transition of heat pipes to R513a has left most companies reliant on traditional refrigerants. Unfortunately, there are few, if any, efficacious approaches for converting to R513a at present.

The paradigm shift towards eco-friendly refrigerants such as R513a, away from the harmful R134a, has noteworthy implications for the engineering design of heat pipes. There exist various elements that have an impact on heat pipe performance, including the heat pipe's design (e.g., length, internal diamateter (ID), outer diameter (OD), evaporator and condenser lengths, and adiabatic length), operational parameters ($\dot{Q}$), refrigerant types, among others. However, when considering only the interchange of refrigerants, these factors can remain constant throughout the experiments. On the other hand, the variation in fill ratio or the mass of working fluid injected into the interior of the heat pipe is arguably the most crucial parameter in determining heat pipe performance. If the mass is inadequate, the evaporator may experience "local dry-out", in which dry regions of the evaporator are prone to overheating. Conversely, if the fill mass (M) increases too much, the depth of the liquid pool that gathers in the evaporator may become too deep, leading to additional thermal resistance at the evaporator end of the heat pipe. Predicting the optimal value of M is a challenging task due to the complex nature of both factors: the effect on the liquid pool and local dry-out. Additionally, one factor has a negative influence while the other has a positive influence.

Our study demonstrates that merely substituting R513a for R134a in a heat pipe can result in considerable disparities in performance. By analyzing these discrepancies concerning heat input and refrigerant mass added to the heat pipe, we gain valuable

insights into the critical factors that influence overall heat pipe performance. Our investigation presents substantial evidence that compares the performance of both refrigerants for smooth (thermosyphon) and grooved heat pipes. We conducted experiments with both types of heat pipes using R513a and R134a refrigerants, allowing us to compare refrigerant performance based on the fill mass and angle of inclination (θ). Our findings offer guidance for transitions from R134a to R513a and indicate when design modifications may be necessary. Moreover, they provide an understanding of how to adjust design parameters to achieve similar levels of performance.

3.2   Experimental Details

3.2.1   Heat pipe specifications

In our experiments, we employ a total of 20 heat pipes, which are pre-filled with refrigerants. These heat pipes are crafted from high-quality copper (type K, Engineered Air), sealed at both ends, and equipped with a Schrader valve (CD4460B, C&D valve) positioned at the middle point. A vacuum pressure of $92\pm2\,\mu$m of mercury is created in the heat pipe to remove the air before sealing the ends. The valve is used to introduce different fill mass (M) of refrigerants. These heat pipes are equipped with two different options for the inner surface, which are then paired with two different refrigerants and five distinct fill masses (M). Accurately determining the actual fill ratio of liquid present in the heat pipe necessitated careful consideration of the heat pipe dimensions. The dimensions of the heat pipes are as follows: a length of $1.2\pm0.02\,$m and inner and outer diameters of $14.5\pm2\,$mm and $16.5\pm2\,$mm, respectively. Throughout the experiments, the length of the evaporator is set to $0.45\pm0.01\,$m, the condenser is set to $0.45\pm0.01\,$m, and the adiabatic section is set to $0.3\pm0.01\,$m. The grooved internal surface of the heat pipe is engineered to feature a highly intricate, triangular-shaped helical groove with an height of $400\pm10\,\mu$m and a base width of $200\pm5\,\mu$m, with a helix pitch length equal to $400\pm8\,\mu$m. The variation in liquid height inside

the heat pipe at a given inclination angle is calculated by considering geometrical parameters and density data of both the liquid and vapor states.

3.2.2   Experimetal setup

The experimental setup for the heat pipe system consists of an evaporator, adiabatic, and condenser sections, as shown in figure 3.1. Aluminium blocks were assembled to create a cylindrical space, which is suitable for housing the heat pipe. In figure 3.1, the evaporator section, representing the heat input end, is indicated by the red arrow, while the condenser section, representing the heat output end, is denoted by the blue arrow.

The evaporator section of the experimental setup consists of four aluminum blocks, each measuring 11.25 cm in length. These blocks are assembled in series, forming a cylindrical shape with a diameter equal to the outer diameter (OD) of the heat pipe. Each block in the evaporator section is equipped with four electric heating units (26008, Tutko), each having an electrical resistance of $2\,\Omega$. In total, the evaporator section contains 16 resistance heaters, with each heater's resistance arranged in parallel within an electric circuit. The heat input to the evaporator section is controlled by adjusting the voltage supplied to the electric circuit. To regulate the voltage supplied to the cartridge heaters, we utilized a DC Power Supply (1687B, B&K Precision) as part of the setup.

The adiabatic portion is just the exterior of the heat pipe positioned between the evaporator and condenser sections.

The design of the condenser section is similar to that of the evaporator section, but it incorporates cooling channels to maintain fix temperature at the condenser end. The condenser section of the heat pipe setup consists of cooling blocks, each with a
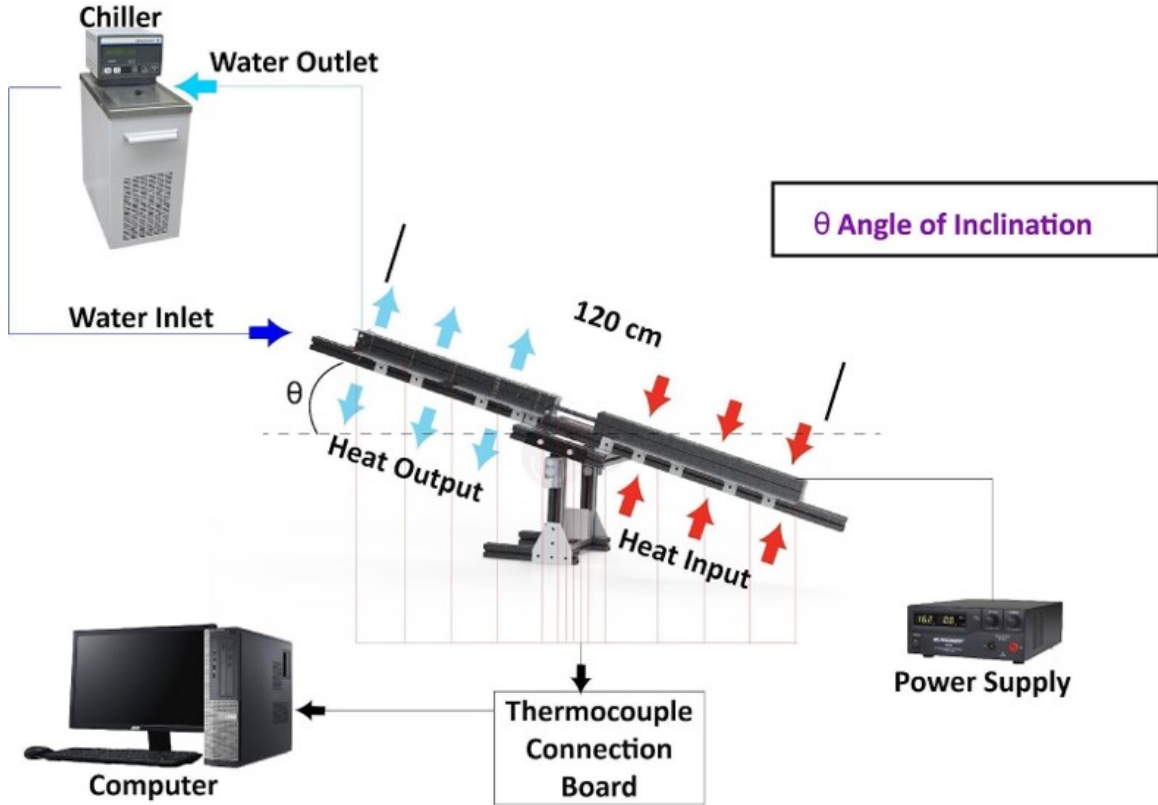
Figure 3.1: Schematic of the heat pipe experimental setup. Red arrow: evaporator section and Blue arrow: condensor section.

length of 45 cm, which share a design resembling the heating blocks and are assembled to form a cylindrical shape between them. The condenser block serves as a heat exchanger, and the blocks are connected with channels that facilitate the axial circulation of chilled ethylene glycol throughout the assembled blocks. Inlet and outlet ports are connected to a cooling unit (9106A11B, Polyscience) that pumps ethylene glycol at a controlled temperature of -10°C. This coolant enables us to achieve the necessary operating temperature.

Each condenser and evaporator is equipped with five T-type thermocouples (5SRTC-TT-T-20-36, OMEGA), which are spaced at 10 cm intervals. The precise axial position and coordinates of all these thermocouples are depicted in Figure 3.2. These thermocouples have a resolution of 0.1°C and an accuracy of ±1°C. The calibra-
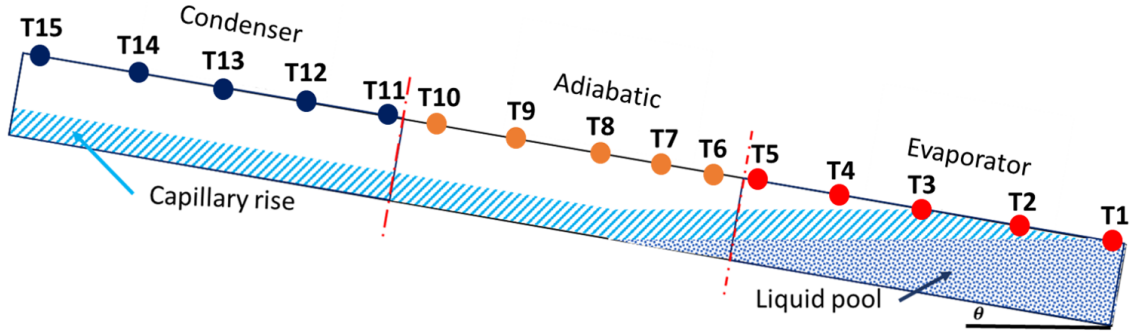
Figure 3.2: Schematic of heat pipe (image not to scale). Thermocouples' axial positions: T1 (2.5 cm), T2 (12.5 cm), T3 (22.5 cm), T4 (32.5 cm), T5 (42.5 cm), T6 (50 cm), T7 (55 cm), T8 (60 cm), T9 (65 cm), T10 (70 cm), T11 (77.5 cm), T12 (87.5 cm), T13 (97.5 cm), T14 (107.5 cm), and T15 (117.5 cm).

tion accuracy between 0°C to 100°C is ±0.8°C. To prevent electrical short circuits caused by direct contact between the heat pipe and thermocouples, we securely attach the thermocouples to the heat pipe using thermally conductive and electrically insulating tape (8810, 3M). Additionally, insulating tape is applied at the tip of each thermocouple to prevent electrical short circuits. The temperature data captured by the thermocouples is collected by a custom-made data acquisition (DAQ) system (Custom, Made in-house). The temperature data can be accessed through the serial monitor integrated into an Arduino IDE on a personal computer.

The temperature in the adiabatic section is measured using five K-type thermocouples (GK11M, Test Products Int), which are positioned at distances of 6 cm one from the other. The adiabatic temperature data is not utilized in the calculation; instead, we opted for a relatively imprecise and more cost-effective option. The position of all these thermocouples is depicted in figure 3.2. Additionally, a Fluke 54-2 B dual-input data logging thermocouple thermometer (52-2, FLUKE) is used to manually record temperature data from five K-type thermocouples. These thermocouples have a resolution of 0.1°C and an accuracy of ±2°C. The calibration accuracy between 0°C to 100°C is ±1.3°C.

Before commencing the experiments, all three sections, namely the evaporator, adiabatic, and condenser sections, were adequately insulated with glass fiber to minimize heat loss. The heat pipe assembly is mounted on a table with one degree of freedom, which allows for the inclination of the heat pipe through various angles (refer to figure 3.1). The table can be adjusted to any angle between -90° and 90°, providing flexibility in the orientation of the heat pipe for experimental purposes. This allows for studying the effect of inclination angle on the performance of the heat pipe.

Properties	R134a	R513a
Composition	Pure	44(R134a)/56(R1234yf)
Safety classification	A1	A1[93]
100-year GWP	1430	570[94]
T_b (°C)	-26.07	-28.3
$h_{fg}{}^a$ (kJ/kg)	198.6	171.27
$\rho_l{}^a$ (kg/m^3)	1294.8	1226.5
$\rho_v{}^a$ (kg/m^3)	14.4	16.1
$K_l{}^a$ (mW/m^3/°C)	92.0	79.9
$K_v{}^a$ (mW/m^3/°C)	11.5	11.7
$\mu_l{}^a$ (μPa-s)	0.18	0.28
$\mu_v{}^a$ (μPa - s)	10.7	10.5
$\sigma^{a'}$[95]	108	99

Table 3.1: Thermophysical properties of R513a and R134a [96]. The superscript 'a' indicates properties measured at 0°C

3.2.3 Refrigrents properties

The working fluids used in these experiments are R134a and R513a. R513a is a blend of 44% R134a and 56% R1234yf. Although the properties of R134a and R513a, as seen in Table 3.1, are comparable, R513a has no ozone-depleting potential and a 60% lower global warming potential, making it a greener option [94]. R513a can be used in

many R134a systems without design modification due to its several similar thermo-physical properties, and due to the fact that it is also non-toxic and non-flammable (ASHRAE safety classification) [97], making it suitable for heat pipe experiments. In summary, this choice of working fluids allows for environmentally friendly and safe experimentation while minimizing the need for system modifications.

3.2.4 Design of experiments

The experiments aimed to establish a temperature gradient along the heat pipe. To achieve varied heat inputs ranging from 10 to 70 W in increments of 10 W, the voltage (V) of the cartridge heater input variable was adjusted. After setting the input power, the system was allowed to reach an equilibrium state, defined as a temperature difference of less than 0.1°C between the evaporator and condenser, within 10 min. During this stage, temperature measurements were recorded for the evaporator, condenser, and adiabatic sections.

$$T_e = \frac{T_1 + T_2 + T_3 + T_4 + T_5}{5} \tag{3.1}$$

$$T_c = \frac{T_{11} + T_{12} + T_{13} + T_{14} + T_{15}}{5} \tag{3.2}$$

$$R = \frac{\Delta T}{Q} = \frac{T_e - T_c}{Q} \tag{3.3}$$

$$T_{op} = \frac{T_e + T_c}{2} \tag{3.4}$$

The average temperature of the evaporator (T_e) and condenser (T_c) is calculated by taking the arithmetic average of the measurements from five thermocouples in each respective section, as shown in (3.1) for the evaporator and (3.2) for the condenser. Moreover, the thermal resistance (R) and operating temperature (T_{op}) of the heat pipe are determined using (3.3) for thermal resistance and (3.4) for the operating

temperature.

The investigation progressed by gradually increasing the heat inputs, and reverse trials were conducted to ensure consistency of results. Each experiment was conducted twice, and the reported findings represent the average of those recordings. The deviation between the two experiments was found to be smaller than the instrumental error; therefore, the deviation of the experiments is not reported.

3.2.5 Investigating the effect of θ on heat pipe performance
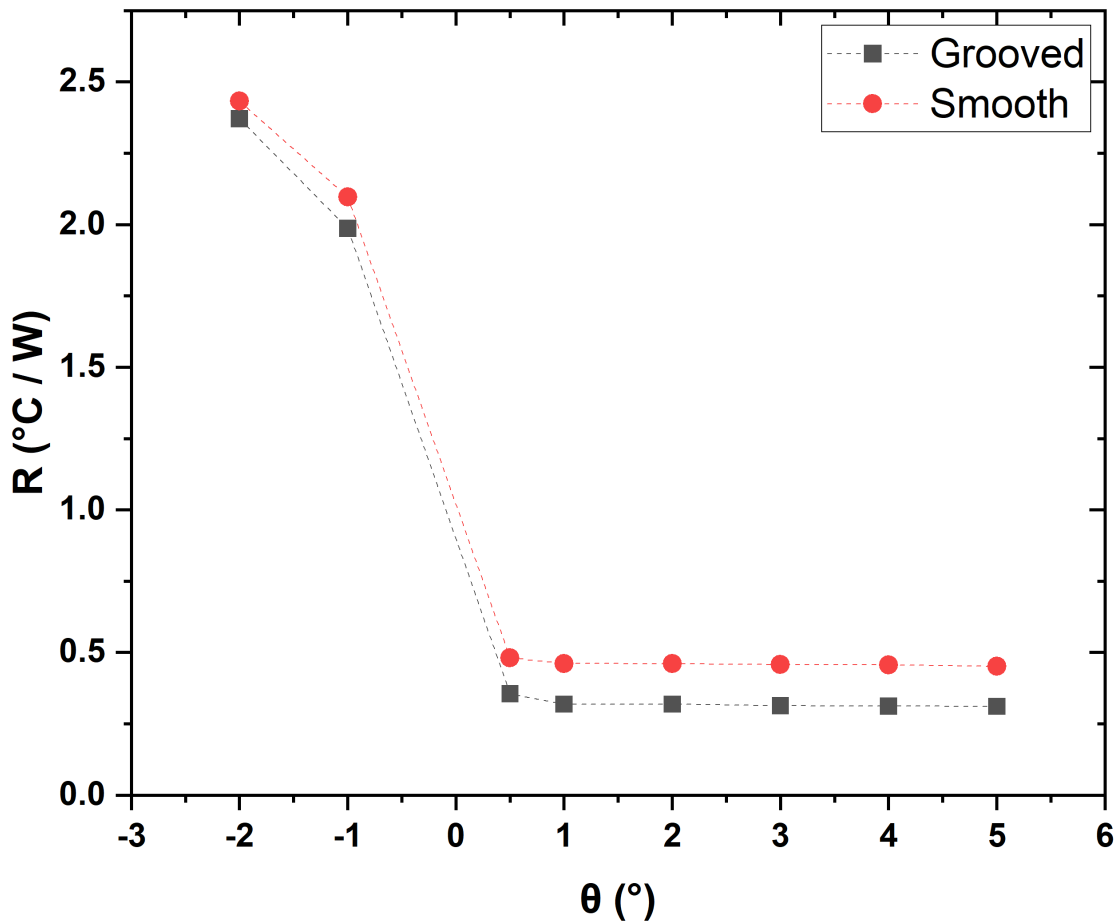
Figure 3.3: R variation with θ at $\dot{Q}$=30 W and M=40 g

This section delves into the performance evaluation of a grooved heat pipe and a smooth heat pipe with tilt angles (θ), aiming to establish a correlation between their

performance and θ. A positive θ denotes a downward inclination of the heat pipe, whereas a negative θ denotes an upward inclination – refer figure 3.2. During these specific experiments, both smooth and grooved heat pipes were subjected to power inputs of 20 W and 30 W, with corresponding masses (M) of 40 g and 60 g. The trend observed remained similar regardless of the heat transfer rate ($\dot{Q}$) and mass (M). Therefore, we chose to report the results only for an M of 40 g and a $\dot{Q}$ of 30 W. The corresponding thermal resistance (R) variation with inclination is presented in figure 3.3.

The results reveal that the thermal resistance (R) is initially high for negative θ values due to the opposing effect of gravity and insufficient capillary force. As θ increases, R decreases. Notably, R exhibits high sensitivity in the vicinity of θ near 0°. However, as θ surpasses 0.5°, the reduction in R becomes minimal, and eventually, R reaches a stagnant state. This behavior is attributed to the dominance of gravity in the return of flow at positive θ. The theoretical analysis in Chapter 2 confirms that increasing θ affects R primarily at small values, while it remains unchanged beyond a certain threshold. The stagnation of R is further supported by the absence of significant changes at θ of 30° (not reported). Previous studies have shown that grooved heat pipes, which utilize capillary forces to counteract gravity and supply sufficient liquid to the evaporator, can avoid the sharp transition in heat transfer near $\theta = 0°$ [98].

Based on these results, we concluded that conducting experiments at specific angles of inclination, such as θ=0.5° and 4.5°, allows for extrapolation of the findings to any angle greater than 0.5°.

3.3 Results and discussions

3.3.1 Experimental study of a helically grooved heat pipe at inclination $\theta = 4.5°$

R variation with $\dot{Q}$

Figures 3.4 and 3.5 demonstrate that for both R134a and R513a, R decreases with increasing $\dot{Q}$ regardless of M. The behavior of these refrigerants is influenced by several parameters, such as vapor density, vapor pressure, liquid viscosity, latent heat, and vapor viscosity. The most significant decline in R occurs in the 10 W to 20 W range for every M, beyond which the rate of decrease slows. In the case of R134a, and as $\dot{Q}$ increased from 10 W to 70 W at 20 g, the vapor pressure and density exhibited increases of 50-60% and 100%, respectively (refer appendix table B.8 and B.9). Meanwhile, the liquid viscosity decreased by 30% (see appendix B.7). Other thermophysical properties, such as the latent heat and liquid thermal conductivity and density, showed minor changes of less than 5%. The significant change of R exhibited in figure 3.4 is therefore believed to result from the sharp increase in vapor pressure and density and the sharp decrease in liquid viscosity, resulting in the observed trend that R decreases with increasing $\dot{Q}$. Similar variations apply for higher M.

The reason behind R decreases with $\dot{Q}$ is that at low heat flux (10 W), the working temperature remains small (-4.95° C), leading to a small difference in vapor pressure between the evaporator and the condenser. Consequently, the small pressure gradient, along with low vapor density, restricts vapor mass flow. Increasing power from 10 W to 20 W causes a more significant decrease in R than the increase from $\dot{Q}$=60 W to 70 W. At small $\dot{Q}$, when T_{op} is relatively small, any minor increase in $\dot{Q}$ leads, proportionally, to a large increase in vapor pressure. As $\dot{Q}$ increases, the vapor pressure also increases, but the proportional change is smaller than what is observed at smaller operating temperatures. Additionally, increasing $\dot{Q}$ from 10 W to 20 W re-

sults in a much larger increase in T_{op} than when $\dot{Q}$ is incremented from 60 W to 70 W.

The same trend between R and $\dot{Q}$ is observed for R513a, as shown in figure 3.5. Similar to R134a, the behavior of R513a is influenced by various parameters such as the vapor density, vapor pressure, and liquid viscosity. For a grooved heat pipe with R513a refrigerant and a mass of 20 g, increasing $\dot{Q}$ from 10 W to 70 W results in a 70% increase in vapor pressure and a 70% increase in vapor density, while the liquid viscosity decreases by 20% (refer appendix tables B.11, B.12, and B.10). Similar to R134a, the increase in power from 10 W to 20 W causes a more significant decrease in R than the increase from 60 W to 70 W due to the same reasons explained earlier.
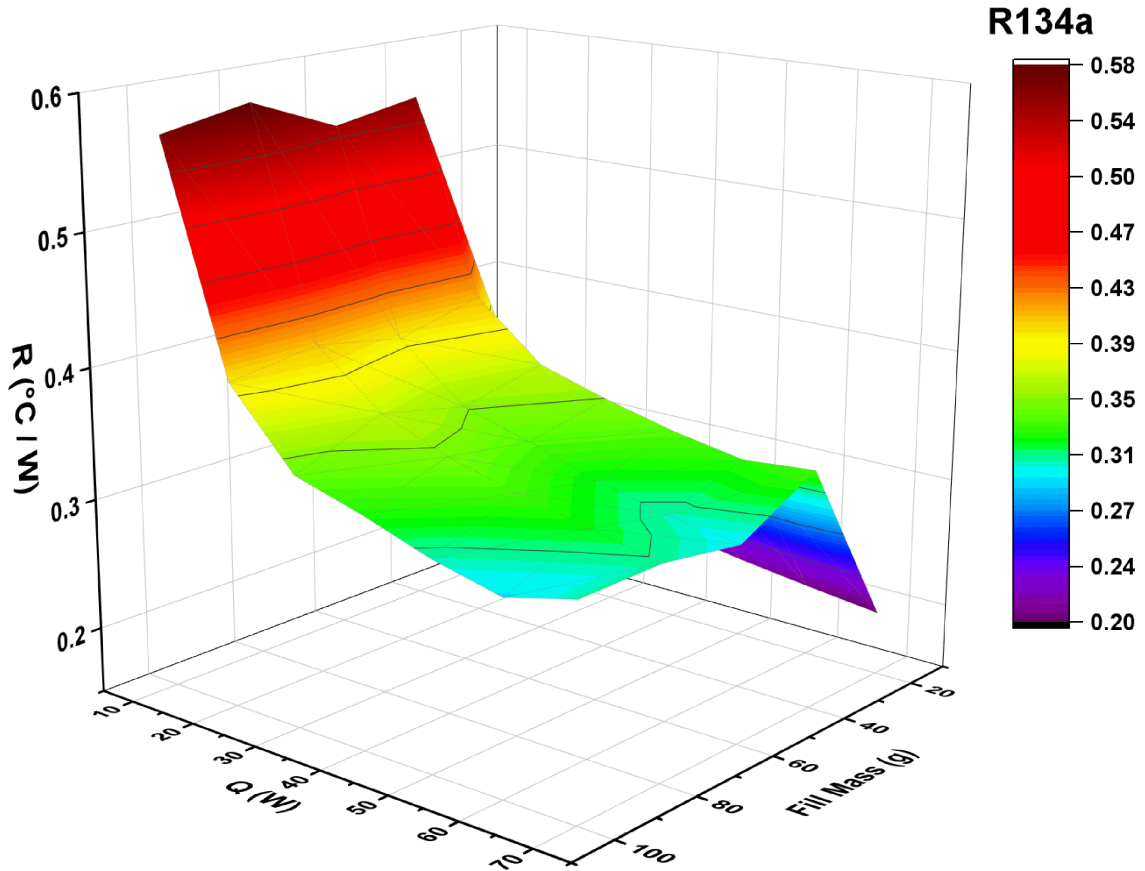
Figure 3.4: R variation of grooved heat pipe at θ=4.5° for R134a
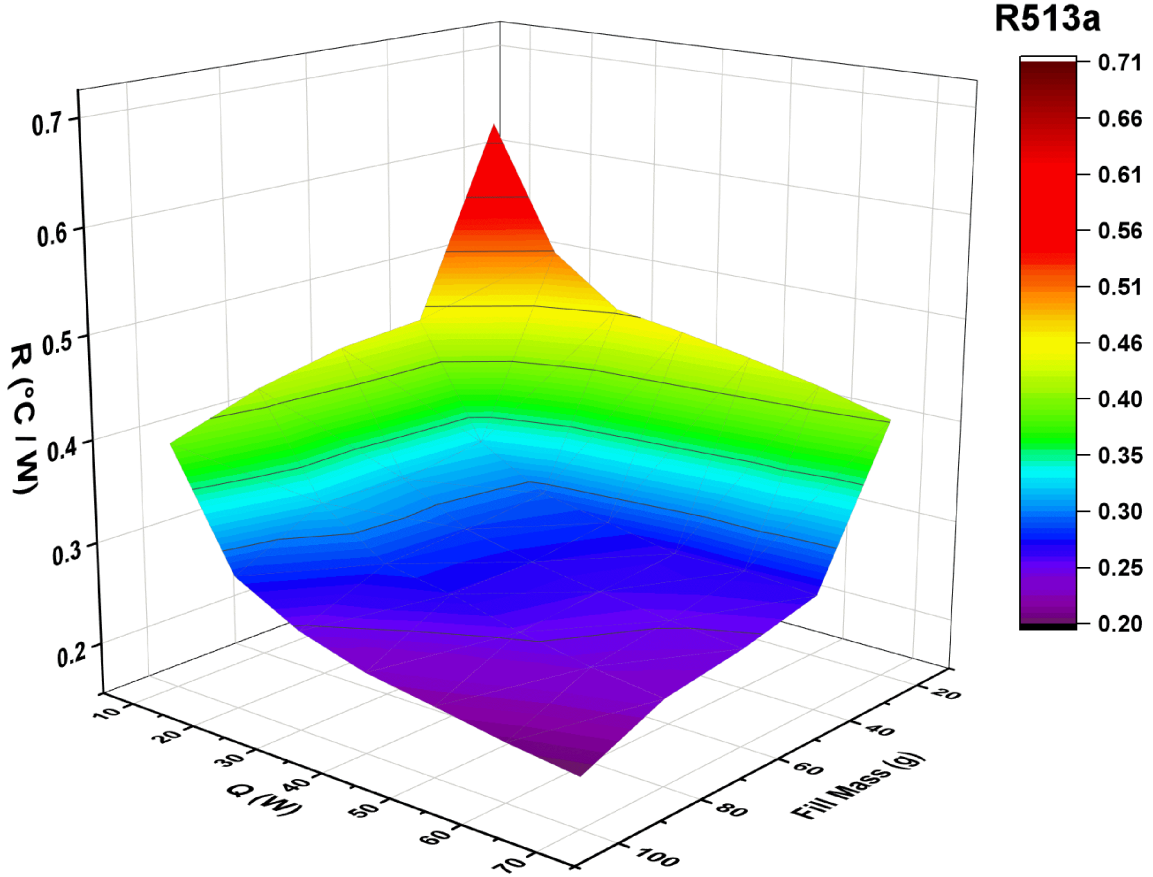
Figure 3.5: R variation of grooved heat pipe at θ=4.5° for R513a

R variation with M for R134a and R513a

The variation of heat pipe thermal resistance (R) with fill mass (M) exhibits a peculiar pattern, as illustrated for R134a in figure 3.4. The figure demonstrates that the minimum R, regardless of $\dot{Q}$, is observed when $M = 20\,\mathrm{g}$ after which it increases to a higher R-value before plateauing or showing only a marginal increase at higher M (i.e., $40\,\mathrm{g}$, $60\,\mathrm{g}$, $80\,\mathrm{g}$ and $100\,\mathrm{g}$). This anomalous behavior can be attributed to the grooved structure of the heat pipe's interior surface and to the properties of the refrigerant. In the case of grooved heat pipes, the helical grooves facilitate the uniform spreading of the refrigerant on the interior surface. The efficacy of this spreading process depends on the dimensions of the groove and the thermophysical properties of the refrigerant, such as surface tension and density. If the properties
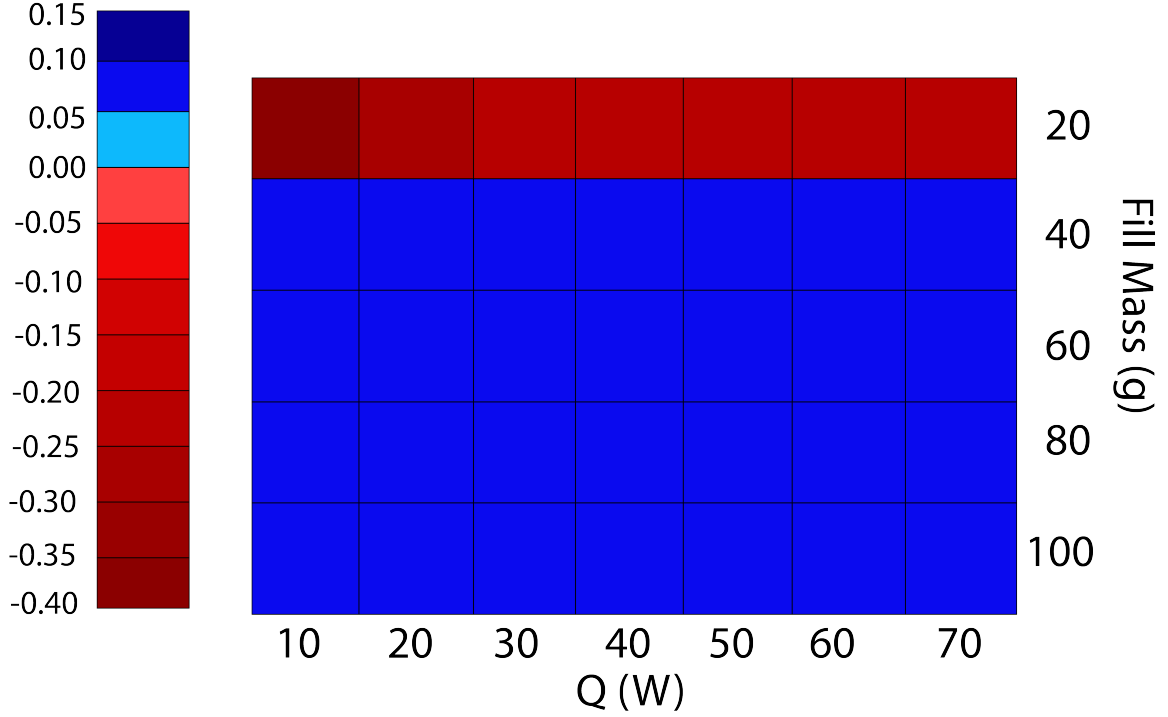
Figure 3.6: ΔR variation for grooved heat pipe at $\theta = 4.5°$

allow for uniform liquid spreading, the liquid will be distributed throughout the entire surface of the heat pipe, instead of forming a stagnant liquid pool. The effectiveness of the refrigerant distribution and its uniformity can be estimated with reference to the capillary rise, which provides indirect information about the circumferential spread of the liquid. The capillary rise expression is given as

$$h_{\mathrm{rise}} = \frac{2\sigma \cos \theta_c}{r \rho g} \tag{3.5}$$

where r is the groove spacing, ρ is the liquid density, σ is the surface tension, and $\cos \theta_c$ is assumed to be equal to 1 due to the small contact angle, θ_c, for both refrigerants. Based on surface tension data and groove parameters, it can be calculated that the liquid rise height in the groove is greater than $11\,\mathrm{mm}$, which is very close to the internal diameter of the heat pipe (ID $\approx 12\,\mathrm{mm}$). Consequently, local dry-out can be largely avoided. This fact is experimentally corroborated by the minor decrease in temperature observed in the evaporator section (from the 1st to the 5th thermocouple)

irrespective of $\dot{Q}$ and M [refer to B.1].

Thus, the plot in figure 3.4 shows that the lowest thermal resistance is observed when at an M of 20 g, regardless of $\dot{Q}$. Furthermore, our calculations indicate that an M of 25 g (at T_{op}=0°C) is required to entirely fill the grooves. At higher M (i.e., 40 g), the grooved wick becomes oversaturated throughout its entire length. The overly saturated wick possed higher thermal resistance in the condenser and obstructed pure radial heat conduction.

The increase in radial thermal resistance of the condenser shows a significant increase in condenser temperature. Moreover, the excess liquid accumulates at the evaporator section, resulting in additional marginal liquid pool resistance or marginally higher thermal resistance. Thus, a significant increase in radial thermal resistance supported by a marginal increase in liquid pool resistance leads to a significantly higher value of R at 40 g. Even at higher values of M (i.e., $M \geq 60$ g), the wick is already saturated and does not contribute to the radial heat flux in the condenser. Therefore, increasing M further only leads to a deeper liquid pool in the evaporator. Hence, R increases marginally, as the thermal resistance of the liquid pool does not change significantly with an increase in pool size because of the high thermal conductivity of R134a.

Figure 3.5 depicts the impact of M on R in the case of R513a. The plot demonstrates that increasing M leads to a decrease in R, contrary to the behavior of R134a. Specifically, the maximum R for R513a is observed at 20 g, regardless of $\dot{Q}$, and it decreases with an increase in fill fraction (i.e., 40 g, 60 g and 80 g) until R reaches a minimum value at 100 g of M.

The primary reason for this anomalous behavior with R513a is its low surface tension, which is 20-40% lower than that of R134a. Due to this, the rise height is calculated to be 6-8 mm, significantly smaller than the pipe ID ($\approx$12 mm). Conse-
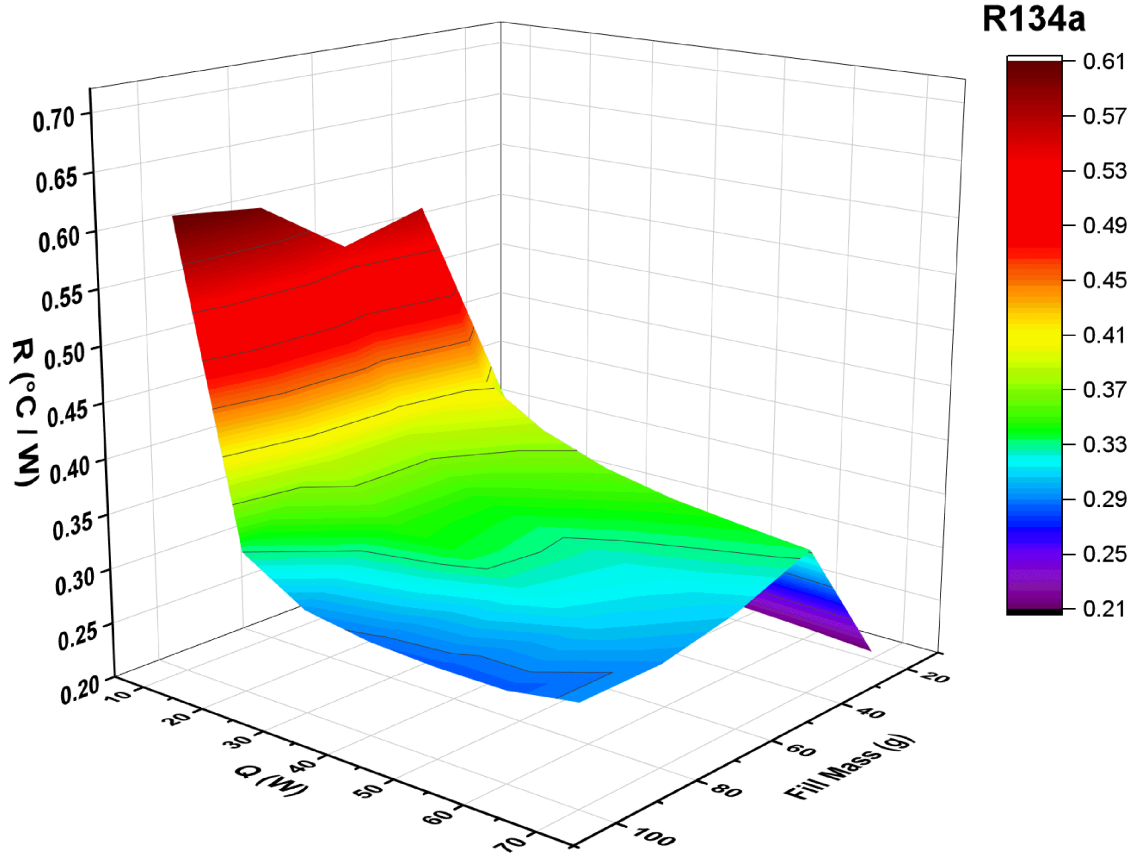
Figure 3.7: R variation of grooved heat pipe at θ=0.5° for R134a.

quently, at 20 g of M, the refrigerant is unable to spread to the upper circumferential interior surface of the evaporator, resulting in local dry-out in the evaporator. In this case, and as shown in figure 3.2, to spread the liquid thoroughly in the evaporator (dark blue + light blue), the calculated value of M g is 105 g (including refrigerant in the adiabatic section and in the condenser) of fill ratio. At 20 g of an M, irrespective of Q, the temperature data in the evaporator shows higher values for four thermocouples located outside liquid spread– refer to B.2.

At 40 g of an M, adding more fluid to the heat pipe and forming a deeper liquid pool in addition to h_{rise} covers a greater fraction of the interior surface area with refrigerant in the evaporator, thus reducing local dry-out. The temperature data in the evaporator shows higher values for three thermocouples located outside liquid spread– refer to B.1. Despite the added resistance in the evaporator from the extra
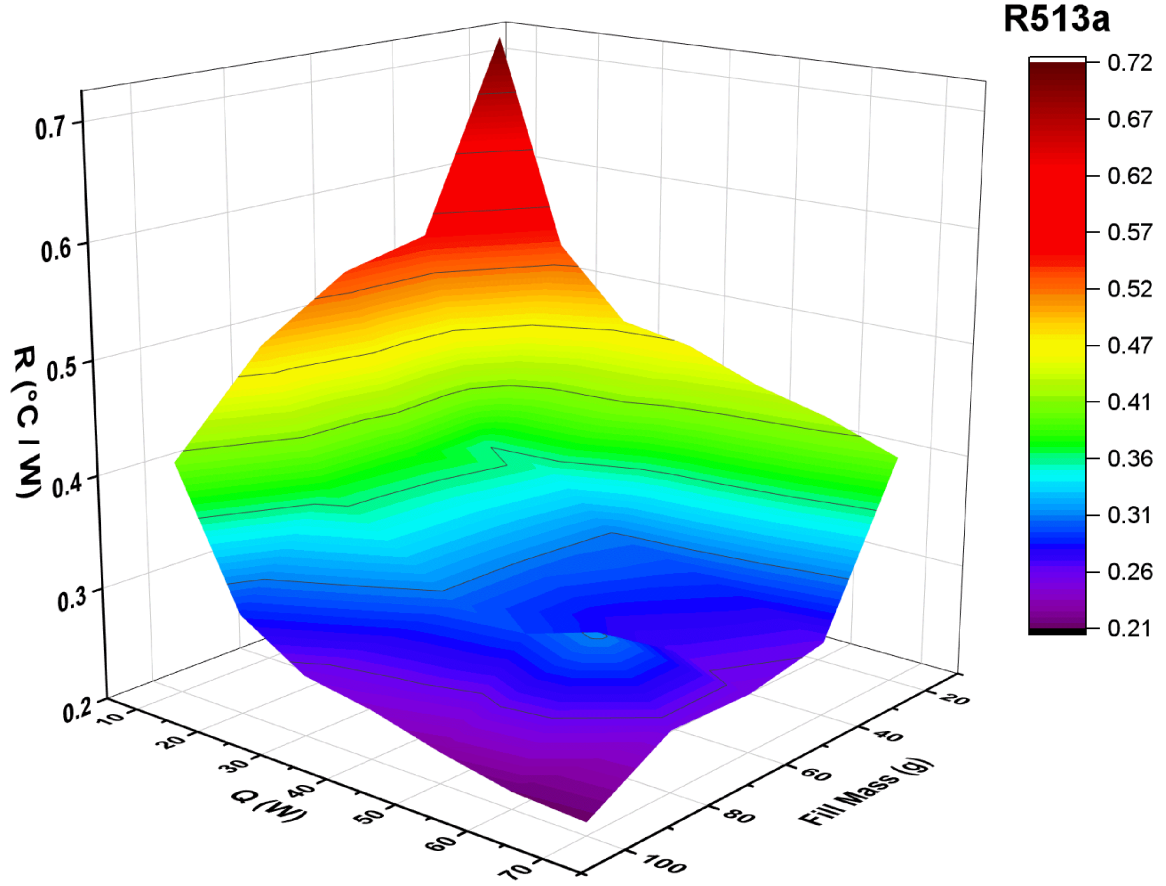
Figure 3.8: R variation of grooved heat pipe at $\theta=0.5°$ for R513a

liquid pool, the impact of local dry-out on R is more significant. Therefore, it can be experimentally observed that increasing M (i.e., 60 g and 80 g) decreases the overall R for the same reason. It is an important point to note that even increasing the M to 100 g leads to a decrease in R. This is because the liquid present in the grooves of the condenser and adiabatic section (roughly 10-12 g) prevents the evaporator from being completely filled (i.e., not exceeding 100% fill ratio). As a result, the R-value declines even at 100 g of M. In case M exceeds 105 g, the R is expected to increase.

ΔR variation with M and $\dot{Q}$

The comparison between the two working fluids for various combinations of $\dot{Q}$ and M can be seen in the color map in figure 3.6. In this color map, ΔR $(R_{R134a} - R_{R513a})$ is assigned different colors, with negative values appearing red indicating that R134a

performs better and positive values appearing blue indicating that R513a performs better. In general, the performance difference (or ΔR) of grooved heat pipes at a tilt angle of 4.5° is more strongly influenced by M than by the heat input ($\dot{Q}$). This implies that when switching to a different refrigerant, as long as the appropriate M is selected, the heat pipe will function effectively, regardless of the value of $\dot{Q}$. In figure 3.6, it is evident that for grooved heat pipes, only the mass flow rate M influences the value of ΔR, while maintaining consistency with Q.

At $M = 20\,\text{g}$, the heat pipe contains a relatively small amount of liquid, approximately 14-16 g, which is significantly less than the mass occupied by the fluid located within the grooves (25 g). As previously discussed, R134a has a maximum capillary rise height of 11 mm, while R513a has a maximum capillary rise height of 6-8 mm. As a consequence, R513a experiences significant local dry-out, whereas R134a remains unaffected. This discrepancy accounts for the superior performance of R134a at 20 g. Although the difference in surface tension values is only 20-40%, the resulting performance difference (as measured by ΔR) can reach up to 50%. In addition to adjusting the fill mass as a means to enhance the performance of a heat pipe using R513a, alternative improvements can be achieved by making modifications to its internal design. For instance, decreasing the groove spacing or the inner diameter (ID) are viable options to consider. A reduction in groove spacing results in an increase in capillary rise height. For the heat geometry of interest here, theoretical calculations suggest that a 20-50% decrease in groove spacing can uniformly coat the interior of the evaporator section with R513a. Additionally, reducing the internal diameter to a range of 6-8 mm can prevent local dry-out. However, decreasing the heat pipe diameter also reduces the cross-sectional area available for vapor flow, necessitating optimization to determine the optimal diameter for performance maximization. A detailed exploration of such optimization is reserved for future studies.

At an M of 40 g, the over-saturated wick with uniformly coated liquid in the interior of the heat pipe obstructs the heat flux in the radial direction of the condenser for R134a. Unlike the previous scenario (i.e., 20 g), uniformly coated liquid in the condenser adds significant radial resistance to the condenser. This leads to a higher condenser temperature than of 20 g case – refer to B.1. However, the smaller surface tension of R513a does not allow refrigerant to distribute all over the interior circumference. The liquid recedes to the bottom of the heat pipe, exposing the metal surface directly to vapor for condensation (shown in figure 3.2). Hence, for higher M, R513a outperforms R134a due to smaller surface tension.

Due to the higher radial resistance of the condenser in R134a, R513a demonstrates superior performance to R134a when the grooves are overfilled with M of 60, 80, and 100 g. Thus, for unsaturated or saturated wicks, where the M is ≤ 25 g, R134a is the recommended refrigerant. For $M \geq 40$ g, it is preferable to opt for a one-to-one replacement with a new refrigerant. However, replacing 20 g of R134a with a new refrigerant on a one-to-one basis is not recommended. Instead, modifying the M of the new R513a refrigerant can produce equivalent or enhanced performance. For instance, replacing 20 g of old R134a refrigerant with a new R513a refrigerant with a M of 80 or 100 g is a viable option. Alternatively, reducing the groove spacing or ID is also a feasible option

3.3.2 Helical grooved heat pipe at inclination $\theta \sim 0.5°$

The preceding subsections' trials were executed at $\theta = 4.5°$. The R vs. θ graph depicted in figure 3.3 demonstrates that R remains almost constant for angles greater than or equal to 0.5°. However, in order to reinforce the findings and account for the slightly higher thermal resistance observed for smaller θ, it is important to validate the results for angles close to 0.5°. Thus, we opted to perform experiments on smooth and grooved heat pipes at $\theta = 0.5°$. This is an attempt to assert the results' validity

for $\theta \geq 0.5°$ while disregarding smaller angles due to the heightened sensitivity of R with θ very near $\theta = 0°$.

Furthermore, the experimental results obtained for the grooved heat pipe at $\theta = 0.5°$ exhibit very little variation or no difference in performance when compared to the results obtained at $\theta = 4.5°$, as discussed earlier. Therefore, we have decided not to elaborate on these findings in this discussion. Instead, we shall present only the experimental findings for the grooved heat pipe at $\theta = 0.5°$.

These findings not only serve to confirm the results from the previous section, as depicted in figure 3.3, but also further reinforce the applicability of the results to most positive values of θ.
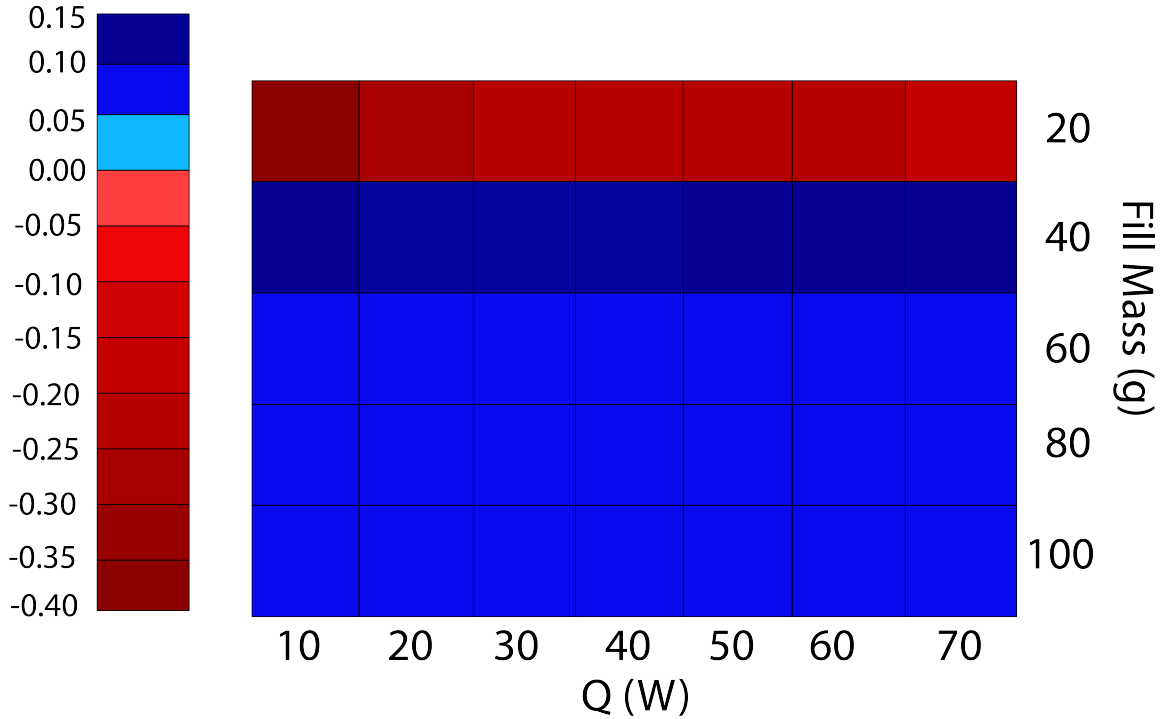
Figure 3.9: ΔR variation of grooved heat pipe at $\theta = 0.5°$

Figures 3.7 and 3.8 depict the results obtained at an inclination angle of 0.5°, which are remarkably similar to those obtained for R513a and R134a at an inclination angle of 4.5°, as demonstrated in the previous subsection, specifically in figures 3.4 and 3.5. Notably, the thermal resistance (R) values are marginally higher at $\theta =$

0.5° compared to $\theta = 4.5°$ for both refrigerants. This is due to the smaller gravity component ($g \sin \theta$) at lower inclination angles, which restricts the return of liquid from the condenser to the evaporator. For both refrigerants, the R-value decreases with $\dot{Q}$, exactly in a similar fashion discussed in the earlier subsection. This trend is attributable to an increase in vapor pressure, an increase in vapor density, and a decrease in liquid viscosity as discussed for an inclination angle of 4.5° in the previous subsection.

The ΔR variation, as illustrated in figure 3.9, evinces a comparable pattern for $\theta = 0.5°$ to that observed earlier for $\theta = 4.5°$, for most values of M. Moreover, akin to the instance of an inclination angle of 4.5°, R134a outperforms R513a at a M of 20 g, whilst R513a performs more favorably for M values surpassing $M \geq 40$ g. These results reinforce our antecedent findings and align with our conceptual understanding. A salient trend emerges for a M of 40 g, where R513a continues to exhibit superior performance, albeit with a greater differential of ΔR at $\theta \sim 0.5°$ relative to $\theta \sim 4.5°$. At 40 g, the increased depth of the liquid pool spread further within the evaporator due to smaller θ (2-3 times spread axially), curtailing the occurrence of local dry-out for R513a. The local dry out mentioned is observed as the temperature decreases across the evaporator [refer to B.1]. In the case of R134a, the condenser wick was already supersaturated, and the extra liquid introduced into the heat pipe did not increase the radial condenser resistance, unlike in the 20 g case. For fill masses of 60 g or higher, there is a slight increase in the actual values of R for both refrigerants at θ =0.5° compared to θ =4.5°. However, the ΔR values for θ =0.5° are similar to those observed in Figure 3.6 for θ =4.5°, and the underlying reasoning remains same.

In summary, the performance of both refrigerants, whether using smooth or grooved heat pipes at θ =0.5°, is very similar and comparable to θ =4.5°. Therefore, these findings can be extrapolated to any $\theta \geq 0.5°$. As the θ decreases, the values of R

increase slightly for both refrigerants, while maintaining a consistent ΔR for most M. Furthermore, in instances where M is small (i.e., $80\,$g or less), augmented liquid spreading actually enhances the performance of R513a with respect to R134a. However, this enhancement in performance is still not enough to completely counteract the return of liquid flow restriction that comes with decreasing the θ from $\theta = 4.5°$ to $\theta = 0.5°$. Thus, R at $\theta = 0.5°$ is slightly higher than R at $\theta = 4.5°$. During the transition from R134a to R513a, the same strategy can be employed regardless of the value of θ, as long as θ is greater than or equal to $0.5°$.

3.3.3 Thermal performance evaluation of a smooth heat pipe inclined at $\theta = 4.5°$

R variation with $\dot{Q}$ for R513a and R134a

Figures 3.10 and 3.11 present graphical performance data for R134a and R513a, respectively. The figures suggest that, for a fixed M, R decreases as $\dot{Q}$ increases. This behavior is similar to grooved heat pipes, where system performance is influenced by vapor density, vapor pressure, and liquid viscosity. For R134a, as $\dot{Q}$ increases from $10\,$W to $70\,$W (at $M = 20\,$g), the operating temperature rises from -4.95° C to 8.6° C. This temperature change results in an 80-100% increase in vapor density, a 40-60% increase in vapor pressure, and a 15-20% decrease in liquid viscosity [refer appendix tables B.13, B.14, and B.15]. Similar variations can be observed at higher M values.

For R513a, figure 3.11 shows a similar trend as of R134a between R and $\dot{Q}$. The reason also remains the same, upon increasing $\dot{Q}$ from $10\,$W to $70\,$W (at $M = 20\,$g), the operational temperature rises from -1.5°C to 12°C. This increase leads to an 80-100% increase in vapor density, a 50-80% increase in vapor pressure, and a 20-30% decrease in liquid viscosity [refer appendix tables B.16, B.17, and B.18]. Similar variations can be observed at higher M values. As with grooved heat pipes, in smooth heat pipes,

83

increasing the power input from 10 W to 20 W results in a more significant decrease in thermal resistance compared to increasing the power input from 60 W to 70 W for both refrigerants.
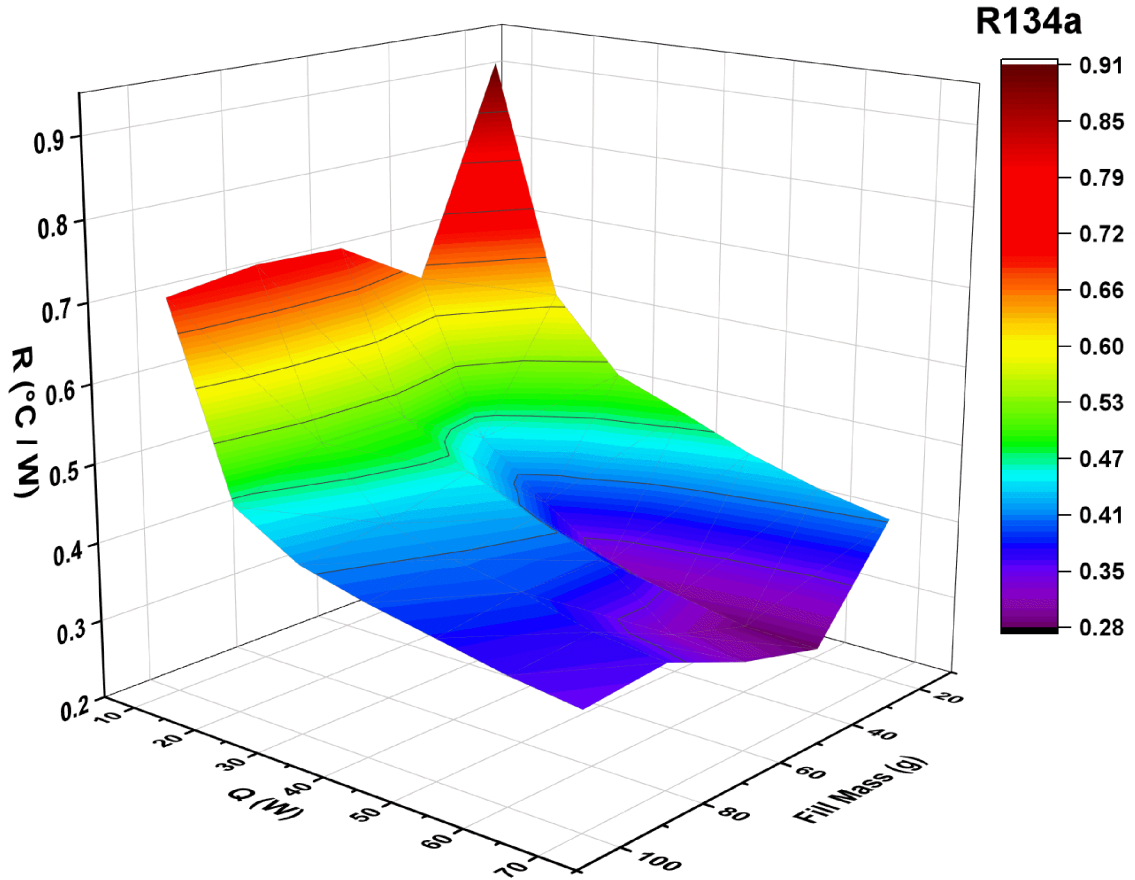
Figure 3.10: R variation of R134a for smooth heat pipe at $\theta = 4.5°$

R variation with M for R134a and R513a

As explained in the introduction, multiple parameters influence the overall thermal resistance of a heat pipe. However, altering the value of M can significantly impact R in two ways. Firstly, it can result in local dry-out (R_{dryout})[1], directly affecting R. Secondly, the presence of a liquid pool in the evaporator (R_{pool})[2] can also impact R. Nevertheless, in grooved heat pipes, as discussed earlier and in contrast to smooth

---

[1]R_{dryout}: the resistance due to local dry-out in evaporator
[2]R_{pool}: the resistance due to liquid pool in evaporator
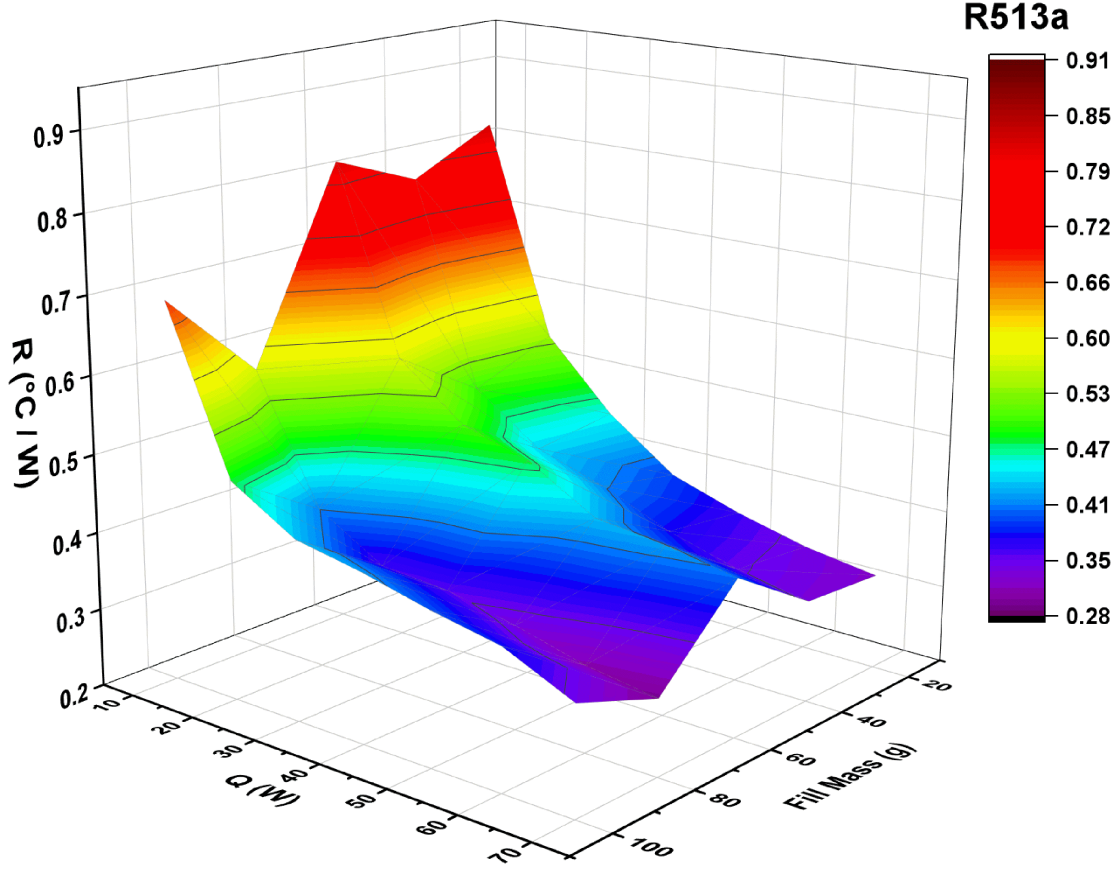
Figure 3.11: R variation of R513a for smooth heat pipe at $\theta=4.5°$

heat pipes, the thermal resistance caused by the liquid pool is considerably reduced due to the capillary rise of the refrigerant, enabling more uniform liquid spreading in the evaporator. Therefore, we avoided considering R_{pool} and R_{dryout} variables in the grooved heat pipe. To comprehensively understand the effect of variables in question and, by extension, the variation of R with M, we have presented a schematic in figure 3.12, based on available literature [99, 100].

The impact of local dry-out (R_{dryout}) on R is determined with reference to the evaporator volume that is both dry and exposed to heat. Symbolically, $R_{\text{dryout}} \propto (V_e - V_{\text{actual}})$, where V_e represents the evaporator volume and V_{actual} represents the actual refrigerant volume. The relationship between R_{dryout} and M is linear with a
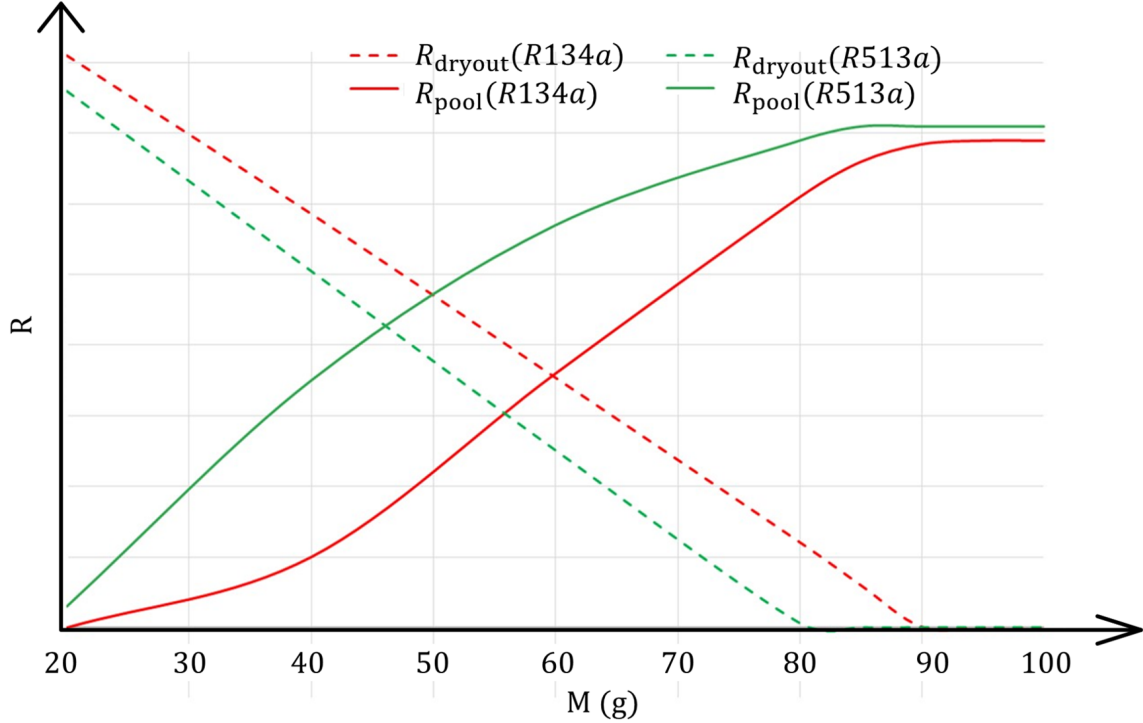
Figure 3.12: R variation due to liquid pool resistance and local dryout [99]. The plotted values for R_{pool} and R_{dryout} are based on speculative assumptions derived from experimental observations and existing literature. It is important to note that there is currently no specific method available to precisely estimate R_{pool} and R_{dryout}.

slope of $-M/\rho$, as illustrated in figure 3.12. However, it is important to note that R_{dryout} expression is only applicable to smooth heat pipes and does not take into account capillary rise in grooved heat pipes. The effect of local dry-out on R is consistently greater for R134a compared to R513a due to its higher liquid density (by 10%), which results in a smaller slope. Additionally, at low values of M (i.e., 20 g), the differences in R of both refrigerants due to local dry-out are minimal, as the fill ratio of R513a is only higher by 1-1.5% (corresponding to the lower density of R513a). For higher values of M (i.e., 80 g), the differences in R increase significantly due to the larger fill ratio differences (i.e., 10%). Local dry-out becomes negligible at a 100% fill ratio, corresponding to $M \approx 80\,\mathrm{g}$ for R513a and $M \approx 90\,\mathrm{g}$ for R134a.

On one hand, several researchers have demonstrated the significant impact of liquid

pool depth on thermal resistance [99–101]. It has been observed by researchers that as the depth of the pool increases, there is a rise in the thermal resistance (R_{pool}), although the rate of increase slows down until it reaches a plateau, as depicted in figure 3.12 [99, 100]. Once the plateau is reached, the thermal resistance (R_{pool}) remains constant regardless of further increases in the fill ratio. Figure 3.12 illustrates this trend for both refrigerants, where the thermal resistance (R_{pool}) caused by the liquid pool size grows rapidly with increasing M until it reaches a plateau for larger fill fractions. R134a exhibits a similar trend, but with smaller values at a given M due to its higher density and smaller fill ratio, and therefore smaller pool depth. Moreover, R134a also has higher thermal conductivity. As a result, a higher M is required to achieve the plateau. Furthermore, the plateau value of R_{pool} depends on the thermophysical properties of the vapor [99], and R134a demonstrates lower R due to its higher thermal conductivity of liquid phase by 10%.

In case of R134a, the variation of overall thermal resistance (R) with liquid fill mass is shown in figure 3.10. At low M (20 g), the overall thermal resistance is high due to the dominant effect of R_{dryout} in the evaporation section, despite small R_{pool} as shown in figure 3.12. The occurrence of local dryout can be observed by comparing the elevated temperatures of the four thermocouples (from 2nd to 5th) with the 1st thermocouple temperature – refer to B.6. As M increases to 40 g, the sum of R_{dryout} and R_{pool} reduces drastically, resulting in a decrease in R. The reduction in R_{dryout} can be seen from the fact that only the last three thermocouples (3rd to 5th) show higher temperatures. At a higher fill mass still (e.g., 60 g), the overall thermal resistance R increases due to an increase in the sum of R_{pool} and R_{dryout}. The occurrence of local dry-out further decreases, and only the last two thermocouples (4th and 5th) show higher temperatures. At 80 g, the decrease in R_{dryout} is equivalent to the increase in R_{pool}, resulting in an insignificant change in R. Only the 5th thermocouple shows a higher temperature at this point. Furthermore, when M reaches 100 g (fill ratio $>$

87

100%), R_{dryout} is eliminated, and the temperature remains uniform throughout the evaporator (see refer to B.6). At this point, R_{pool} increases and reaches a plateau. Hence, the initial rise in R_{pool} until it reaches a plateau, coupled with the subsequent decrease in R_{dryout}, results in the overall thermal resistance R remaining relatively constant.

Figure 3.11 illustrates the performance of R513a with respect to M. The primary reason for the discrepancy with R134a is the higher fill ratio of R513a at a given fill mass (M). At an M of 20 g i.e., at a fill ratio of less than 20%, the most significant impact on R is from R_{dryout}, with a small contribution from R_{pool}. A state of local dry-out is evident from the higher temperatures of the last three thermocouples (3rd to 5th) compared to the first two thermocouples in the evaporator section, as shown in B.6. When the mass flow rate M is increased to 40 g, the combined effect of an increase in R_{pool} and a decrease in R_{dryout} is almost balanced. As a result, there is only a small decrease in the total thermal resistance R compared to the case of 20 g. The local dry-out is confirmed by the presence of abnormally higher temperatures for the last two thermocouples (4th and 5th) compared to the first three. At $M=60$ g, the increase in R_{pool} is slightly higher than the decrease in R_{dryout}, leading to a slight increase in R. The local dry-out is confirmed by abnormally higher temperatures for the last thermocouple (5th) compared to the first three. However, it is worth noting that in figure 3.11, the changes in R for 20 g, 40 g, and 60 g are hardly noticeable. At an M of 80 g (fill ratio up to 99%), R reaches its minimum value because the influence of R_{dryout} on R becomes negligible, and only R_{pool} affects R. No local dry-out is observed, as seen from the uniform temperature distribution in the evaporator, as shown in B.6. Further increasing M to 100 g (fill ratio of approximately 120%) results in a marginal increase in R since R_{pool} has not yet reached a plateau.
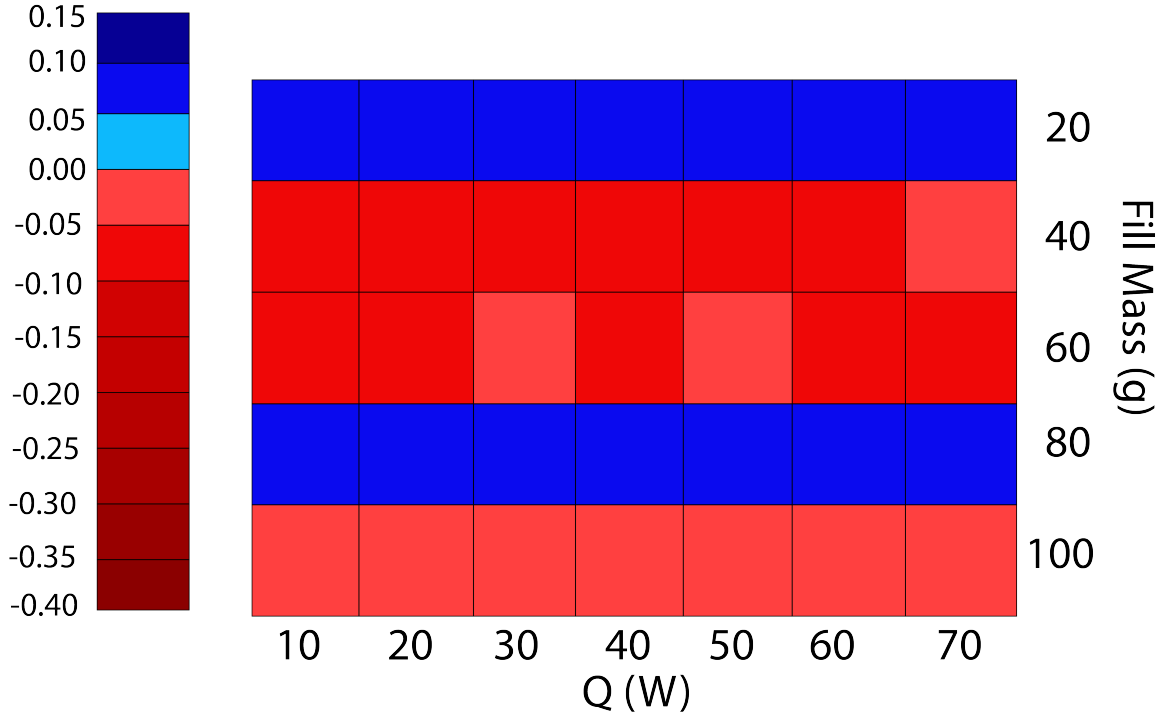
Figure 3.13: ΔR variation for smooth heat pipe at $\theta=4.5°$

ΔR variation with M and $\dot{Q}$

Similar to the grooved heat pipe shown in figure 3.13, the difference in efficacy (i.e., ΔR), of a smooth heat pipe containing R513a or R134a depends on the fill mass (M) rather than the heat input ($\dot{Q}$). The variation of ΔR with $\dot{Q}$ remained consistent for each M, except at $40\,\mathrm{g}$ ($70\,\mathrm{W}$) and $60\,\mathrm{g}$ ($30\,\mathrm{W}$ and $50\,\mathrm{W}$), where changes were in any event small. Therefore, it can be concluded that ΔR remains largely independent of $\dot{Q}$.

In figure 3.13, it can be observed that at a mass flow rate of $M = 20\,\mathrm{g}$, R513a outperforms R134a in terms of efficacy. The primary factor contributing to this performance difference is local dry-out since the resistance from the liquid pool is very similar for both fluids (refer to Figure 3.12). Specifically, R513a exhibits a higher fill ratio, ranging from 0.9% to 1.5%, which is in contrast to R134a.

At higher M, specifically at $40\,\mathrm{g}$ and $60\,\mathrm{g}$, R134a outperforms R513a, as depicted in figure 3.13. In contrast to the case at $20\,\mathrm{g}$, in this regime, the increase in thermal resistance of the liquid pool becomes highly sensitive to the depth of the pool. The steep increase in R_{pool}, attributed to a 4.5% higher fill ratio of R513a compared to R134a, results in a positive ΔR, favoring R134a. As M increases to $60\,\mathrm{g}$, the rate of increase of R_{pool} becomes smaller and approaches the plateau value. However, even at $M = 60\,\mathrm{g}$, the difference in fill ratio, reaching up to 8%, still favors R134a by the same margin of ΔR.

At $M = 80\,\mathrm{g}$, R513a outperforms R134a, primarily due to its higher fill ratio,which can be up to 10% higher than that of R134a. The higher fill ratio of R513a helps to completely eliminate local dry-out, while for R134a, local dry-out still persists, as shown in figure 3.12. Moreover, the effect of the liquid pool on ΔR ultimately becomes marginal for both refrigerants, as both curves approach the plateau, indicating that a further increase in M has little impact on the difference in efficacy (ΔR) between R513a and R134a.

At a fill mass of $100\,\mathrm{g}$, R134a exhibits a slight advantage in performance. Both R513a and R134a result in overfilled heat pipes, with fill ratios of 110% and 120% respectively, rendering R_{dryout} irrelevant for comparison. Furthermore, the thermal resistance due to the liquid pool (R_{pool}) has already reached a plateau for both refrigerants, as shown in figure 3.12. As a result, ΔR depends only on the plateaued value of R_{pool}, which in turn is influenced by the thermophysical properties of the refrigerants. With R134a having a slightly higher thermal conductivity (10%) compared to R513a, it performs better by a marginal amount.

To summarize, dry-out considerations matter most when one of two limiting cases is approached: (i) an evacuated heat pipe, and, (ii) a heat pipe that is very close to

100% fill fraction such that the evaporator is almost completely flooded with liquid. In either case, R513a is the more effective working fluid because of its smaller density suggesting comparatively less (or no) exposed bare metal in the evaporator section. By contrast, and for intermediate fill fractions or fill fractions in excess of 100%, dry-out is of secondary and negligible importance, respectively. Here, a more important determinant of heat pipe performance is the depth of the liquid pool that accumulates in the evaporator and which represents a potential barrier to heat transfer. R134a benefits from having a shallower liquid pool and higher thermal conductivity. Hence, for intermediate or large M, a one-to-one replacement of refrigerants is inadvisable, but adjusting the M could make the interchange of refrigerants much more palatable.

3.4 Conclusions

In this study, two different types of experiments were run to see how well the low GWP refrigerant R513a performed as a prospective R134a replacement. The experimental research indicates that the smooth heat pipe configuration exhibits the best performance when operated near 100% fill ratio for both R513a and R134a refrigerants, irrespective of the angle of inclination (θ). This suggests that achieving a high fill ratio is crucial for maximizing heat transfer efficiency in smooth heat pipes. In the case of helical grooved heat pipes, the findings reveal that R134a performs optimally when the grooves are completely saturated. The saturation point for the grooves, considering the specific dimensions of the heat pipe and refrigerant properties, occurs at approximately 25 g of fill mass. This implies that ensuring complete groove saturation is vital to achieving the best performance with R134a in helically grooved heat pipes. In contrast, when considering a grooved heat pipe with R513a refrigerant, the optimal performance is achieved when the fill ratio is close to 100%.

Transitioning from R134a to R513a in smooth heat pipes shows that, at very small fill masses (20 g) and close to 100% fill ratio (80 g), R513a demonstrates superior per-

formance compared to R134a. In these particular scenarios, it is possible to replace the refrigerant on a one-to-one basis without sacrificing performance or changing design parameters. However, for intermediate fill masses or overfilled conditions, R134a outperforms R513a. Consequently, a direct one-to-one transition between these refrigerants is not feasible. To achieve equivalent performance between the two refrigerants in such cases, the fill mass must be adjusted accordingly.

For helically grooved heat pipes, a direct one-to-one replacement from R134a to R513a is possible in all fill mass cases except for undersaturated or saturated wick conditions (i.e., 20 g). In oversaturated wick scenarios, a direct replacement is feasible. However, for undersaturated or saturated wicks, the transition can only be achieved by modifying the fill mass or adjusting the internal wick design. The results at $\theta = 0.5°$ indicate the validity of the transition strategy for all $\theta \geq 0.5°$, exhibiting a similar pattern

Chapter 4

LowTHeR: A GUI for Heat Pipe Design and Optimization

4.1 Introduction

LowTHeR is a Matlab-based design tool for assessing and optimizing heat pipe designs and for diagnosing the performance of a bank of heat pipes. 'LowTHeR' stands for **Low T**emperature **He**at **R**ecovery. The standalone executable of this software does not require the installation of Matlab.

Development of LowTHeR was led by Muhammad Rizwanur with subsequent additions by the author. More specifically, I expanded the software's capabilities related to wicks and refrigerants, as well as added material to the user manual. I then applied LowTHeR in contextualizing select experimental results from Chapter 3. Please note that LowTHeR has not been described in a previous archival publication nor in a previous thesis, either from U. Alberta or elsewhere.

4.1.1 Purpose and scope

LowTHeR v2.0 has four distinct capabilities. The coding architecture is shown in figure 4.1.

- **Working fluid, one tab:** To analyze a number of key parameters, such as the Merit number, wicking factor, degree of superheat etc., so as to guide the user in selecting a working fluid appropriate to the operating conditions.

- **Design assessment (single), one tab:** To map the operating point relative to the limiting conditions associated with boiling, entrainment, viscosity, etc. Results are presented graphically in terms of the heat pipe "fundamental diagram."

- **Design optimization (single), one tab:** To prescribe the optimum combination of design parameters (wick thickness and mesh number for screen-type wicks, groove depth and number of grooves for axial groove-type wicks) and thereby provide design insight on how to increase performance while assuring that operational failure will not occur.

- **Design assessment (bank), three tabs:** To assess the operation of a bank of heat pipes and to predict, for prescribed exterior conditions, the temperature of the air supplied to the interior space and/or the exhaust air temperature and number of heat pipes required.

The coding architecture is depicted in figure 4.1. As suggested by the above description, `LowTHeR` v2.0 does not extend to heat pipes containing multi-screen wicks. However, this functionality could be added at a later point in time.

4.1.2 System Overview

`LowTHeR` v2.0 offers users the flexibility of inputting heat pipe design specifications, of choosing from a library of working fluids, of determining the most suitable working fluid pertinent to the operating conditions, and of assessing performance over a wide range of operating temperatures and heat loads. Technical details are described in the following sections.

4.1.3 Graphical user interface overview

The GUI has input and output segments that are distributed categorically over six different tabs – see e.g. figure 4.2.
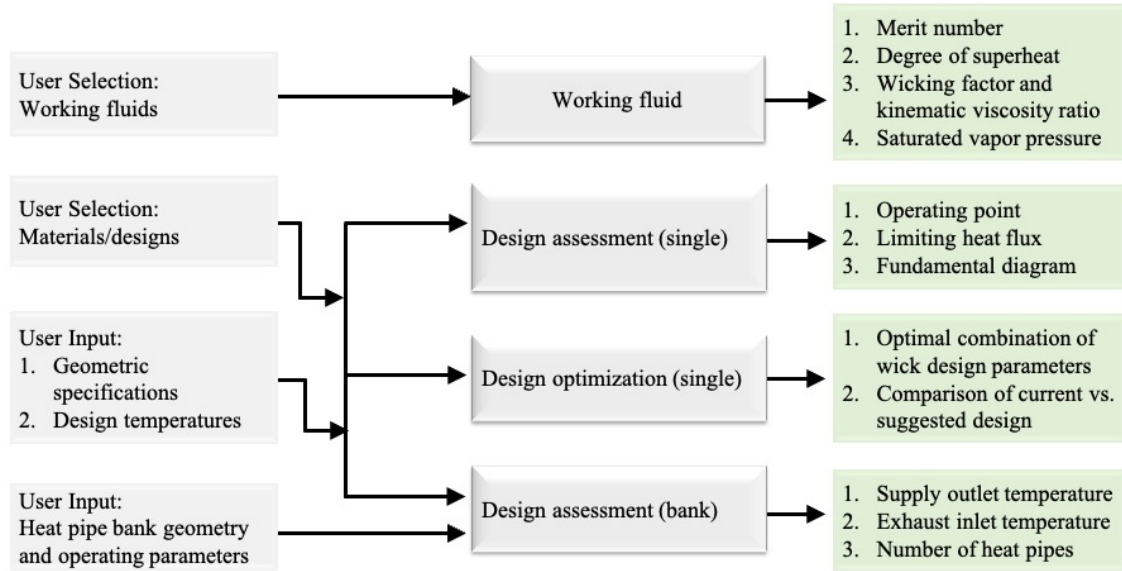
Figure 4.1: Code architecture. The right hand side boxes (in green) indicate module outputs.

The far left-hand side of the GUI contains user input fields corresponding to operating conditions, material selection and heat pipe geometric specifications. The data input in this section is global and is therefore available to all of the tabs. Note, however, that none of these data are used when selecting the working fluid, i.e. the tab `Working fluid` is self-contained and does not make reference to the global variables in question. In the following sections, we describe tabs and panels in greater detail.

User selections/inputs

The panel titled `Materials/design` asks the user to select, from drop down lists, the following heat pipe properties:

a. Working fluid,

b. Container material,

c. Wick material,

d. Wick type.

The user is also asked to provide two angles, namely

95
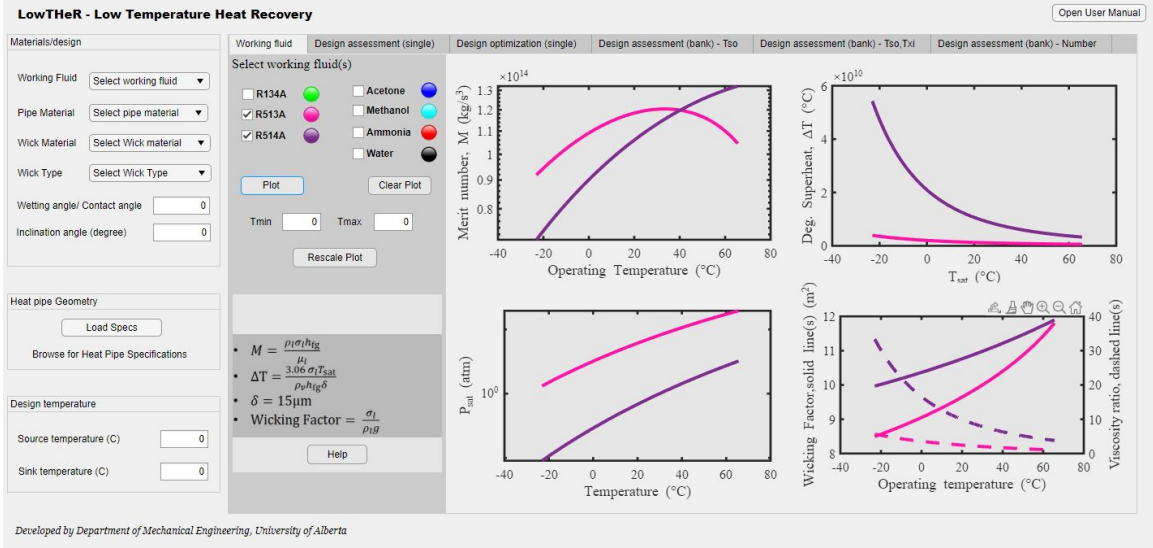
Figure 4.2: User Interface, Tab 1 - `Working fluid`.

a. Wetting angle for the wick material (default value of 0° indicating, for example and in case of a water-based working fluid, a perfectly superhydrophilic surface),

b. Heat pipe inclination angle, i.e. the angle of inclination assuming that the evaporator is situated below the condenser (default value of 0° indicating a horizontal heat pipe).

The drop down menus are linked to built-in libraries that specify the necessary material/fluid property values over a wide range of operating temperatures. Once selections are made from the drop down lists, property values are then automatically loaded or calculated. In the case of the working fluid, the data in question includes the latent heat of vaporization (h_{fg}), liquid-density (ρ_l), vapor density (ρ_v), vapor pressure (P_v), surface tension (σ), molecular weight (M), liquid dynamic viscosity (μ_l), vapor dynamic viscosity (μ_v), liquid thermal conductivity (K_l), effective wick thermal conductivity (K_e), and shell thermal conductivity (K_s).

These properties are calculated at operating temperature (T_{op}), which is the arithmetic average[1] of the source and sink temperatures. Both the source and sink tem-

---

[1]In computing an arithmetic average of the source and sink temperatures, we implicitly assume that the evaporator and condenser are of equal length.

peratures must fall within the operating limits for the working fluid of interest.

Once the above-mentioned selections are made, an Excel spreadsheet, containing an ordered list of relevant geometric parameters is to be loaded in the panel titled `Heat pipe geometry`. The input parameters in question are the (i) mesh number, n, (ii) wick thickness, h, (iii) wire diameter (iv) pipe inner diameter, d_i, (v) vapor core diameter, d_v, (vi) condenser length, L_c, (vii) adiabatic length, L_a, (viii) evaporator length, L_e, (ix) pipe outer diameter, d_o, (x) groove depth, h, and, (xi) number of grooves, N. Of these, (i-iii) are required for screen-type wicks whereas (x-xi) are required for wicks consisting of axial grooves. In either case, the parameters related to the other wick type should be set to zero in the Excel file. Note, the sequence of these parameters is to be strictly maintained as described above.

Tab 1 - `Working fluid`, figure 4.2

The first tab allows the user to compare five parameters that are essential in the selection of an appropriate heat pipe working fluid. Unlike other tabs, `Working fluid` does not use any input values from the far left panels, i.e. `Materials/design`, `Heat pipe geometry` and `Design temperatures`. `Working fluid` contains a list of working fluids from which the user can select one or more so as to compare Merit numbers, degrees of superheat, saturated vapor pressures, wicking factors and kinematic viscosity ratios. These variables, and their significance to heat pipe design, are outlined below.

- **Merit number[2]:** The Merit number, serves as a helpful indicator of the ability of a working fluid to transfer heat (large Merit numbers are favored). It is defined as

$$\text{Merit number} = \frac{\rho_l \sigma h_{fg}}{\mu_l}$$

---

[2]Merit number predictions made by `LowTHeR` are validated with data from Advanced Cooling Technologies, Inc. https://www.1-act.com/merit-number-and-fluid-selection/

- **Degree of superheat:** As the heat load increases, so too does the temperature drop across the wick in the evaporator section. If the temperature difference exceeds the degree of superheat of the working fluid, nucleate boiling may occur. The onset of nucleate boiling within the wick is disadvantageous: it may interfere with liquid circulation leading, eventually, to dry out. The degree of superheat, ΔT, is defined as [58]

$$\Delta T = \frac{3.06 \sigma_l T_{\text{sat}}}{\rho_v h_{fg} \delta_{\text{th}}},$$

  where δ_{th} is the thermal boundary layer thickness, a representative value for which is $\delta_{\text{th}} = 15 \, \mu\text{m}$ [58]. Furthermore, T_{sat} is the saturated vapor temperature and ρ_v is the vapor density. Working fluids exhibiting higher degrees of superheat carry a lower likelihood of nucleate boiling.

- **Saturated vapor pressure:** The saturated vapor pressure, P_{vap}, is important from the perspective of material selection [58]. Heat pipes are often bonded to radiator plates. It is therefore necessary to know the working fluid vapor pressure at the soldering temperature in order to determine the minimum wall thickness necessary to avoid material failure during soldering. This minimum wall thickness can be determined from

$$t_{\text{min}} = \frac{P_{\text{vap}} R_i}{\Omega},$$

  where R_i is the pipe inner radius and Ω is the 0.1% proof stress of the pipe material. A working fluid with a lower vapor pressure will require a lower wall thickness and will therefore incur substantially lower construction costs.

- **Wicking factor:** The wicking factor, $\sigma_l/(\rho_l g)$ where g is gravitational acceleration, measures the ease with which liquid may be transported against gravity by surface tension. Large wicking factors are favored, particularly in instances where the evaporator is located above the condenser.

- **Kinematic viscosity ratio:** The kinematic viscosity ratio, ν_v/ν_l, accounts for the severity of viscous and shear losses [61]. Small kinematic viscosity ratios are favored in heat pipe design.

Tab 2 - `Design assessment (single)`, **figure 4.3**

The second tab allows the user to assess the performance of a single heat pipe by showing, within the heat pipe fundamental diagram, the operating line and the operating point relative to the limiting heat fluxes imposed by the sonic, capillary, boiling, entrainment and viscous limits[3]. In drawing the fundamental diagram, it is assumed that the wick or axial grooves are exactly filled with liquid.

The operational heat flux ($\dot{Q}_{\mathrm{op}}$) is always constrained by the heat pipe limitations, referred to as $\dot{Q}_{\mathrm{Limiting}}$, which are discussed in Chapter 1 and illustrated in figure 4.3. The software incorporates several limiting equations, described as follows:

1. Viscous limit: To account for the viscous limit, we utilized (1.1).

2. Sonic limit: To consider the sonic limit, we utilized (1.2).

3. Entrainment limit: To consider the entrainment limit, we utilized (1.3).

4. Boiling limit: To consider the boiling limit, we utilized (1.4).

5. Capillary limit: To consider the capillary limit, we utilized (1.5)

Tab 3 - `Design optimization (single)`, **figure 4.4**

The third tab allows the user to augment heat pipe performance through optimization. The optimization in question is achieved by making the least possible changes to the wick geometry. This feature is especially helpful when the design specified by

---

[3]Note that not all five limiting curves may be visible in the "fundamental diagram," i.e. one or more of the curves may lie out-of-range depending on the heat pipe operating conditions and the vertical axis limits. Such is the case in figure 2 where the viscous limit does not appear.
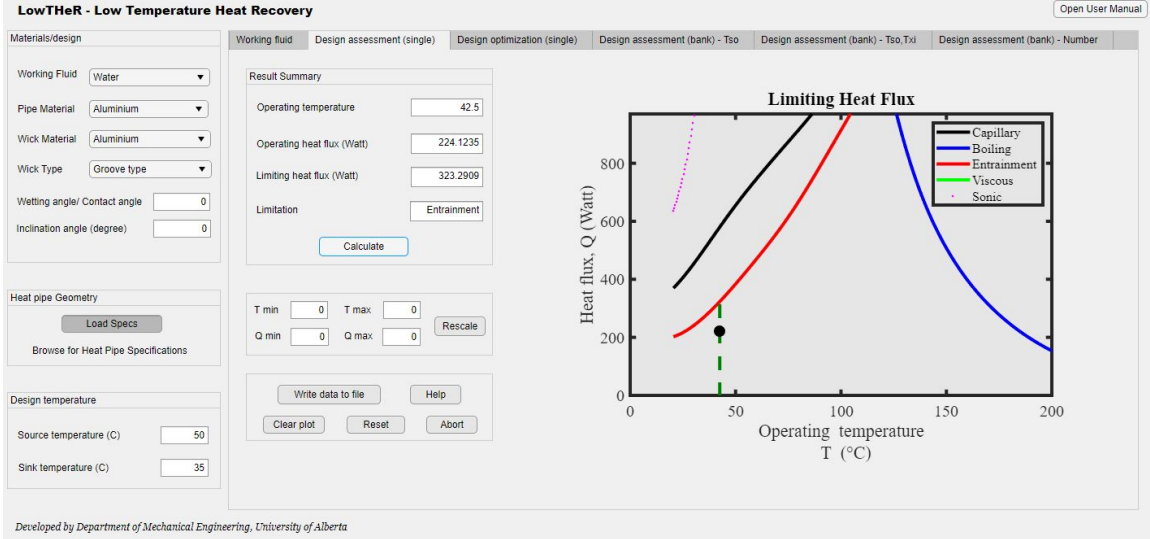
Figure 4.3: User interface, Tab 2 - `Design assessment (single)`.

the data input on the left-hand side of the GUI yields an operating point in excess of the maximum allowable heat flux. In such instances, `LowTHeR` will modify the wick properties so as to either increase the limiting heat flux, decrease the operating heat flux or both. Displayed in the third tab are (i) a table that indicates, as a function of the wick properties, the rate of heat transfer both for the previous and the current (optimized) design, and, (ii) a surface plot showing all those operating heat fluxes that are at least 5% below the minimum of the limiting heat fluxes associated with the sonic, capillary, boiling, entrainment and viscous limits. Optimization typically increases each of the limiting heat fluxes by a comparable amount. Therefore, the process of optimization typically does not change the limiting condition type. In other words, if the original design is limited by capillarity, it is very likely that the capillary limiting curve will again fall below its counterpart limiting curves when considering the optimized design.

While the first, second, and third tabs of `LowTHeR` allow the user to assess and optimize the performance of a single heat pipe, the fourth, fifth and sixth tabs focus on performance assessments for a bank of heat pipes. Given the expanded focus

100
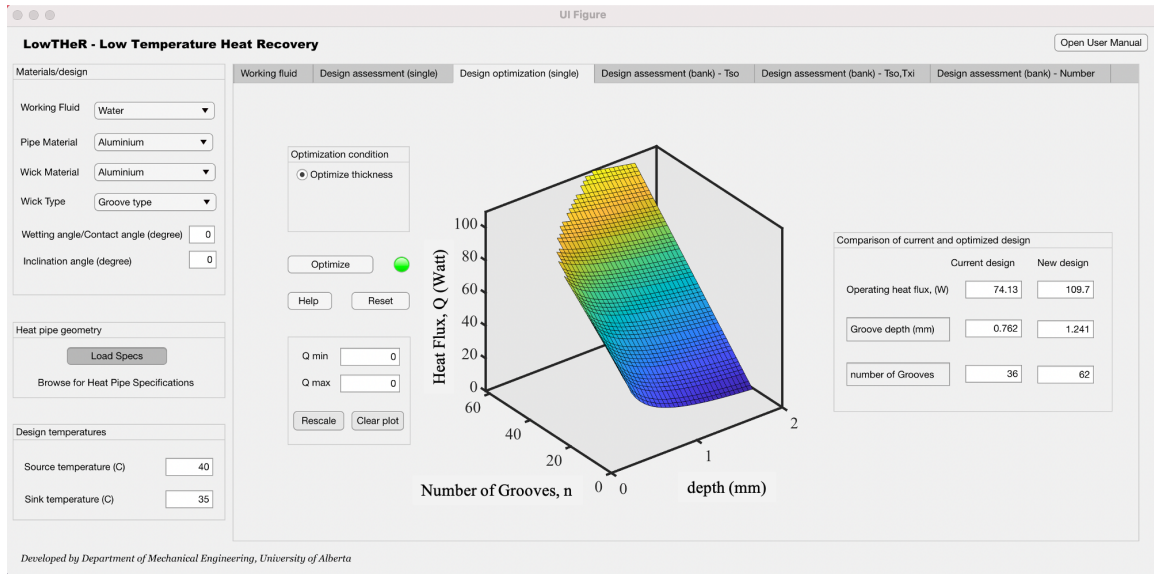
Figure 4.4: User interface, Tab 3 - `Design optimization (single)`.

associated with studying a heat pipe bank, some additional information is required related, for example, to the number of heat pipes within the bank, the thermodynamic conditions of the air flowing over the heat pipe bank, etc. Note that the source and sink temperatures specified in the far left column are not required for Tabs 4, 5 and 6.

4.2 Governing equations

4.2.1 Heat pipe operational performance

To model the heat flows within a heat pipe, an analogous thermal resistance network can be constructed by considering each component from the source to the sink and how these components are interconnected, i.e., through a combination of series and parallel resistors – see figure 4.5. Table 3 gives the mathematical expressions used to estimate the individual resistances and their relative magnitudes. Apparent from the tabulated values, the resistances of the liquid-vapor interface and of the vapor core are very small; as such these contributions are ignored such that $R_3 = R_4 = R_5 = 0$. Conversely, the resistance of the pipe wall is significantly larger than that of any other component. Therefore, and in the context of the thermal circuit diagram of figure 4.5, we model the pipe wall as being "open circuit" such that $R_s \to \infty$.
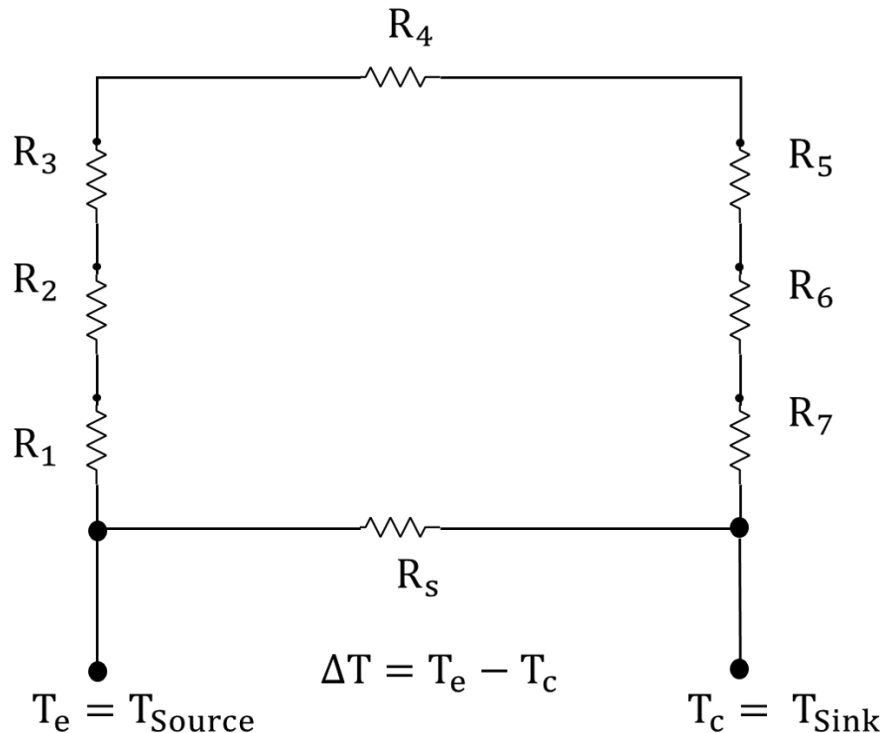
Figure 4.5: Thermal resistance network model across the heat pipe.

Table 4.1: Different thermal resistances associated with the heat pipe [61]. Variables are defined as follows – r_o: outer radius, r_i: inner radius, r_v: vapor core radius, R: gas constant, L_a: adiabatic length, L_e: evaporator length, L_c: condensor length, ΔP_v: pressure difference between condensor and evaporator, K_s: envelope thermal conductivity, T: interface temperature, A_e: evaporator area, A_{wall}: wall crossection area, A_{w}: wick crossection area, $\Delta T_{4/6}$: interface temperature difference. The subscripts 'e' and 'c' stand for evaporator and condenser, respectively.

Term	Resistance	Description	Scale
R_1, R_7	$\dfrac{\ln \frac{r_o}{r_i}}{2\pi L_e K_s}$	Wall conduction (radial)	10^{-1}
R_2, R_6	$\dfrac{d}{K_w A_e} = \dfrac{\ln \frac{r_i}{r_v}}{2\pi L_e K_e}$	Wick conduction (radial)	10
R_3, R_5	$\dfrac{(2\pi RT)^2 RT^2 L^2 P_v \Delta T_{4/6}}{L^2 P_v A_e}$	Liquid-vapor interfacial	10^{-5}
R_4	$\dfrac{RT^2 \Delta P_v}{\dot{Q} L P_v}$	Vapor advection (axial)	10^{-8}
R_s	$\dfrac{L_e + L_a + L_c}{A_w K_e + A_{\text{wall}} K_s}$	Wall conduction (axial)	10^3 (open circuit)

The effective resistance can therefore be calculated using the following formula:

$$R_{\text{e}} = R_1 + R_2 + R_6 + R_7 = 2R_1 + 2R_2 \tag{4.1}$$

Here, R_{e} is the equivalent thermal resistance of the heat pipe. This quantity is related to the heat pipe operating heat flux via

$$\dot{Q}_{\text{op}} = \frac{\Delta T}{R_{\text{e}}} \tag{4.2}$$

4.2.2 Effective thermal conductivity

In a heat pipe, the effective thermal conductivity of a wick saturated with liquid is a critical parameter for calculating heat transfer. LowTHeR incorporates three different types of wicks and uses separate techniques for calculating thermal conductivity. These are detailed in the following subsections.

Type 1: Wrapped screen- or mesh-type wick [61]

Wrapped screen-type wicks are made by wrapping a metal fabric or mesh around a forming mandrel and then the wick can be inserted into the heat pipe. These

wicks have moderate capillary pumping capability and a higher permeability than do sintered wicks [61]. Screen-type wicks are often preferred for heat pipes with complex shapes [61] The thermal conductivity (K_e) of screen-type wick can be approximated as follows:

$$K_{\text{e}} = \frac{k_l[(k_l + k_w) - (1 - \epsilon)(k_l - k_w)]}{(k_l + k_w) + (1 - \epsilon)(k_l - k_w)} \tag{4.3}$$

Here ϵ represents the porosity, k_l represents the thermal conductivity of the liquid refrigerant, and k_w represents the thermal conductivity of the wick material.

Type 2: Axial grooved wicks [61]

Axial grooves are used to enhance the capillary forces that drive the return flow of liquid in a heat pipe. Regularly-spaced axial fins are cut into the inner surface of the heat pipe along its length. The effective thermal conductivity of the wick is dependent on the degree of liquid saturation. Consistent with the commentary above, we assume a wick that is exactly flooded with liquid in which case the effective thermal conductivity can be evaluated from [61]

$$K_{\text{e}} = \frac{(w_f k_l k_w \delta) + w k_l (0.185 w_f k_w + \delta k_l)}{(w + w_f)(0.185 w_f K_f + \delta k_l)} \tag{4.4}$$

In the case of trapezoidal-shaped axial grooves, w_f denotes the thickness of the fin located at the top of the groove, and w represents the thickness of the base of the groove. However, for rectangular-shaped grooves, the fin thickness (w_f) is equal to the groove base thickness (w). Additionally, the parameter δ corresponds to the depth of the groove.

Type 3: Sintered wicks [61]

Sintered wicks are produced using a metal powder manufacturing process where, at high temperatures, the metal powders are bonded together and also to the heat pipe wall, resulting in a porous medium. For the calculation of the effective thermal conductivity, it is again assumed that the wick is fully saturated with liquid. Chi's theory provides a framework for determining the effective thermal conductivity of

liquid-saturated sintered wicks. On the basis of this theory, the effective thermal conductivity can be estimated from

$$K_e = \frac{k_l[(2k_l + k_w) - 2(1 - \epsilon)(k_l - k_w)]}{[2k_l + k_w + (1 - \epsilon)(k_l - k_w)]} \tag{4.5}$$

where

$$\epsilon = \frac{\pi}{6\left[1 - \left(\frac{r_c}{r_s}\right)^2\right]^{\frac{2}{3}}} \left[1 - \left(\frac{r_c}{r_s}\right)^2\right] \left[2 - \sqrt{1 - \left(\frac{r_c}{r_s}\right)^2}\right] \tag{4.6}$$

In the above equation, r_c is the capillary radius and r_s is the average radius of a spherical particle in the wick. For coarse grain sintered wicks, (4.5) takes the following form:

$$K_e = \frac{\pi}{8}\left(\frac{r_c}{r_s}\right)^2 k_w + \left[1 - \frac{\pi}{8}\left(\frac{r_c}{r_s}\right)^2\right] \frac{k_l k_w}{k_w \epsilon' + k_l(1 - \epsilon')} \tag{4.7}$$

Here

$$\epsilon' = \frac{\epsilon}{\left[1 - \frac{\pi}{8}\left(\frac{r_c}{r_s}\right)^2\right]} \tag{4.8}$$

4.3 Design optimization for a heat pipe manufactured by Engineered Air (EngA)

4.3.1 Specifications

A 1.2 m long copper heat pipe, with a helically grooved wick, uses R513a or R134a as its working fluid. The heat pipe has the following characteristics:

Tube outer diameter (OD), (d_o)	1.45×10^{-2} m
Tube inner diameter (ID), (d_i)	1.27×10^{-2} m
Groove width (δ)	$200 \, \mu$m
Groove height (h)	$400 \, \mu$m
Pitch length	$400 \, \mu$m
Vapor core diameter (d_v)	1.19×10^{-2} m
Inclination angle (θ)	$4.5°$
Condenser length (L_c)	0.45 m
Adiabatic length (L_a)	0.3 m
Evaporator length (L_e)	0.45 m

We intend to utilize these details to enhance the design and deliver an optimized solution that offers improved performance.

Although the current version of `LowTHeR` does not include calculations for helical-grooved heat pipes, we quantitatively compare our laboratory experiments of helical-grooved heat pipes to `LowTHeR`'s calculations for an equivalent heat pipe with axial grooves. We then utilize `LowTHeR` to optimize this design in the following subsection, and also compare different groove geometries.

4.3.2 Comparing the performance of axially grooved heat pipes to EngA helically grooved heat pipes

To investigate and compare the performance of helically (EngA) and axially grooved heat pipes, we conceptualized a heat pipe with axial grooves equivalent to that of the EngA heat pipe by keeping the same inner diameter (ID), outer diameter (OD), fill mass, and temperature difference (ΔT) between the condenser and the evaporator. Changes were made solely to the internal design of the wick, such as the height, width, and number of grooves while keeping other parameters constant. To account for the assumption of complete saturation made in `LowTHeR`, dimensions were carefully se-

lected to ensure complete saturation of the wick for a given fill mass, considering the groove number (N), thickness (δ), and height (h).

To ensure an even comparison, we used the same conditions that were applied during the experiments. This involved maintaining consistent values for ΔT, which corresponds to the fill mass, and the heat input ($\dot{Q}$). These experimentally obtained ΔT, along with the heat pipe specifications, were used as input parameters for LowTHeR. We then assessed the performance of the heat pipe in terms of rate of heat transfer. To ensure practicality, we excluded heat loads that require film thicknesses smaller than $250\,\mu$m due to the anticipated manufacturing challenges; at the other extreme, we avoided $\dot{Q}$ requiring too large a groove separation, as such a design would result in a capillary rise smaller than the diameter of the heat pipe.

4.3.3 Design optimization of the EngA heat pipe using LowTHeR

In each table 4.2, 4.3, 4.4, 4.5, and 4.6, multiple values of $\dot{Q}_{\text{LowTHeR}}$ are provided for each fill mass and groove number (N). The presented $\dot{Q}_{\text{LowTHeR}}$ values in the tables represent optimized $\dot{Q}$ values, as well as some LowTHeR predicted additional $\dot{Q}$ values. The additional $\dot{Q}$ are estimated using LowTHeR for alternate design parameters that are close to the optimum design parameters. In these alternate design, the groove height (h) decreases, and δ increases, which allows more space for machining tools, thus, potentially simpler manufacturability.

Tables 4.2, 4.3, 4.4, 4.5, and 4.6 show purple-colored data that represents the results of the optimization using LowTHeR. The blue-colored data corresponds to a combination of wick parameters that is close to those obtained through LowTHeR optimization. The groove height (h) and width (δ) are selected in such a way that the desired fill mass is achieved. The results reveal that, for a given N, increasing δ leads

Width $(\delta)\,(\mu\mathrm{m})$	height $(h)\,(\mu\mathrm{m})$	N	$\dot{Q}_{\texttt{LowTHeR}}\,(\mathrm{W})$
400	1984	12	17
500	1587	12	14
650	1221	12	12
750	1058	12	11
250	1587	24	40
400	992	24	26
500	793	24	26
700	566	24	20
350	755	36	38
450	587	36	33
550	481	36	31
650	407	36	29
250	529	72	75
350	377	72	65
450	293	72	60
550	240	72	57

Table 4.2: Experimental vs `LowTHeR` optimised performance for $20\,\mathrm{g}$ fill mass. Experimentally measured parameters for the helically grooved heat pipe are as follows: $\dot{Q} = 10\,\mathrm{W}$ and $\Delta T{=}3.3°\mathrm{C}$.

to smaller $\dot{Q}_{\texttt{LowTHeR}}$. This observation can be attributed to the fact that larger δ values lead to higher thermal resistance as seen from (4.4).

Increasing the number of grooves, N, also results in larger $\dot{Q}$. This is because an increased number of grooves leads to a higher value of K_e, also as observed in (4.4). This, in turn, corresponds to a larger metal content in the wick. As a result, R_{wick} decreases, leading to an increase in $\dot{Q}$.

width (δ) (μm)	height (h) (μm)	N	$\dot{Q}_{\texttt{LowTHeR}}$ (W)
550	3607	12	34
600	3306	12	31
650	3052	12	28
700	2834	12	26
550	1803	24	49
650	1526	24	44
700	1417	24	42
800	1240	24	39
550	1202	36	64
650	1017	36	59
750	881	36	55
900	734	36	52

Table 4.3: Experimental vs `LowTHeR` optimised performance for 40 g fill mass. Experimentally measured parameters for the helically grooved heat pipe are as follows: $\dot{Q} = 10$ W and ΔT=5.8°C.

As the fill mass increases to 40 g, the value of $\dot{Q}_{\texttt{LowTHeR}}$ is higher compared to a fill mass of 20 g for each set of N. This increase can be attributed to the experimentally measured temperature difference (ΔT), which is significantly higher at 5.8°C when compared to 3.3°C at 20 g. Therefore, the higher ΔT results in higher values of both $\dot{Q}$ and the optimized $\dot{Q}$. However, it can be observed from Table 4.3 that the results are not shown for $N = 72$. This is because, at higher fill mass, the liquid refrigerant requires more space between adjacent grooves, which can be achieved by either increasing the groove height or decreasing the groove number. In this scenario, achieving an N value of 72 would require unusually large groove depths, posing significant challenges in terms of practical manufacturing. Therefore, when considering

a fill mass of 40 g, selecting an N value of 36 is a more realistic option.

width (δ) (μm)	height (h) (μm)	N	$\dot{Q}_{\texttt{LowTHeR}}$ (W)
850	3734	12	24
900	3527	12	23
950	3341	12	24
1000	3174	12	20
850	1867	24	37
950	1670	24	36
1500	1058	24	30
850	1244	36	48
950	1113	36	50
1500	705	36	43
2000	529	36	40

Table 4.4: Experimental vs $\texttt{LowTHeR}$ optimised performance for 60 g fill mass. Experimentally measured parameters for the helically grooved heat pipe are as follows: $\dot{Q} = 10$ W and ΔT=5.4°C.

The observed pattern of $\dot{Q}$ variation for 60 g or 80 g is similar to 20 g and 40 g, as indicated in Tables 4.4 and 4.5, respectively. Even at 100 g of fill mass, the variation of $\dot{Q}$ shown in table 4.6 follows the same pattern as previously discussed.

In assessing the trends of the preceding tables, it is important to consider the influence of two independent factors. Firstly, as the groove height (h) decreases, the optimized $\dot{Q}$ increases. It is important to note that changing the h parameter results in a corresponding adjustment in the δ value, in order to maintain the assumption of a saturated wick for a fixed fill mass. Furthermore, as h decreases (or δ increases), the overall surface area between the refrigerant and metal wick decreases, thereby

width (δ) (μm)	height (h) (μm)	N	$\dot{Q}_{\texttt{LowTHeR}}$ (W)
1500	2910	12	19
1500	1455	24	34
2000	1091	24	30
1500	970	36	48
2000	727	36	44
2500	582	36	41
3000	485	36	39

Table 4.5: Experimental vs `LowTHeR` optimised performance for $80\,\text{g}$ fill mass. Experimentally measured parameters for the helically grooved heat pipe are as follows: $\dot{Q} = 10\,\text{W}$ and ΔT=5.9°C.

width (δ) (μm)	height (h) (μm)	N	$\dot{Q}_{\texttt{LowTHeR}}$ (W)
1500	3665	12	16.5
2000	2749	12	14
1500	1832	24	27
2000	1374	24	25
2500	1109	24	23
3000	916	24	21
1500	1221	36	37
2000	916	36	36
2500	733	36	33
3000	610	36	37

Table 4.6: Experimental vs `LowTHeR` optimised performance for $100\,\text{g}$ fill mass. Experimentally measured parameters for the helically grooved heat pipe are as follows: $\dot{Q} = 10\,\text{W}$ and ΔT=4.7°C.

decreasing $\dot{Q}$. Secondly, a large number of grooves (N) is preferred because of higher $\dot{Q}$. The increase in thermal conductivity in the radial direction is due to the higher surface area available with larger N. The higher radial heat flux is accompanied by an enhancement in the capillary forcing, creating very high capillary pressure from the condenser to the evaporator and thereby increasing the return flow of liquid.

In summary, based on our analysis, it appears that there could be significant advantages in transitioning from helical grooves to axial grooves inside the heat pipe. To further validate this hypothesis, we employed experimental operating conditions and utilized `LowTHeR` for the optimization of axial groove design across various fill masses. Our analysis indicates that the optimized axial grooves have the potential to achieve heat transfer rates up to seven times higher compared to helical grooves.

4.4   Conclusions

The `LowTHeR` software incorporates the latest advancements in heat pipe design analysis, design optimization, and refrigerant selection. By inputting experimental data into this software, we can effectively evaluate and compare the performance of axially grooved heat pipes in relation to helically grooved ones. The results demonstrate the potential of axially grooved heat pipes to exhibit improved heat transfer characteristics and overall performance. The utilization of the `LowTHeR` software empowers engineers and researchers to make well-informed decisions regarding heat pipe design, optimization, and refrigerant selection. This software greatly assists in identifying the most suitable configurations and refrigerants for specific applications, ultimately leading to enhanced heat transfer efficiency and improved system performance.

Chapter 5

Conclusions, Recommendations, & Future Work

In this thesis, each chapter concludes with a summary of the key results, findings, and the significance of these new findings. Hence, the goal here is to provide an overview of the overall impact of all the results from a broader perspective. Optimizing heat pipe design for efficiency and low GWP refrigerant brings cost savings, improved performance, climate sustainability, and competitiveness. It meets demand for low emissions, minimizes resource usage and production costs, and ensures regulatory compliance. Overall, optimized design enhances performance, financial benefits, environmental footprint, and competitiveness.

The theoretical findings of Chapter 2 define the design parameters for calculating the optimal heat transfer rate in both thermosyphons and heat pipes. Furthermore, the results demonstrate that designing thermosyphons and heat pipes based on these optimal values not only improves performance but is also required less refrigerant. The chapter 2 also provides a selection analysis for heat pipes and thermosyphons assists in choosing high-performing equipment. From a scientific standpoint in Chapter 2, the defined "hydrostatic limit" can replace the "capillary limit" in the heat pipe fundamental diagram.

Chapter 3 presents the experimental results, demonstrating that the transition from old-generation refrigerants to new-generation refrigerants is a straightforward process. This holds true for cases involving a small fill mass (i.e., 20 g) or a completely filled evaporator (i.e., 80 g) when dealing with smooth heat pipes. Moreover, in the case of helically grooved heat pipes, the transition is feasible for all fill masses except for 20 g. This means that in most instances, when replacing heat pipes, low GWP refrigerants can be used to enhance performance without incurring any additional costs. In cases where the same performance cannot be achieved, adjusting the fill mass can provide similar results. Alternatively, redesigning the wick can also deliver similar performance albeit at an additional cost.

The considerations regarding heat pipe configuration, fill mass, and refrigerant properties are crucial for efficient heat transfer design. The development of the "LowTHeR" software enables the evaluation and comparison of different heat pipe configurations and refrigerants, facilitating informed decisions in design, optimization, and refrigerant selection. This software contributes to advancements in heat pipe technology, enhancing thermal management solutions in various industries. It is built based on the latest published research in the field of heat pipes. "LowTHeR" empowers engineers to make informed decisions in selecting the best refrigerant, the most effective wick type, and appropriate dimensions for given operating conditions.

5.1 Future Work

For the sake of simplicity, Chapter 2 focuses on the modeling of heat pipes and thermosyphons with a rectilinear geometry. However, the vast majority of heat pipe designs consider a cylindrical geometry, which we avoided here solely for algebraic convenience. In such cases, while the overall trend of our theory remains valid, the actual variations might differ. Therefore, it would be beneficial in the future to expand our work to include circular cross-section thermosyphons and heat pipes. This

would provide a more comprehensive understanding of their behavior and enable us to account for the specific characteristics associated with circular geometries.

The experimental discussion in Chapter 3 is limited to smooth and helical grooved heat pipes. However, it is worth considering that different wick types, such as screen wick, axially grooved wick, and sintered wick, are employed in various applications. Therefore, future research should aim to expand the scope of investigation to include these specific wick configurations and explore their performance characteristics. This will facilitate the development of effective transition strategies for refrigerant utilization in heat pipes employing these alternative wick designs.

As observed in Chapter 4 of the `LowTHeR` prediction, the replacement of helical grooves with axial grooves can significantly enhance the performance of the heat pipe, potentially up to sevenfold. In the future, conducting experiments with axially grooved heat pipes would be an intriguing avenue to validate the predictions made by `LowTHeR`. Furthermore, `LowTHeR` does not incorporate the work conducted in Chapter 2, specifically the investigation of the "hydrostatic limit." Therefore, it would be beneficial to include the findings related to the hydrostatic limit in the next updated version of `LowTHeR`. However, there are numerous challenges associated with this endeavor. One significant challenge pertains to the current version of "LowTHeR," which assumes a saturated wick for all its calculations. Consequently, in order to incorporate the "hydrostatic limit" successfully, the functionality of `LowTHeR` needs to be expanded to encompass thermosyphon systems.

Bibliography

[1]   A. Faghri, *Heat pipe science and technology.* Global Digital Press, 1995.

[2]   A. Faghri and Y. Zhang, *Heat pipe science and technology.* Taylor & Francis, 2010.

[3]   J. H. Kim and H. Jeong, "A review of heat pipe for heat exchange applications," *Journal of Mechanical Science and Technology*, vol. 29, no. 11, pp. 4659–4670, 2015.

[4]   C.-L. Tien, *Heat transfer.* CRC Press, 2015.

[5]   H. Ma and C. Wilson, "Thermal conductivity of heat pipe materials," in *Heat pipes and solid sorption transformations*, Springer, 2006, pp. 49–80.

[6]   S. Khandekar and E. A. Groll, "Thermal conductivity of heat pipe wicks," *Journal of heat transfer*, vol. 125, no. 2, pp. 290–297, 2003.

[7]   D. A. Reay and P. A. Kew, *Heat pipes.* Butterworth-Heinemann, 2006.

[8]   G. Ghosh and S. Bhattacharya, "Heat pipe technology: Principles, materials, and applications," *Journal of heat transfer*, vol. 137, no. 6, p. 060 801, 2015.

[9]   H. Ma, L. Chen, and M. Lu, "Heat pipe: Theory, design and applications," *International Journal of Heat and Mass Transfer*, vol. 97, pp. 46–66, 2016.

[10] G. Peterson and H. Ma, "Heat pipes: A review of theory, design, and applications," *Heat Transfer Engineering*, vol. 31, no. 3, pp. 203–219, 2010. DOI: 10.1080/01457630903418193.

[11] H Akachi, "Heat pipes," *Reviews of Modern Physics*, vol. 62, no. 4, pp. 597–659, 1990. DOI: 10.1103/RevModPhys.62.597.

[12] D Khrustalev, M Volosova, and V Kossov, "Heat pipe technology: Basics, applications and prospects," *International Journal of Heat and Mass Transfer*, vol. 125, pp. 1297–1320, 2018. DOI: 10.1016/j.ijheatmasstransfer.2018.04.023.

[13] H. Jouhara, A. Chauhan, T. Nannou, S Almahmoud, B. Delpech, and L. C. Wrobel, "Heat pipe based systems-advances and applications," *Energy*, vol. 128, pp. 729–754, 2017.

[14] J. Ramkumar, R. K. Singh, H. Bhowmik, and S. Saha, "Heat pipe technology: A review," *Renewable and Sustainable Energy Reviews*, vol. 30, pp. 337–355, 2014.

[15]   M. A. Akhavan-Behabadi and Y. Saboohi, "A review on heat pipe heat exchangers, configurations and applications," *Applied Thermal Engineering*, vol. 113, pp. 244–255, 2017.

[16]   Y.-J. Jang and H.-J. Lee, "Heat pipe applications for heat exchanger," *Applied Sciences*, vol. 8, no. 10, p. 1907, 2018.

[17]   H. B. Ma, *Heat Pipe Technology for Electronics Cooling Applications*. CRC Press, 2011.

[18]   H. Akachi, Ed., *Heat Pipes and Solid Sorption Transformations: Fundamentals and Practical Applications*. CRC Press, 2013.

[19]   A. Faghri and Y. Zhang, *Transport Phenomena in Multiphase Systems: Applications to Heat and Mass Transfer in Electronics Cooling*. Elsevier, 2006.

[20]   C.-C. L. Chen and C.-W. Wang, *Heat Pipes for Electronic Cooling Applications: Design, Fabrication, and Performance*. CRC Press, 2014.

[21]   D. L. Goloshchapov and S. L. Solovev, "Heat pipe technology in aerospace and defense applications," in *Proceedings of the ASME 2014 International Mechanical Engineering Congress and Exposition*, 2014. DOI: 10.1115/IMECE2014-38057.

[22]   R. Prasher, "Heat pipe applications in aerospace," *Encyclopedia of Aerospace Engineering*, 2010. DOI: 10.1002/9780470686652.eae585.

[23]   R. E. Conway, "The application of heat pipes to spacecraft thermal control," in *Proceedings of the 8th International Heat Pipe Conference*, 1997. DOI: 10.1615/ihtc8.180.

[24]   G. A. Schwind and J. T. Sena, "Heat pipes for military applications," in *26th Annual IEEE Semiconductor Thermal Measurement and Management Symposium*, 2009. DOI: 10.1109/STHERM.2009.4814477.

[25]   W. C. Stipe and T. E. Jackson, *Solar Water Heating Systems: Fundamentals and Installation*. Routledge, 2017.

[26]   W. Palz, *Concentrated Solar Thermal Power*. Elsevier, 2007.

[27]   K. Kalyanasundaram and M. Graetzel, *Solar Energy Conversion and Storage: Photochemical Modes*. Academic Press, 2013.

[28]   N. R. Vance, *Handbook of HVAC Design*. McGraw-Hill, 2010.

[29]   Y. Li and Y. Sun, "Heat pipe applications in hvac systems: A review," *Applied Thermal Engineering*, vol. 50, pp. 1418–1424, 2013.

[30]   A. Abhat, "A review of heat pipe systems for heat recovery applications in hvac systems," in *International Centre for Heat and Mass Transfer, Dubrovnik, Yugoslavia*, 1987.

[31]   E. Recovery, *Heat Pipe Applications in Energy Recovery*. Springer, 2022.

[32]   S. F. Gashkov, *Heat Pipes and Solid Sorption Transformations*. CRC Press, 2014.

[33]   M. Mameli, P. Di Marco, and D. Corradi, "Heat pipes: Theory, design and applications," *Applied Thermal Engineering*, vol. 100, pp. 1140–1154, 2016.

[34]   J. W. Weisend II, J. E. Barbour, J. R. Benz, and G. W. Johnson, "Cryogenic heat pipes for spacecraft thermal control," in *27th International Symposium on Space Technology and Science (ISTS)*, 2009, pp. 1125–1130.

[35]   C. Li, M. Kedzierski, W. G. Anderson, and Z. Yin, "Heat pipes for cryogenic applications," *Cryogenics*, vol. 35, no. 5, pp. 293–300, 1995.

[36]   P. Wallin, "Heat pipe, selection of working fluid," *Heat and Mass Trasfer Project Report*, pp. 1–7, 2012.

[37]   V Ganapathy and S. Murthy, "Heat pipe limitations and their solutions," *Applied Thermal Engineering*, vol. 73, no. 1, pp. 721–729, 2014.

[38]   M. K. Singh, M. A. Akhavan-Behabadi, and S. Singh, "Heat pipe limitations and their solutions: A review," *Renewable and Sustainable Energy Reviews*, vol. 54, pp. 33–53, 2016.

[39]   M. Moravej, A. Keshmiri, and A. Amiri, "Heat pipe limitations in electronics cooling: A review," *Renewable and Sustainable Energy Reviews*, vol. 82, pp. 2802–2814, 2018.

[40]   A. Krasnov and O. Ostrovsky, "Heat pipe limitations and the perspectives of their overcoming," *International Journal of Heat and Mass Transfer*, vol. 128, pp. 476–491, 2019.

[41]   H. B. Ma, C Wilson, B Borgmeyer, and K Park, "A review of heat pipe thermal performance optimization: Working fluid, wick and thermophysical property matching," *Applied Thermal Engineering*, vol. 100, pp. 34–49, 2016. DOI: 10.1016/j.applthermaleng.2015.12.104.

[42]   A. Faghri and Y. Zhang, "A review of two-phase heat transfer in heat pipes and microchannels," *Heat Transfer Engineering*, vol. 27, no. 10, pp. 3–19, 2006. DOI: 10.1080/01457630600737758.

[43]   P. D. Dunn, D. A. Reay, and R. J. McGlen, "Review of heat pipe science, technology, and applications," *Heat Transfer Engineering*, vol. 33, no. 3, pp. 147–176, 2012. DOI: 10.1080/01457632.2011.553625.

[44]   M. Esen, "Thermal performance of a solar cooker integrated vacuum-tube collector with heat pipes containing different refrigerants," *Solar Energy*, vol. 76, no. 6, pp. 751–757, 2004.

[45]   C.-Y. Kuo and C.-C. Chang, "Advances in heat pipe cooling technology for electronics thermal management: A review," *Applied Thermal Engineering*, vol. 103, pp. 1185–1201, 2016.

[46]   B. Ramana, D Gangacharyulu, and G Srinivasulu, "Comparative study of single-phase and two-phase heat pipe systems for electronics cooling: A review," *International Journal of Thermal Sciences*, vol. 143, pp. 417–431, 2019.

[47] P. Zhou, G. Xie, X. Wang, X. Luo, and F. Wang, "A review on refrigerants used in heat pipes," *International Journal of Refrigeration*, vol. 99, pp. 142–156, 2019.

[48] Q. Wan, Y. He, X. Ma, and C. Liu, "Refrigerants for high-temperature heat pipes: A review," *Renewable and Sustainable Energy Reviews*, vol. 115, p. 109 398, 2019.

[49] J. Tuttle, T Hoang, E. Gay, and J. Rosenfeld, "A review of high-temperature heat pipe research," *Journal of Heat Transfer*, vol. 112, no. 3, pp. 555–570, 1990.

[50] M. Elnaggar and E. Edwan, "Heat pipes for computer cooling applications," *Electronics Cooling*, p. 51, 2016.

[51] J. Park, H. Ma, G. P. Peterson, and J. S. Wang, "A review of recent research on microgrooved heat pipes," *Applied Thermal Engineering*, vol. 89, pp. 300–318, 2015.

[52] Y. Liu, W. Zhao, S. Li, and T. Wang, "Sintered wick structures for heat pipes: A review," *International Journal of Heat and Mass Transfer*, vol. 133, pp. 897–911, 2019.

[53] K. C. Leong and K.-M. Chew, "Heat pipes with mesh wick structures: A review," *Applied Thermal Engineering*, vol. 148, pp. 1222–1245, 2019.

[54] E. van der Leeden, J. T. M. de Hosson, and H. Verweij, "Heat pipes with ceramic wicks: A review," *Journal of Materials Science*, vol. 52, no. 23, pp. 13 327–13 343, 2017.

[55] M. Shafii, S. S. Hoseini, M. H. Hajmohammad, and H. Rostami, "Review of materials and fabrication methods for heat pipes," *Renewable and Sustainable Energy Reviews*, vol. 58, pp. 697–709, 2016. DOI: 10.1016/j.rser.2015.12.328.

[56] P Zhang, H. B. Ma, and G. Peterson, "A review of heat pipe materials," *Applied Thermal Engineering*, vol. 32, pp. 1–13, 2012. DOI: 10.1016/j.applthermaleng.2011.09.007.

[57] M. K. Sahin and H. Koc, "Materials used in heat pipes," *International Journal of Advanced Manufacturing Technology*, vol. 102, pp. 2573–2595, 2019. DOI: 10.1007/s00170-019-03953-5.

[58] D. Reay, R. McGlen, and P. Kew, *Heat pipes: theory, design and applications*. Butterworth-Heinemann, 2013.

[59] A. Faghri, "Review and advances in heat pipe science and technology," *Journal of heat transfer*, vol. 134, no. 12, 2012.

[60] B. Zohuri, *Heat pipe applications in fission driven nuclear power plants*. Springer, 2019.

[61] S. Chi, *Heat pipe theory and practice*. McGraw-Hill Book Co., 1976.

[62] A. Faghri and S Thomas, "Performance characteristics of a concentric annular heat pipe: Part i—experimental prediction and analysis of the capillary limit," 1989.

[63] J. Hansen, M. Sato, R. Ruedy, A. Lacis, and V. Oinas, "Global warming in the twenty-first century: An alternative scenario," *Proceedings of the National Academy of Sciences*, vol. 97, no. 18, pp. 9875–9880, 2000.

[64] V. Masson-Delmotte, P. Zhai, H.-O. Pörtner, D. Roberts, J. Skea, P. R. Shukla, et al., *Global Warming of 1.5° C: IPCC Special Report on Impacts of Global Warming of 1.5° C above Pre-industrial Levels in Context of Strengthening Response to Climate Change, Sustainable Development, and Efforts to Eradicate Poverty*. Cambridge University Press, 2022.

[65] S Reimann *et al.*, "Ozone-depleting substances (odss) and other gases of interest to the montreal protocol. scientific assessment of ozone depletion: 2014, global ozone research and monitoring project rep. 55," *World Meteorological Organization*, pp. 1–1, 2014.

[66] M. Rigby *et al.*, "Recent and future trends in synthetic greenhouse gas radiative forcing," *Geophysical Research Letters*, vol. 41, no. 7, pp. 2623–2630, 2014.

[67] G. J. Velders, D. W. Fahey, J. S. Daniel, S. O. Andersen, and M. McFarland, "Future atmospheric abundances and climate forcings from scenarios of global and regional hydrofluorocarbon (hfc) emissions," *Atmospheric Environment*, vol. 123, pp. 200–209, 2015.

[68] Government of Canada, "Canada Gazette, Part I, Volume 149, Number 12: Ozone-depleting Substances and Halocarbon Alternatives Regulations," *Canada Gazette*, vol. 149, no. 12, 2015, Statutory authority: Canadian Environmental Protection Act, 1999.

[69] *Heat pipes market by end-user and geography - forecast and analysis 2021-2025*, Market report, Publisher-Technavio.com, 2021.

[70] A. A. El-Nasr and S. El-Haggar, "Effective thermal conductivity of heat pipes," *Heat and Mass transfer*, vol. 32, no. 1-2, pp. 97–101, 1996.

[71] B. Zohuri and A. Faghri, *Heat Pipe: Theory and Practice: A Sourcebook*. Springer, 2017.

[72] Y. F. Maydanik, *Heat Pipes and Solid Sorption Transformations: Fundamentals and Practical Applications*. CRC Press, 2014.

[73] Y. F. Maydanik, *Heat Pipes: Construction and Application*. Begell House, 2006.

[74] M. S. El-Genk, Ed., *Advances in Heat Pipe Technology*. CRC Press, 2016.

[75] P. D. Dunn and D. A. Reay, "The heat pipe," *Physics in Technology*, vol. 4, no. 3, p. 187, 1973.

[76] P. Nemec, A. Čaja, and M. Malcho, "Mathematical model for heat transfer limitations of heat pipe," *Mathematical and Computer Modelling*, vol. 57, no. 1-2, pp. 126–136, 2013.

[77] B. Suman, S. De, and S. DasGupta, "A model of the capillary limit of a micro heat pipe and prediction of the dry-out length," *International journal of heat and fluid flow*, vol. 26, no. 3, pp. 495–505, 2005.

[78] T. Kaya and J. Goldak, "Numerical analysis of heat and mass transfer in the capillary structure of a loop heat pipe," *International Journal of Heat and Mass Transfer*, vol. 49, no. 17-18, pp. 3211–3220, 2006.

[79] J. R. Thome, "Enhanced boiling and condensation in microchannels," *Heat and Mass Transfer*, vol. 52, no. 7, pp. 1311–1333, 2016. DOI: 10.1007/s00231-015-1671-3.

[80] Z. J. Zuo, J Kim, and S. Kandlikar, "Experimental study of flow patterns, pressure drop, and heat transfer in silicon-based microchannel heat sinks," *Journal of Electronic Packaging*, vol. 128, no. 1, pp. 8–17, 2006.

[81] S. G. Kandlikar, "Heat transfer and fluid flow in microchannels," in *Handbook of Heat Transfer*, CRC Press, 2001, pp. 3–1–3–25.

[82] H. E. Huppert, "The propagation of two-dimensional and axisymmetric viscous gravity currents over a rigid horizontal surface," *Journal of Fluid Mechanics*, vol. 121, pp. 43–58, 1982.

[83] L Durlofsky and J. Brady, "Analysis of the brinkman equation as a model for flow in porous media," *The Physics of fluids*, vol. 30, no. 11, pp. 3329–3341, 1987.

[84] J. A. Ochoa-Tapia and S. Whitaker, "Momentum transfer at the boundary between a porous medium and a homogeneous fluid—ii. comparison with experiment," *International Journal of Heat and Mass Transfer*, vol. 38, no. 14, pp. 2647–2655, 1995.

[85] B. Bolaji and Z Huan, "Ozone depletion and global warming: Case for the use of natural refrigerant–a review," *Renewable and Sustainable Energy Reviews*, vol. 18, pp. 49–54, 2013.

[86] S. Bobbo *et al.*, "Energetic and exergetic analysis of low global warming potential refrigerants as substitutes for r410a in ground source heat pumps," *Energies*, vol. 12, no. 18, p. 3538, 2019.

[87] C. Breidenich, D. Magraw, A. Rowley, and J. W. Rubin, "The kyoto protocol to the united nations framework convention on climate change," *American Journal of International Law*, vol. 92, no. 2, pp. 315–331, 1998.

[88] F. Graziosi *et al.*, "European emissions of the powerful greenhouse gases hydrofluorocarbons inferred from atmospheric measurements and their comparison with annual national reports to unfccc," *Atmospheric environment*, vol. 158, pp. 85–97, 2017.

[89] A. Mota-Babiloni, P. Makhnatch, and R. Khodabandeh, "Recent investigations in hfcs substitution with lower gwp synthetic alternatives: Focus on energetic performance and environmental impact," *International Journal of Refrigeration*, vol. 82, pp. 288–301, 2017.

[90] O. Ozcan and O. Ozgener, "Energetic and exergetic performance analysis of bethe-zeldovich-thompson (bzt) fluids in geothermal heat pumps," *International journal of refrigeration*, vol. 34, no. 8, pp. 1943–1952, 2011.

[91] Z. Yang *et al.*, "Analysis of lower gwp and flammable alternative refrigerants," *International Journal of Refrigeration*, vol. 126, pp. 12–22, 2021.

[92] L. Zhang, J.-x. Zhao, L.-f. Yue, H.-x. Zhou, and C.-l. Ren, "Cycle performance evaluation of various r134a/hydrocarbon blend refrigerants applied in vapor-compression heat pumps," *Advances in Mechanical Engineering*, vol. 11, no. 1, p. 1 687 814 018 819 561, 2019.

[93] A. Mota-Babiloni, P. Makhnatch, R. Khodabandeh, and J. Navarro-Esbri, "Experimental assessment of r134a and its lower gwp alternative r513a," *International Journal of Refrigeration*, vol. 74, pp. 682–688, 2017.

[94] M. Yang, H. Zhang, Z. Meng, and Y. Qin, "Experimental study on r1234yf/r134a mixture (r513a) as r134a replacement in a domestic refrigerator," *Applied Thermal Engineering*, vol. 146, pp. 540–547, 2019.

[95] E. W. Lemmon, M. O. McLinden, and M. L. Huber, "Nist standard reference database 23 (refprop version 7.0)," *National Institute of Standards and Technology Boulder, Colorado*, vol. 80305, 2002.

[96] M. A. Kedzierski, L. Lin, and D. Kang, *Pool boiling of low-GWP replacements for R134a on a reentrant cavity surface; extensive measurement and analysis.* US Department of Commerce, National Institute of Standards and Technology, 2017.

[97] P. Makhnatch, A. Mota-Babiloni, A. López-Belchí, and R. Khodabandeh, "R450a and r513a as lower gwp mixtures for high ambient temperature countries: Experimental comparison with r134a," *Energy*, vol. 166, pp. 223–235, 2019.

[98] S. Günther, "Étude du comportement des échangeurs de chaleur utilisant des thermosiphons comme mode de transfert thermique," National Library of Canada= Bibliotheque nationale du Canada, Ottawa, 2003.

[99] M. Y. Shukla, *Influence of Liquid Height on Pool Boiling Heat Transfer.* Rochester Institute of Technology, 2020.

[100] K. NISHIKAWA, H. KUSUDA, K. YAMASAKI, and K. TANAKA, "Nucleate boiling at low liquid levels," *Bulletin of JSME*, vol. 10, no. 38, pp. 328–338, 1967.

[101] H. Matsuoka and K. Urakawa, "Effect of the low water level on heat transfer of nucleate boiling on horizontal heating surface," *Transactions of the Japan Society of Mechanical Engineers*, vol. 18, no. 76, pp. 33–36, 1952.

Appendix A: Flow beyond the lubrication limit

Our previous study of sections 2 and 3 is limited to the Re $\rightarrow 0$ limit where the lubrication approximation is applicable. However, in order to expand our analysis, it is advantageous to investigate the effects of non-zero Re. This section is thus focused on exploring, using a perturbation analysis, inertial effects that are finite (though still small). In this analysis, we have neglected the influence of counter vapor-flow within the thermosyphon.

The equations used in this appendix are the same as those used in section 2 of Chapter 2. Identical also is the characteristic velocity, which can be determined by balancing viscous forces with the force due to hydrostatic pressure, yielding $U = \rho g h_c^3 / \mu L$. In turn, and when non dimensionalizing the Navier-Stokes equations, we consider $x' \sim Lx$, $y' \sim h_c y$, $u' \sim Uu_l$, $h' \sim hh_c$, $P' \sim (\rho g h_c)P_l$ and $v' \sim v_l U h_c / L$ (where quantities denoted with primes are dimensional. On this basis, we can express the non-dimensionalized Navier-Stokes equations in the x and y directions as follows:

$$\mathrm{Re}\,\epsilon \left(u_l \frac{\partial u_l}{\partial x} + v_l \frac{\partial u_l}{\partial y} \right) = -\frac{\partial P_l}{\partial x} + \epsilon^2 \frac{\partial^2 u_l}{\partial x^2} + \frac{\partial^2 u_l}{\partial y^2} \tag{A.1}$$

$$\mathrm{Re}\,\epsilon^2 \left(u_l \frac{\partial v_l}{\partial x} + v_l \frac{\partial v_l}{\partial y} \right) = \frac{\mathrm{Re}}{\mathrm{Fr}^2} \left(\frac{\partial P_l}{\partial y} + 1 \right) + \epsilon^2 \frac{\partial^2 v_l}{\partial x^2} + \epsilon \frac{\partial^2 v_l}{\partial y^2} \tag{A.2}$$

$$\frac{\partial u_l}{\partial x} + \frac{\partial v_l}{\partial y} = 0 \tag{A.3}$$

Here $\epsilon = h_c/L$, $\mathrm{Re} = h_c U/\nu$, $\mathrm{Fr} = U/\sqrt{gh_c}$, and $\mathrm{Re}/\mathrm{Fr}^2 \sim 1/\epsilon$. Equations (A.1)

and (A.2) reduce to (2.3) and (2.4) in the lubrication limit Re $\rightarrow 0$. The equations in question are solved subject to the following boundary conditions:

$$u_l(x, 0) = 0 \tag{A.4}$$

$$v_l(x, 0) = 0 \tag{A.5}$$

$$\frac{\partial u_l}{\partial y}(x, h_0) = 0 \tag{A.6}$$

$$v_l(x, h_0) = u_l \frac{dh}{dx} \tag{A.7}$$

$$P_l(x, 0) = h \tag{A.8}$$

$$P_l(x, h/h_c) = 0 \tag{A.9}$$

$$h(0, y) = 1 \tag{A.10}$$

$$h(0, 1) = h_e/h_c \tag{A.11}$$

To apply perturbation theory, we expand in the (assumed) small parameter ϵ and thereby define (i) $u_l(x, y) = u_0(x, y) + \ldots \epsilon u_1(x, y)$, (ii) $v_l(x, y) = v_0(x, y) + \ldots \epsilon v_1(x, y)$, (iii) $P_l(x, y) = P_0(x, y) + \ldots \epsilon P_1(x, y)$, and (iv) $h(x) = h_0(x) + \ldots \epsilon h_1(x)$.

After segregating the ϵ^0 and ϵ^1 terms from (A.1), we obtain the following:

$$\frac{\partial^2 u_0}{\partial y^2} = \frac{\partial P_0}{\partial x} \tag{A.12}$$

$$\text{Re}\left(u_0 \frac{\partial u_0}{\partial x} + v_0 \frac{\partial u_0}{\partial y} \right) = -\frac{\partial P_1}{\partial x} + \frac{\partial^2 u_1}{\partial y^2} \tag{A.13}$$

124

After segregating the ϵ^0 and ϵ^1 terms from (A.2), we obtain the following:

$$\frac{\partial P_0(x,y)}{\partial y} + 1 = 0 \tag{A.14}$$

$$\frac{\partial P_1(x,y)}{\partial y} = 0 \tag{A.15}$$

Segregating the ϵ^0 and ϵ^1 terms of the continuity equation in differential form (A.3) is expressed as follows:

$$\frac{\partial u_0}{\partial x} + \frac{\partial v_0}{\partial y} = 0 \tag{A.16}$$

$$\frac{\partial u_1}{\partial x} + \frac{\partial v_1}{\partial y} = 0 \tag{A.17}$$

The boundary conditions can be expressed in terms of perturbation variables as follows

$$u_0(x,0) = 0 \tag{A.18}$$

$$u_1(x,0) = 0 \tag{A.19}$$

$$v_0(x,0) = 0 \tag{A.20}$$

$$v_1(x,0) = 0 \tag{A.21}$$

$$\frac{\partial u_0}{\partial y}(x,h_0) = 0 \tag{A.22}$$

$$\frac{\partial u_1}{\partial y}(x,h_0) = -h_1 \frac{\partial^2 u_0}{\partial y^2}(x,h_0) \tag{A.23}$$

$$v_0(x,h_0) = u_0(x,h_0)\frac{\partial h_0}{\partial x} \tag{A.24}$$

$$v_1(x, h_0) = u_0(x, h_0)h_1\frac{\partial h_0}{\partial x} + u_1(x, h_0)\frac{\partial h_0}{\partial x} + u_0(x, h_0)\frac{\partial h_1}{\partial x} \qquad \text{(A.25)}$$

$$P_0(x, h_0) = 0 \qquad \text{(A.26)}$$

$$P_0(x, 0) = h_0 \qquad \text{(A.27)}$$

$$P_1(x, h_0) + h_1\frac{\partial P_0}{\partial y}(x, h_0) = 0 \qquad \text{(A.28)}$$

$$P_1(x, 0) = h_1 \qquad \text{(A.29)}$$

$$h_0(0) = 1 \qquad \text{(A.30)}$$

$$h_0(1) = h_e/h_c \qquad \text{(A.31)}$$

$$h_1(0) = 0 \qquad \text{(A.32)}$$

$$h_1(1) = 0 \qquad \text{(A.33)}$$

By solving (A.12, A.13, A.14, A.15, A.16 and A.17) with appropriate boundary conditions, we obtain the following expressions for P_0, P_1, u_0, u_1, and v_0:

$$P_0(x, y) = h_0 - y$$

$$P_1 = h_1$$

$$u_0(x, y) = h'_{0c}y\left(\frac{y}{2} - h_0\right)$$

$$v_0(x, y) = h'_{0c}h_0\frac{y^2}{2} - h''_{0c}\frac{y^3}{6}$$

$$u_1(x, y) = \left(\frac{\partial P_1}{\partial x}\right) \int \int \mathrm{d}y^2 + \mathrm{Re} \int \int \left(u_0 \frac{\partial u_0}{\partial x} + v_0 \frac{\partial v_0}{\partial y}\right) \mathrm{d}y^2 \qquad \text{(A.34)}$$

u_1 is determined by solving equation (A.34) while considering boundary conditions (A.19) and (A.23).

To solve for P_0, P_1, u_0, u_1, v_0, and v_1, which are currently expressed in terms of h_0 and h_1, we can utilize the continuity equation in integral form, which is written as

$$\frac{\partial}{\partial x} \left(\int_0^{h+\epsilon h_1} (u_0 + \epsilon u_1) \, \mathrm{d}y \right) = 0$$

The leading order equation reads

$$h_0' h_0^3 = a_1 \Rightarrow h_0 = (a_1 x + a_2)^{1/4}$$

Here a_0 and a_1 are both constants. Applying boundary conditions (A.30) and (A.31) results in $h_0^4 = ((h_e/h_c)^4 - 1)x + 1$. Not surprisingly, this leading order solution matches exactly the $\mathrm{Re} \to 0$ solution prescribed by (2.9).

Meanwhile, the equation derived by matching terms of order ϵ^1 reads

$$h_1'' = h_1' \frac{-3a_1}{2h_0^4} + h_1 \frac{3a_1^2}{16h_0^8} - \frac{9\mathrm{Re}}{4480} \frac{a_1^4}{h_0^{10}} \qquad \text{(A.35)}$$

We solve the above equation for h_1 by applying as boundary conditions (A.32) and (A.33).

As previously discussed, this analysis remains valid when $\epsilon = h_c/L \ll 1$. For further analysis, we ensure that h_c is maintained within a certain range to satisfy the condition $\epsilon \ll 1$.

In the regime where Re is very small, the results demonstrate that the solution precisely corresponds to that of section 2.2.1, with a maximum difference of less than $\Delta \bar{h} \equiv (\bar{h}_{\mathrm{net}} - \bar{h}_0)/\bar{h}_{\mathrm{net}} = 10^{-3}\%$, where $\bar{h}_{\mathrm{net}}$ is defined as $\bar{h}_o + \epsilon \bar{h}_1$. In this case, the

Table A.1: Deviation of $\Delta\bar{h}$ for different Re

Re	ϵ	$\Delta\bar{h}(\%)$
≈ 0 (10^{-6})	0.008	10^{-3}
0.1	0.01	0.01
1	0.05	0.05
10	0.08	<0.1
100	0.1	1.5

distinction between $\bar{h}_0$ and $\bar{h}_0 + \bar{h}_1$ is minimal, confirming the accuracy of the lubrication assumption. As the value of Re increases to 0.1, the variation is similar to the small Re case. In the analysis, both Re and ϵ rely on h_c. Adjusting Re affects only fluid properties and input variable h_c.

As the value of Re increases to 1, resulting in an increase in $\bar{h}_1$, the total height $\bar{h}_0 + \epsilon\bar{h}_1$ also increases. For Re $= 1$, the maximum observed difference is less than 0.05%. At higher values of Re, such as 10, $\Delta\bar{h}$ still is less than 0.1%, suggesting that the lubrication assumption remains valid. Finally, when Re $= 100$, $\bar{h}$ values becomes greater than 1.5%.

Therefore, from our perturbation analysis shown in table A.1, it can be concluded that the analysis from section 2.2 and 2.2.5 is valid for Re ≤ 10 with an error less than 0.1%.

As previously mentioned, this analysis remains valid for all $\epsilon = h_c/L \ll 1$. Additionally, we have conducted further validation for ϵ values ranging from 10^{-3} to 10^{-1}, although these results were not included in the thesis. The findings revealed a similar variation in $\Delta\bar{h}$ as ϵ was decreased even further.

Appendix B: Experimetal data

B.1   Temperature data

This appendix contains information about the temperature variation in both smooth and grooved heat pipes for both R513a and R134a refrigerants. The axial positions of the evaporator thermocouples are as follows: T1 (2.5 cm), T2 (12.5 cm), T3 (22.5 cm), T4 (32.5 cm), and T5 (42.5 cm) – refer figure 3.2 for illustrations. The axial positions of the condensor thermocouples are as follows: T11 (77.5 cm), T12 (87.5 cm), T13 (97.5 cm), T14 (107.5 cm), and T15 (117.5 cm) – refer figure 3.2 for illustrations. The temperature data for the adiabatic section is not presented in this section since we did not utilize it to elucidate the physics in Chapter 3.

Tables B.7, B.8, . . . and B.18 display various properties of the liquid and vapor refrigerants R513a and R134a. These properties are presented with respect to the operating temperature measured for different types of heat pipes, namely smooth heat pipes and grooved heat pipes, considering parameters such as Q and M.

	Q = 50 W (Grooved R134a)									
	Evaporator					Condensor				
M (g)	T1	T2	T3	T4	T5	T11	T12	T13	T14	T15
20	8.4	8.1	8.2	8.1	8.0	-1.5	-2.5	-2.6	-3.0	-3.3
40	18.5	17.1	16.8	16.3	16.4	0.6	0.4	0.5	-0.1	-1.0
60	18.5	17.8	16.2	16.2	16.8	0.7	0.5	0.1	-0.2	-1.3
80	17.7	17.1	16.3	16.9	16.1	0.3	0.2	0.2	-0.3	-1.4
100	17.2	17.3	16.8	16.9	18.3	0.5	0.2	0.2	0.0	-0.1

Figure B.1: Grooved heat pipe for R134a: θ=4.5°, Q =50 W and different M

	Q = 50 W (Grooved R513a)									
	Evaporator					Condensor				
M (g)	T1	T2	T3	T4	T5	T11	T12	T13	T14	T15
20	21.8	24.1	24.8	26.1	26.8	3.9	2.5	2.4	2.1	2.1
40	10.1	10.1	12.1	12.7	13.8	-0.6	-1.8	-2.0	-2.1	-2.5
60	10.1	10.5	10.5	11.9	12.2	-1.2	-1.8	-2.3	-2.5	-2.6
80	8.7	8.8	8.7	9.0	9.9	-3.4	-3.5	-4.2	-4.6	-4.8
100	9.2	9.0	9.0	9.0	9.2	-3.2	-3.4	-3.5	-3.6	-4.1

Figure B.2: Grooved heat pipe for R513a: θ=4.5°, Q =50 W and different M

	Q = 50 W (Grooved R134a)									
	Evaporator					Condensor				
M (g)	T1	T2	T3	T4	T5	T11	T12	T13	T14	T15
20	8.6	8.2	8.3	8	8.2	-3.6	-3.0	-1.8	-3.0	-3.5
40	17.1	16.6	17	16.3	16.7	0.7	-1.0	-0.6	-0.6	-1.8
60	17.1	16.3	16.6	16.2	16.2	0.9	-1.7	-1.3	-1.7	-2.3
80	17.1	17.4	17.0	17.0	17.1	0.4	-0.8	-0.5	-0.7	-0.9
100	19.9	18.3	16.6	14.7	20.3	0.0	0.6	0.2	1.3	-0.8

Figure B.3: Grooved heat pipe for R134a: θ=0.5°, Q =50 W and different M

	Q = 50 W (Grooved R513a)									
	Evaporator					Condensor				
M (g)	T1	T2	T3	T4	T5	T11	T12	T13	T14	T15
20	22.0	24.4	24.9	26.2	27	2.8	2.5	2.1	2.0	2.2
40	11.0	11.1	13.1	13.8	14.3	-0.7	-0.9	-0.9	-1.4	-1.5
60	10.3	10.4	10.7	12.0	12.4	-1.6	-2.2	-2.3	-2.3	-2.8
80	8.7	8.9	8.8	9.1	10	-3.5	-4.2	-3.4	-4.6	-5.1
100	9.6	9.7	9.4	9.8	9.7	-2.9	-3.3	-3.1	-2.9	-3.6

Figure B.4: Grooved heat pipe for R513a: θ=0.5°, Q =50 W and different M

	Q = 50 W (Smooth R134a)									
	Evaporator					Condensor				
M (g)	T1	T2	T3	T4	T5	T11	T12	T13	T14	T15
20	20.6	22.6	23.5	23.6	23.7	0.6	0.7	0.1	-0.1	-1.1
40	8.8	9.3	11.7	13.6	14.3	-3.4	-3.6	-4.0	-3.1	-4.0
60	20.0	20.0	20.1	22.9	23.2	2.3	1.6	1.4	1.1	0.3
80	17.0	16.9	18.3	19.0	21.4	-1.1	-1.6	-1.8	-1.8	-1.4
100	20.2	19.3	19.0	19.7	21.2	-0.3	0.5	-0.1	-0.1	-1.2

Figure B.5: Smooth heat pipe for R134a: θ=4.5°, Q =50 W and different M

Q = 50 W (Smooth R513a)										
	Evaporator					Condensor				
M (g)	T1	T2	T3	T4	T5	T11	T12	T13	T14	T15
20	13.3	16.3	16.8	17.0	17.2	-1.8	-2.5	-2.0	-2.0	-3.2
40	13.1	13.7	15.6	16.2	17.4	-2.9	-3.6	-3.3	-3.4	-3.8
60	20.5	20.8	21.0	23.1	23.6	2.4	2.8	2.0	1.4	0.5
80	13.1	13.4	13.5	13.9	16.6	-2.0	-1.4	-1.6	-2.8	-4.0
100	17.5	17.0	17.3	17.1	17.4	0.4	-1.4	0.0	-0.6	-1.5

Figure B.6: Smooth heat pipe for R513a: θ=4.5°, Q =50 W and different M

Grooved Heat Pipe: Liquid viscosity (R134a)							
	10 W	20 W	30 W	40 W	50 W	60 W	70 W
20 g	0.00029	0.00029	0.00028	0.00027	0.00027	0.00026	0.000247
40 g	0.00029	0.00028	0.00027	0.00026	0.00025	0.00024	0.00023
60 g	0.00029	0.00028	0.00027	0.00026	0.00025	0.00024	0.000238
80 g	0.00029	0.00028	0.00027	0.00026	0.00025	0.00024	0.00023
100 g	0.00029	0.00028	0.00027	0.00026	0.00025	0.00024	0.000233

Figure B.7: Grooved heat pipe with R134a: variation of liquid viscosity $(Pas-s)$ at θ=4.5°

Grooved Heat Pipe: Vapor density (R134a)							
	10 W	20 W	30 W	40 W	50 W	60 W	70 W
20 g	12.2	13.0	13.8	14.7	15.9	17.4	19.4
40 g	13.1	14.4	15.9	17.2	18.9	21.0	23.2
60 g	12.9	14.1	15.5	16.7	18.2	20.2	21.3
80 g	12.8	14.0	15.5	17.1	18.6	20.4	23.3
100 g	12.7	14.5	15.9	17.1	18.7	20.5	22.5

Figure B.8: Grooved heat pipe with R134a: variation of vapor density (kg/m^3) at θ=4.5°

Grooved Heat Pipe: Vapor pressure (R134a)							
	10 W	20 W	30 W	40 W	50 W	60 W	70 W
20 g	245347	262702.3	279703.3	299153.4	323333.7	356024.3	397854
40 g	265889.3	292734.7	324193.4	351423.5	388214.3	431422.9	478193.6
60 g	261241.3	287205.8	316518.4	342059.5	373609.4	414900	436799.9
80 g	258579.1	284082.8	315955.5	348684.9	380696.2	418026.2	478579.6
100 g	256177	294063.1	323620.1	350508.8	382646.7	419770.6	462194.4

Figure B.9: Grooved heat pipe with R134a: variation of vapor pressure (Pas) at θ=4.5°

	Grooved Heat Pipe: Liquid viscosity (R513a)						
	10 W	**20 W**	**30 W**	**40 W**	**50 W**	**60 W**	**70 W**
20 g	0.00021	0.00021	0.00020	0.00019	0.00018	0.00017	0.00016
40 g	0.00022	0.00022	0.00021	0.00020	0.00020	0.00019	0.00019
60 g	0.00022	0.00022	0.00021	0.00021	0.00020	0.00019	0.00019
80 g	0.00022	0.00022	0.00021	0.00021	0.00021	0.00020	0.00019
100 g	0.00022	0.00022	0.00021	0.00021	0.00021	0.00020	0.00019

Figure B.10: Grooved heat pipe with R513a: variation of liquid viscosity $(Pas-s)$ at $\theta=4.5°$

	Grooved Heat Pipe: Vapor density (R513a)						
	10 W	**20 W**	**30 W**	**40 W**	**50 W**	**60 W**	**70 W**
20 g	16.6	18.5	21.0	23.5	26.5	29.9	33.6
40 g	15.1	16.1	17.5	18.7	20.2	22.1	24.1
60 g	15.1	16.1	17.5	18.5	19.9	21.3	22.9
80 g	14.8	15.6	16.6	17.5	18.5	19.9	21.5
100 g	14.6	15.5	16.6	17.3	18.3	19.7	21.7

Figure B.11: Grooved heat pipe with R513a: variation of vapor density (kg/m^3) at $\theta=4.5°$

	Grooved Heat Pipe: Vapor pressure (R513a)						
	10 W	**20 W**	**30 W**	**40 W**	**50 W**	**60 W**	**70 W**
20 g	311913.2	350289.8	399538.2	449851.0	509273.8	574448.7	645703.3
40 g	282485.4	302847.2	330672.8	353644.4	384958.3	422194.7	462116.6
60 g	282485.4	302847.2	330672.8	350289.8	377822.9	406984.5	437834.6
80 g	276867.4	293986.3	311913.2	330672.8	350289.8	377822.9	410747.2
100 g	274091.1	291077.7	311913.2	327487.3	346959.7	374293.5	414536.4

Figure B.12: Grooved heat pipe with R513a: variation of vapor pressure (Pas) at $\theta=4.5°$

Smooth Heat Pipe: Liquid Viscosity (R134a)							
	10 W	20 W	30 W	40 W	50 W	60 W	70 W
20 g	0.00028	0.00027	0.00026	0.00025	0.00024	0.00023	0.00022
40 g	0.00029	0.00028	0.00027	0.00027	0.00026	0.00025	0.00024
60 g	0.00028	0.00027	0.00026	0.00025	0.00024	0.00025	0.00023
80 g	0.00029	0.00028	0.00026	0.00026	0.00025	0.00024	0.00023
100 g	0.00029	0.00028	0.00027	0.00026	0.00025	0.00024	0.00023

Figure B.13: Smooth heat pipe with R134a: variation of liquid viscosity $(Pas-s)$ at $\theta=4.5°$

Smooth Heat Pipe: Vapor density (R134a)							
	10 W	20 W	30 W	40 W	50 W	60 W	70 W
20 g	13.9	15.3	17.1	18.7	20.6	23.2	26.1
40 g	13	14.2	15.5	15.3	16.5	18.1	20.6
60 g	13.6	14.7	17.7	19.1	21.2	19.1	22.5
80 g	13.2	14.6	16.2	17.4	19.1	20.8	22.9
100 g	13.2	14.3	15.9	17.4	19.1	21.2	23.8

Figure B.14: Smooth heat pipe with R134a: variation of vapor density (kg/m^3) at $\theta=4.5°$

Smooth Heat Pipe: Vapor Pressure (R134a)							
	10 W	20 W	30 W	40 W	50 W	60 W	70 W
20 g	282015.3	311479.9	348684.9	382646.7	423276.1	476267.1	537541.9
40 g	262946.4	288514.9	315674.4	312315.4	337302	371375.7	421871.2
60 g	275375.9	298345.2	362230.4	391849.6	436080.1	391849.6	461818.5
80 g	266875.9	296198.2	330261.1	356641.2	391849.6	427511.9	471667.6
100 g	266382.3	291410.9	325055	354792.9	390524.7	436080.1	488700

Figure B.15: Smooth heat pipe with R134a: variation of vapor pressure (Pas) at $\theta=4.5°$

Smooth Heat Pipe: Vapor Pressure (R513a)

	10 W	20 W	30 W	40 W	50 W	60 W	70 W
20 g	305846.3	337115.3	370789.3	377822.9	406984.5	449851.0	491723.2
40 g	293986.3	311913.2	337115.3	367310.4	395854.3	437834.6	491723.2
60 g	321187.3	360427.7	395854.3	466261.1	500440.3	569595.6	651034.2
80 g	285327.4	308868.2	333882.1	367310.4	395854.3	429960.5	474634.5
100 g	299870.9	330672.8	370789.3	410747.2	458000.2	504842.4	559982.0

Figure B.16: Smooth heat pipe with R513a: variation of liquid viscosity $(Pas-s)$ at $\theta=4.5°$

Smooth Heat Pipe: Vapor density (R513a)

	10 W	20 W	30 W	40 W	50 W	60 W	70 W
20 g	13.9	15.3	17.1	18.7	20.6	23.2	26.1
40 g	13	14.2	15.5	15.3	16.5	18.1	20.6
60 g	13.6	14.7	17.7	19.1	21.2	19.1	22.5
80 g	13.2	14.6	16.2	17.4	19.1	20.8	22.9
100 g	13.2	14.3	15.9	17.4	19.1	21.2	23.8

Figure B.17: Smooth heat pipe with R513a: variation of vapor density (kg/m^3) at $\theta=4.5°$

Smooth Heat Pipe: Vapor Pressure (R513a)

	10 W	20 W	30 W	40 W	50 W	60 W	70 W
20 g	305846.3	337115.3	370789.3	377822.9	406984.5	449851.0	491723.2
40 g	293986.3	311913.2	337115.3	367310.4	395854.3	437834.6	491723.2
60 g	321187.3	360427.7	395854.3	466261.1	500440.3	569595.6	651034.2
80 g	285327.4	308868.2	333882.1	367310.4	395854.3	429960.5	474634.5
100 g	299870.9	330672.8	370789.3	410747.2	458000.2	504842.4	559982.0

Figure B.18: Smooth heat pipe with R513a: variation of vapor pressure (Pas) at $\theta=4.5°$